A Printed Phospholipid-based Hybrid Biosensor with Impedimetric-Readout

Zur Erlangung des akademischen Grades eines

DOKTORS DER **INGENIEURWISSENSCHAFTEN**

(Dr.-Ing.)

von der KIT-Fakultät für Elektrotechnik und Informationstechnik des

Karlsruher Instituts für Technologie (KIT)

angenommene

DISSERTATION

von

M.Tech, **Srivatsan K. Vasantham**

Tag der mündlichen Prüfung: 20.03.2025

Hauptreferent: Prof. Dr. rer. nat. **Jasmin Aghassi-Hagmann**

Korreferent: Prof. Dr. Ing. **Maria Francesa Spadea**

Korreferent: PD Dr. rer. nat. Dr. rer. medic. **Michael Hirtz**

Fakultät für Elektrotechnik und Informationstechnik

Karlsruher Institut für Technologie

Postfach 640 76344 Karlsruhe

Declaration

I declare that I have developed and written the enclosed thesis completely by myself, and have not used other sources or means without declaration in the text.

Karlsruhe; **Date**: 20.02.2025

. . . . . .

Srivatsan Kandadhai Vasantham

If you are not willing to risk the usual, you will have to settle

for the ordinary.

-Jim Roh

Acknowledgements

The work presented in this dissertation would not be possible without the contributions of many individuals, and I want to take this opportunity to give thanks to some of the most important here.

Firstly, I wish to express my deepest gratitude to Prof. Dr. Jasmin Aghassi-Hagmann and PD Dr. Dr. Michael Hirtz for their unwavering support, invaluable insights, and continuous encouragement throughout this project. Their exceptional patience and perceptive feedback have not only been instrumental in saving me considerable time and effort but have also facilitated significant personal and professional growth. Their consistent guidance and constructive critiques have propelled me towards remarkable development. I am profoundly indebted to them for the impact in shaping the person I am today.

I extend my heartfelt appreciation to the colleagues-turned-friends in my research group, Mahsa and Wenjing, for their consistent support and camaraderie throughout this journey. Their willingness to lend an ear to my rants and their presence as fantastic office mates have made this experience all the more enjoyable.

A special acknowledgement must be made to Navid for his unwavering support and belief in me throughout my PhD. His guidance and encouragement have been invaluable, and I consider him not just a mentor but a part of my extended family. I am thankful for his presence during the highs and lows of this journey. Special thanks to Nishtha for agreeing to read my thesis and making it clean and even more aesthetic. Also, thanks to my parents and my brother (Shreyas) for always picking up the phone anytime during the day and encouraging me always.

I am beyond words to express the role of my wife, Lahari. Over the past four years, she has stood by me, sharing in my struggles as if they were her own, offering both encouragement and solutions with remarkable patience and understanding. From assisting me with schematics for publications to lending a compassionate ear to my endless discussions on experiments, scientific theories, and rehearsals for conference presentations, she has been an invaluable presence throughout this journey. For all the sacrifices she has made, the patience she has shown, and the unwavering faith she has had in me, I am profoundly grateful.

Abstract

Phospholipids, as integral components of cell membranes, play a pivotal role in various biological processes, including their potential use as biomimetic materials. These amphiphilic molecules not only serve as structural "cushions" for presenting antigens on surfaces but also hold promise for studying cell-like behaviour. Their unique physicochemical properties such as dielectric nature, surface charge and electrochemical stability make phospholipids highly suitable for exploring material interactions and investigating substrates that could serve as advanced electrode materials in biosensor applications. The quest to identify advanced electronic materials suitable for electrode applications has spotlighted nanoglasses, particularly CuZr-based compositions, as promising candidates due to the ability to tailor the surface characteristics such as morphology and grain size to increase the electrochemical performance. However, substantial knowledge gaps persist regarding the complex interactions between phospholipids, cellular membranes, and these emerging materials, particularly in the context of biointerfaces and biosensing applications.

This dissertation explores these facets through two interrelated studies. In the first study, we examine the interaction of nanoglass surfaces with a phospholipid mixture comprising 1,2-dioleoyl-sn-glycero-3-phosphocholine (DOPC) and 1-palmitoyl-2-oleoyl-sn-glycero-3-phospho-L-serine (POPS), which are fundamental components of cellular membranes. Utilizing lipid dip-pen nanolithography, we observe a unique stabilizing effect of nanoglasses on lipid nanostructures, characterized by their ability to constrain lipid spreading on the surface—a phenomenon we term "confinement." This stabilization highlights a potential mechanism by which nanoglasses modulate cell membrane structure and, consequently, cellular behaviour. Such insights pave the way for understanding how

nanoglasses influence cell-material interactions and hold promise for their application in biomimetic systems.

The second study emphasizes the development of a low-volume impedimetric biosensor, designed to minimize analyte consumption by utilizing sample volumes as small as 10 µl, while also requiring reduced material input. he sensor capitalizes on the unique electrochemical properties of an indium oxide (In_2O_3)/lipid interface, employing this composite as an efficient transducer material. This device is termed a hybrid biosensor, as it integrates an organic molecular layer-biotinylated DOPC phospholipids—with an inorganic metal-oxide semiconductor, indium oxide, thereby combining the strengths of both material classes. Fabricated through inkjet printing and functionalized with biotinylated DOPC phospholipids using dip-pen nanolithography, this sensor demonstrates exceptional sensitivity and scalability. The biosensor is optimized for the detection of streptavidin, with the electrochemical impedance spectroscopy (EIS) technique employed to monitor binding events. Substantial variations in leak resistance (R_{leak}) and surface capacitance upon target interaction show the sensor's capability for precise detection. The In_2O_3-based platform exhibits superior performance compared to conventional electrode materials such as gold, highlighting its potential to be used in multiplexed biosensing applications and point-of-care diagnostics.

Together, these two studies bridge critical knowledge gaps by elucidating the interactions between phospholipids and emerging material systems, such as nanoglasses and semiconductor-based electrodes. This work not only contributes to the understanding of phospholipid-material dynamics but also underscores the potential of advanced materials in biosensing technologies. By combining biomimetic lipid systems with innovative materials like CuZr nanoglasses and indium oxide, this research lays the groundwork for future advancements in biointerface design and biosensor development.

Zusammenfassung

Phospholipide spielen als integrale Bestandteile von Zellmembranen eine zentrale Rolle in verschiedenen biologischen Prozessen einschließlich ihrer möglichen Verwendung als biomimetische Materialien. Diese amphiphilen Moleküle dienen nicht nur als strukturelle „Polster“ für die Präsentation von Antigenen auf Oberflächen, sondern sind auch vielversprechend für die Untersuchung zellähnlicher Verhaltensweisen. Aufgrund ihrer einzigartigen physikalisch-chemischen Eigenschaften eignen sich Phospholipide hervorragend zur Erforschung von Materialwechselwirkungen und zur Untersuchung von Electrode, die als fortschrittliche Elektrodenmaterialien für Biosensoranwendungen dienen könnten. Unter diesen Materialien haben sich Nanogläser wie CuZr-basierte Zusammensetzungen aufgrund ihrer neuartigen Oberflächenmerkmale und elektrochemischen Eigenschaften als vielversprechende Kandidaten erwiesen. Trotz dieser Fortschritte gibt es nach wie vor erhebliche Lücken im Verständnis der komplizierten Wechselwirkungen zwischen Phospholipiden, Zellmembranen und neuen Materialien, insbesondere bei Anwendungen, die Bioschnittstellen und Biosensorik umfassen.

In dieser Dissertation werden diese Aspekte in zwei miteinander verbundenen Studien untersucht. In der ersten Studie wird die Wechselwirkung von Nanoglasoberflächen mit einer Phospholipidmischung untersucht, die aus 1,2-Dioleoyl-sn-glycero-3-phosphocholin (DOPC) und 1-Palmitoyl-2-oleoyl-sn-glycero-3-phospho-L-serin (POPS) besteht, den grundlegenden Bestandteilen von Zellmembranen. Mit Hilfe der Lipid-Tauchstift-Nanolithografie beobachten wir eine einzigartige stabilisierende Wirkung von Nanogläsern auf Lipid-Nanostrukturen, die durch ihre Fähigkeit gekennzeichnet ist, die Ausbreitung von Lipiden auf der Oberfläche einzuschränken - ein Phänomen, das wir „Confinement“ nennen. Diese

Stabilisierung weist auf einen möglichen Mechanismus hin, durch den Nanogläser die Zellmembranstruktur und damit das Zellverhalten beeinflussen. Diese Erkenntnisse ebnen den Weg zum Verständnis, wie Nanogläser die Wechselwirkungen zwischen Zellen und Materialien beeinflussen, und sind vielversprechend für ihre Anwendung in biomimetischen Systemen.

Die zweite Studie konzentriert sich auf die Entwicklung eines impedimetrischen Biosensors mit geringem Volumen, der die Eigenschaften von Indiumoxid (In_2O_3) als Wandlermaterial nutzt. Der mittels Tintenstrahldruckverfahren hergestellte und mit biotinylierten DOPC-Phospholipiden funktionalisierte Sensor zeichnet sich durch außergewöhnliche Empfindlichkeit und Skalierbarkeit aus. Der Biosensor ist für den Nachweis von Streptavidin optimiert, wobei die elektrochemische Impedanzspektroskopie (EIS) zur Überwachung der Bindungsvorgänge eingesetzt wird. Erhebliche sensitivität des Leckwiderstands (R_{leak}) und der Oberflächenkapazität bei der Interaktion mit dem Target zeigen die Fähigkeit des Sensors zur präzisen Erkennung. Die In_2O_3-basierte Plattform zeigt eine überlegene detektions im Vergleich zu herkömmlichen Elektrodenmaterialien wie Gold, was ihr Potenzial für Multiplex-Biosensoranwendungen und Point-of-Care-Diagnostik unterstreicht.

Zusammengenommen schließen diese Studien kritische Wissenslücken, indem sie die Wechselwirkungen zwischen Phospholipiden und neuen Materialsystemen wie Nanogläsern und halbleiterbasierten Elektroden aufklären. Diese Arbeit trägt nicht nur zum Verständnis der Phospholipid-Material-Dynamik bei, sondern unterstreicht auch das Potenzial fortschrittlicher Materialien für Biosensorik-Technologien. Durch die Kombination biomimetischer Lipidsysteme mit innovativen Materialien wie CuZr-Nanogläsern und Indiumoxid legt diese Forschung den Grundstein für künftige Fortschritte bei der Gestaltung von Bioschnittstellen und der Entwicklung von Biosensoren.

Table of Contents

List of Figures

List of Tables

I. INTRODUCTION

Chapter 1: INTRODUCTION

1.1 Motivation

Affinity biosensors are important tools for detecting different biomedical analytes, such as DNA, proteins, and cells. While most sensors today rely on optical readout, using purely electronic readout can help reduce the system's cost, size, and power use. In this method, analytes are detected by measuring changes in impedance at the electrode-solution interface, where a probe on the electrode selectively captures the target analyte. A major advantage of impedance biosensors is that they allow real-time monitoring of analyte binding without needing the labelling compounds that most other affinity biosensors require. This ability to detect without labels and monitor interactions in real time highlights the potential of impedance biosensors as an effective and affordable option for many biomedical uses. Impedance biosensors usually rely on one functionalized electrode and require a large and costly impedance analyser to operate. By making the measurement system smaller and cheaper, it opens the door to new uses. Semiconductor technology enables the development of smaller and more affordable biosensors, making them more practical and available for various uses. In recent years, there has been growing interest in field-effect transistor (FET) and organic electrochemical transistors (OECTs)[1–4] based biosensors for detecting biomolecules such as nucleic acids and proteins, with graphene and indium oxide playing key roles as channel materials.[5,6] The use of indium oxide (In_2O_3) as a semiconductor channel material stands out because it provides important benefits compared to silicon and other alternatives. In_2O_3 is easier to fabricate, can be fully printed, and can also be used on flexible substrates, which expands its applications.

Metal oxides, such as indium oxide (In_2O_3), present significant advantages in FET-based sensors due to their cost-effectiveness and remarkable stability in aqueous

environments, as compared to those of traditional materials. For instance, silicon, a widely used material in FETs, requires complex surface passivation to maintain stability, whereas indium oxide inherently exhibits robust chemical and environmental resilience. Similarly, while gold offers excellent electrical conductivity, its high cost and dependence on additional functionalization steps limit its practicality compared to the more affordable and versatile indium oxide. Carbon-based materials, such as graphene, are used for their high conductivity, but they often experience reduced performance in aqueous or oxidative environments where indium oxide remains stable. Additionally, other metal oxides like zinc oxide (ZnO) and titanium dioxide (TiO_2) share similar stability traits; however, indium oxide outperforms them due to its higher electron mobility and enhanced surface reactivity, making it particularly suitable for biosensing applications. Additionally, indium oxide thin-film transistors have been widely adopted in industries such as touch screens, displays, and solar cells due to their excellent electronic performance and large-area consistency.[7–9] This makes In_2O_3 a highly promising material for biosensor applications, offering both flexibility in fabrication and performance advantages over silicon.

This research aims to explore and evaluate different metal electrode materials that are compatible with phospholipids for their use in impedance biosensors. The principal goal of this work is to fabricate and to develop a fully printed, label-free impedance biosensor using indium oxide and phospholipids, a design that has not yet been achieved but promises to address problems such as biofouling(which refers to the nonspecific accumulation of biological materials like proteins, cells, or microorganisms on the sensor surface) and modular coupling(integration of independently optimized, interchangeable components within a system, enabling seamless functionality and adaptability across diverse applications). Label-free biosensors reduce the overall cost and complexity by eliminating the need for

additional labelling compounds, but existing devices have yet to incorporate both indium oxide and phospholipids in a fully printed format. The ultimate goal is to build an efficient biosensor capable of detecting proteins through affinity binding, enhancing the practicality and functionality of label-free biosensing technologies.

1.2 Structure of the thesis

Chapter 2 begins with a brief introduction to the fundamental concepts of biosensors, offering a foundational understanding of their general function and importance. This background will set the stage for a more detailed exploration of impedance biosensors. The chapter will cover key concepts, principles, and terminology associated with impedance biosensing, which are essential for understanding the subsequent chapters of this dissertation. The chapter aims to provide clarity on why impedance biosensors are particularly relevant for protein detection and how they fit within the broader scope of biosensor technologies.

In Chapter 3, attention shifts to the various printing and fabrication techniques used for developing biosensors, with a specific focus on the materials chosen for these experiments. The chapter will detail the selection of indium oxide and phospholipids as key components in sensor development, exploring why their combination is ideal for impedance-based detection. By examining the benefits of using these materials together, this chapter will demonstrate how their complementary properties such as indium oxide's electronic capabilities and phospholipids' bio-functional role create an optimal foundation for biosensor functionality. Additionally, the chapter will introduce the experimental methods used throughout the thesis, laying the groundwork for the discussion of results.

Chapter 4 investigates the unique properties of phospholipids, focusing on their enhanced stability when incorporated into CuZr nanoglasses. It will highlight the

improved stability of phospholipids and peculiar lipid arrangement that could be observed in nanoglasses.

Chapter 5 presents the core experimental results of the thesis, focusing on the development and performance of label-free impedance-based biosensors for streptavidin detection. The chapter will showcase the effectiveness of the indium oxide-phospholipid system in achieving selective and sensitive detection of streptavidin, highlighting the practical application of the sensor in real-world scenarios. The results will be analysed in relation to the methods outlined in Chapter 3.

Chapter 6 explores the potential future applications and extensions of this work, particularly in broadening the scope to detect a wider range of diseases using impedance biosensors. This chapter will also summarize the key findings of the thesis, reflecting on the advancements made in terms of printed biosensors and the potential for these sensors to be used in the context of biomedical diagnostics.

II. THEORY

Chapter 2: IMPEDANCE BIOSENSORS

The field of impedance biosensors demands an interdisciplinary understanding, requiring knowledge from biology, materials science, electrical engineering, chemistry, and physics. Many researchers entering this area may not have a complete background in all these domains, which can make grasping the full scope of the field challenging. Moreover, the relevant literature is dispersed across a variety of technical journals and conferences from these different disciplines, making it difficult to acquire the foundational knowledge necessary to follow the latest advancements.

This chapter serves as a comprehensive introduction for both electrical engineers and biochemists to familiarize themselves with key concepts related to impedance biosensors. The chapter concludes with a review of significant literature on impedance biosensors and highlights key areas that require further research, although only a portion of these could be tackled in this work.

2.1 Background on Biosensors

In recent decades, and particularly in the wake of the COVID-19 pandemic, there has been a substantial surge in research dedicated to biosensors, driven by the urgent need for rapid and accurate diagnostics coupled with the imperative to minimise device costs. Biosensors are sophisticated systems designed for the detection and quantification of biomolecules, such as DNA, proteins, and microorganisms. A typical biosensor (**Figure 2.1a**) is composed of three fundamental components: a transducer (nanomaterial, semi-conductor, etc.), a bio-recognition element (DNA, proteins, or enzymes) and the target analyte. As a consequence of the interaction between the analyte and the recognition element,

the transducer converts this interaction into a measurable signal, typically in the form of optical or electrical output.

Biosensors can be categorised based on the underlying transduction mechanism employed (**Figure 2.1b**), leading to various types such as:

- optical detection biosensors,
- resonant detection biosensors,
- thermal detection biosensors,
- ion-sensitive field-effect transistor (ISFET) biosensors, and
- electrochemical biosensors.

Furthermore, based on the type of biorecognition layer utilised, biosensors can be classified as enzyme-based, antibody-based, cell-based, DNA-based, or lipid-based. Electrochemical biosensors can be further classified into potentiometric, amperometric, and conductometric sensors.

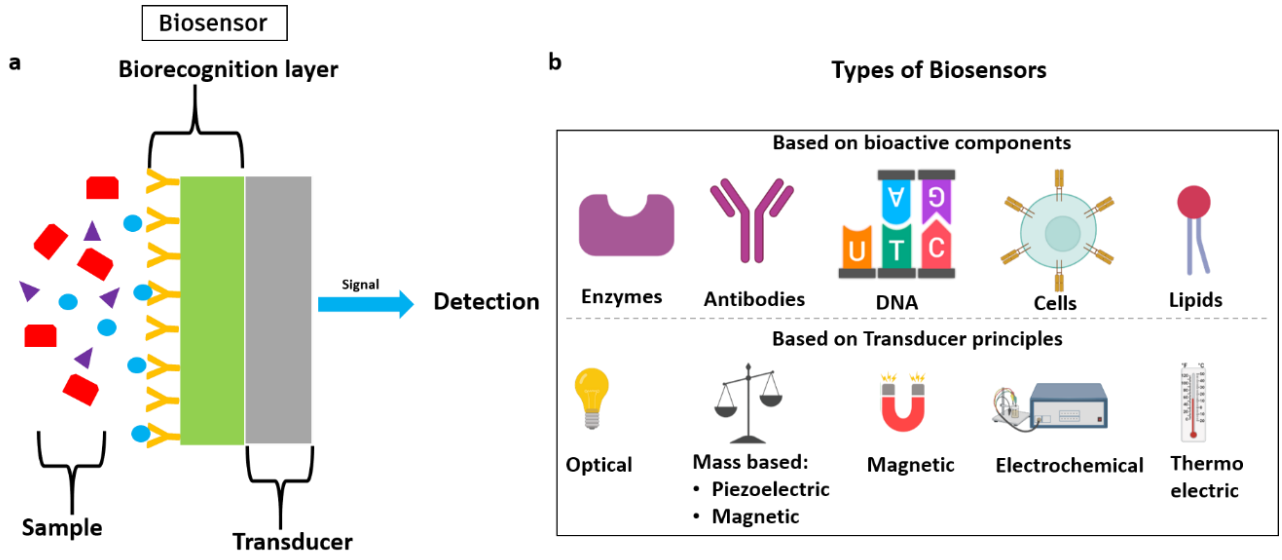

Figure 2.1 Components and Types of Biosensors
a) Components of a typical biosensor. b) The different types of biosensors based on recognition element and transducer type.

The integration of these elements facilitates precise molecular detection—this makes biosensors indispensable tools in modern diagnostics. This field continues to

evolve and holds the potential to address critical challenges in healthcare and beyond.

2.1.1. Definition of Impedance Biosensor

Electrical biosensors can be classified into voltammetric, conductometric and impedance-based biosensors. Voltammetry and amperometry techniques measure the current at an electrode as a response to the applied electrode-solution voltage. These methods operate using direct current (DC) or pseudo-DC signals and deliberately alter the conditions at the electrode. On the other hand, impedance biosensors work by measuring the electrical impedance at an interface under alternating current (AC) steady-state conditions with a constant DC bias. Typically, this is done by applying a small sinusoidal voltage at a specific frequency and recording the resulting current. Repeating this process at various frequencies allows for the calculation of the current-to-voltage ratio at each frequency, which produces an impedance spectrum. This method, referred to as Electrochemical impedance spectroscopy (EIS), is widely employed to investigate different electrochemical processes over a broad frequency range. Electrochemical impedance spectroscopy enables the detection of biological molecules by measuring changes at the electrode-solution interface.

2.1.2. Applications of Electrochemical impedance spectroscopy

Impedance biosensors are capable of detecting a wide range of target analytes by modifying the probe utilized for detection. In this thesis, the focus is to detect streptavidin through biotinylated phospholipids, though electrochemical impedance spectroscopy is used in a variety of biological applications such as:

1) Detection of biologically significant small molecules[10,11]

2) Detection and quantification of cell presence or concentration[12–14]

3) Analysis of lipid bilayers, particularly in systems involving membrane proteins[15–17]

4) Mapping of impedance structures through the use of scanning probe techniques[18–20]

Beyond biosensor applications, electrochemical impedance spectroscopy (EIS) finds utility in diverse fields, such as monitoring corrosion processes, analyzing charge transfer dynamics in fuel cells, and assessing battery performance.[21–23] Recently, EIS has also been applied to field-effect transistors (FETs), where changes in the semiconductor surface charge influence resistance or capacitance, resulting in modulated impedance signals.[24] Numerous field-effect transistors (FETs) have been developed and reported in recent years, as documented in contemporary reviews.[25–28]

2.1.3. Why Impedance Biosensors?

Electrical biosensors show the greatest potential in applications where affordability, compact size, and speed are prioritized over ultimate sensitivity or detection limits. Impedance sensors, in particular, are promising for point-of-care diagnostics.[29–32] By reducing both the cost and time for each reliable measurement, these sensors could become feasible for routine medical check-ups and even at-home health monitoring. However, critical questions remain: can these sensors achieve high selectivity and specificity in detecting diseases, and are they robust and stable enough for widespread use? If these challenges are met, impedance biosensors could enable efficient, rapid, label-free, and affordable biomolecule detection in real time.

2.2 Fundamentals of Impedance Biosensors

This section covers the key concepts such as basic principles of electrical impedance, electrode -electrolyte interface, electrode materials commonly used as electrodes, equivalent circuit models and signal analysis and data interpretation

2.2.1. What is Impedance?

In the context of impedance biosensors, the concept of electrical impedance is important to understand how the devices detect biological molecules through changes in electrical properties at an interface. Impedance, often represented by the symbol Z, is a measure of the opposition that a circuit presents to the flow of alternating current (AC). Impedance combines both resistive and reactive (capacitive or inductive) components, making it a more complex measurement than simple resistance, which only applies to direct current (DC) circuits.

Impedance can be defined as the ratio of the AC voltage V applied across a component to the resulting current I that flows through it:

$$Z = \frac{V}{I} \tag{1}$$

In a biosensor, an AC signal is typically applied to an electrode in contact with an electrolyte solution, and the impedance of this interface is measured. The impedance Z in an AC circuit can be expressed as a complex quantity:

$$Z = R + jx \tag{2}$$

where:

- R is the resistance, representing the opposition to current due to collisions within the conductor,
- j is the imaginary unit, where $j = \sqrt{-1}$
- x is the reactance, which varies with the frequency of the applied AC signal and accounts for capacitive or inductive opposition.

For a purely resistive element, $X = 0$, so the impedance Z is simply equal to R. However, in practical biosensors, capacitive effects play a significant role, especially at the electrode-electrolyte interface, which can make the system behave like a

capacitor. In this case, the impedance is frequency-dependent and can be described using capacitive reactance X_C:

$$X_C = \frac{1}{\omega C} \tag{3}$$

where:

- ω is the angular frequency of the AC signal, ω=2πf (with f as the frequency),
- C is the capacitance of the electrode interface.

This leads to the total impedance for a simple RC (resistor-capacitor) circuit, which is a commonly used model in biosensors, being given by:

$$Z = R + \frac{1}{j\omega C} \tag{4}$$

Impedance biosensors rely on changes in Z that occur when biomolecules, such as proteins or nucleic acids, interact with the electrode surface. This interaction changes the properties of the interface, often modifying R, C, or both. For instance, a charged molecule on the electrode surface can alter the double-layer capacitance (C_{dl}) or the charge transfer resistance (R_{ct}), resulting in a measurable change in impedance that is proportional to the concentration of the target analyte. By analysing the changes in R_{ct}, C_{dl} with respect to the frequency one can gain insight into the biological interactions occurring at the electrode surface.

2.2.2. Electrodes

To measure electrolyte-solution impedance, a minimum of two electrodes is required, though typically three are employed for greater control and precision. In a standard three-electrode setup, the current is measured at the working electrode, which is commonly functionalized with a probe (protein, DNA or lipid) to target specific analytes. To establish the desired potential difference between the working

electrode and the surrounding electrolyte solution, additional electrodes—either a reference electrode, a counter electrode, or both—are necessary to create a stable electrical contact with the solution.

Directly inserting a metal wire at a set potential is not sufficient for controlling the solution's potential, as the solution-metal interface introduces a natural potential difference influenced by the electrode's surface composition, microstructure, and the solution's ionic profile. A reference electrode provides a consistent, reproducible electrical potential between its metal contact and the solution, enabling precise application of a known voltage between the electrolyte solution and the working electrode. Silver-silver chloride (Ag/AgCl) electrodes are the most frequently used reference electrodes in impedance biosensors due to their stable and well-defined potential. The potential at the Ag/AgCl interface remains stable as long as the chloride ion concentration in the solution is constant and any chloride exchange with the AgCl interface is minimal. In some cases, a pseudo-reference or quasi-reference electrode, such as a platinum wire, can be used as a substitute for a standard reference electrode under specific conditions, though this is generally not preferred due to potential variability. Neglecting the use of a reference electrode can lead to poorly regulated DC bias across the electrode-electrolyte interface, which is a common oversight in biosensor design.[33]

The counter electrode plays a complementary role by supplying current to the solution to maintain the intended electrode-solution potential. This electrode is often significantly larger than the working electrode, allowing it to provide sufficient current with minimal interface impedance, thereby ensuring it does not interfere with the working electrode's measurements. The counter and reference electrodes typically function within a feedback loop where the counter electrode adjusts the solution's potential, as monitored by the reference electrode.

Important to note that, the roles of the counter and reference electrodes can be merged if the reference electrode can supply adequate current, and if any resistive drop in the solution is negligible or non-critical. This is more feasible with smaller electrodes. When the counter and reference electrodes are combined, the three-electrode setup effectively becomes a two-electrode configuration. Here, the measurement captures the combined impedance of both electrodes along with the solution, in contrast to a three-electrode arrangement where only the impedance between the working and reference electrodes is measured.

2.2.3. Electrode Materials

The selection of appropriate electrode materials is critical in the design of impedimetric biosensors due to the requirements of biocompatibility and non-toxicity. The electrode surface must not denature proteins or disrupt the structural integrity of other biomolecules interfacing with the sensor. This factor is particularly significant when the biomolecules are printed directly onto the electrode surface, a process that depends on both the chemical stability and the surface properties of the electrode material.

Gold is traditionally the most widely used electrode material in impedance biosensors due to its stability, excellent conductivity, and relative inertness, making it highly compatible with biological samples. Gold's work function (approximately 5.4 eV) aligns well for many biosensing applications, providing stable, reliable measurements.[34] However, in recent years, there has been an increasing interest in indium tin oxide (ITO) as an alternative electrode material, owing to its advantageous electrical properties and optical transparency. ITO has a work function around 4.7 eV, which allows for effective charge transfer and minimal interference with the biomolecular layer.[35] Its transparency makes it particularly valuable in applications requiring optical monitoring alongside electrochemical

measurements. In this thesis, ITO has been explored as a potential electrode material due to these beneficial attributes.

Since, the aim of the work is to fabricate a Field Effect Transistor (FET) like device, the choice of material for the transducing semiconductor channel is equally important, as it significantly influences the efficiency and sensitivity of the biosensor. Several different types of metal oxide semiconductors have been reported including ZnO, In_2O_3, IZO, IGZO, SnO, and CuOx have been used in biosensor applications[36] but the most important thing is that the semiconductor material needs to exhibit strong charge transport properties to facilitate signal transduction. Indium oxide, with a band gap around 3.6 eV, was selected for this thesis due to its remarkable semiconducting characteristics, its compatibility with inkjet printing and applications in biosensing.[37–39] Indium oxide provides a favourable band alignment with common electrode materials, enabling efficient charge transfer at the metal-semiconductor interface. Moreover, indium oxide has been shown to support lipid dip-pen nanolithography (L-DPN) of lipid layers, which is essential for precise biomolecule patterning and further enhances its suitability for biosensing applications.[40]

The metal-semiconductor contact in this setup plays a pivotal role, as it impacts the efficiency of charge injection and collection. A proper contact between the metal electrode and the semiconductor is crucial for minimizing the Schottky barrier, thereby improving the sensitivity of the sensor. In impedimetric sensing, this contact governs the overall impedance response and contributes significantly to the reproducibility and accuracy of the measurements. By carefully selecting indium oxide as the transducing channel material and ITO or gold as the electrode, this work aims to optimize the sensor's electrical performance and biological compatibility, achieving a stable interface for high-precision biosensing.

2.2.4. Instrumentation

A potentiostat is an electronic circuit used to control the voltage between a solution and a working electrode while simultaneously measuring the resulting current flow. Functionally, it utilizes a feedback loop to adjust the current at the counter electrode so that the voltage of the solution, recorded by the reference electrode, matches the set command voltage. In this setup, the working electrode is held at ground potential, with its current being measured via a transimpedance amplifier. This configuration allows the potentiostat to apply a specified voltage across the electrode-electrolyte interface and record the resulting current, which is essential for impedance measurements.

If the counter and reference electrodes are combined, a feedback loop is no longer required, though impedance can still be determined similarly. Potentiostats specially designed for Electrochemical impedance spectroscopy (EIS) are commonly used to measure AC impedance across a broad frequency range, typically from 10^{-2} to 10^{-5} Hz. Computer control is widespread in both potentiostats and EIS analyzers, allowing for efficient data collection and digital post-processing to enhance measurement accuracy and analysis.

2.2.5. Faradaic vs Non-faradaic Impedimetric Sensing

In typical Faradaic electrochemical impedance spectroscopy (EIS) experiments, the impedance variations resulting from a binding event reflect either an increase or decrease in the extent of surface blockage. These variations alter the accessibility of redox markers in the electrolyte solution (bulk electrolyte) to the electrode surface. For instance, the impedance of the system may rise due to the binding of a large target molecule, which generates an increased electrostatic barrier, thereby obstructing redox probes from reaching the electrode surface. Conversely, a reduction in impedance may result from a lowered electrostatic barrier, as occurs

when surface-bound molecules carry an opposite charge relative to the redox probes, facilitating their approach to the electrode.

However, due to the complexity of biological probes and their specific binding interactions, the observed impedance changes may involve a combination of factors. For example, simultaneous effects, such as the binding of large target molecules and local charge screening near the electrode surface, can create complex impedance profiles. This combination of mechanisms can result in intricate shifts in impedance that require detailed analysis to interpret accurately.[41]In contrast to Faradaic electrochemical impedance spectroscopy (EIS), non-Faradaic EIS is conducted without redox-active species in the electrolyte. In non-Faradaic systems, the analysis centres primarily on the double-layer capacitance (C_{dl}) rather than the charge transfer resistance (R_{ct}). Since no redox markers are present, electron transfer processes are negligible, and the overall impedance response is predominantly governed by the capacitive component. This capacitance arises from the charging and discharging dynamics at the electrode-electrolyte interface, providing useful information into interfacial properties without the influence of redox reactions.[42]

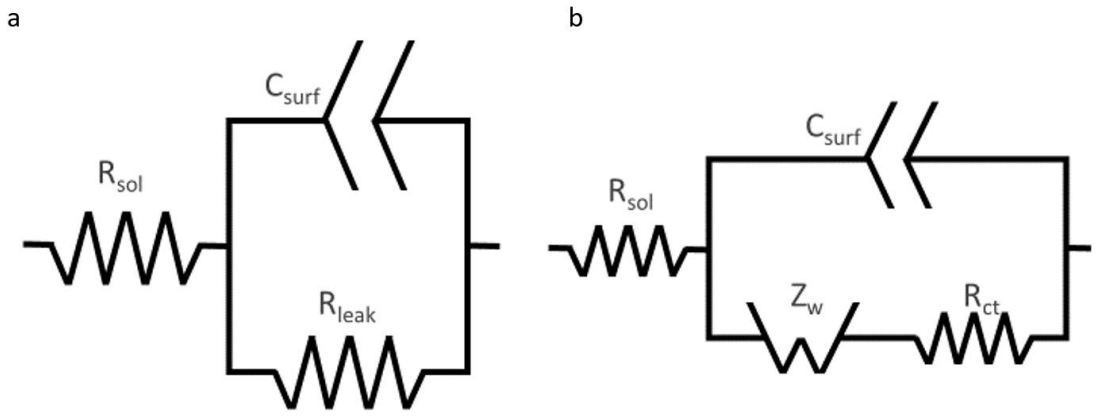

Figure 2.2 Equivalent Electrical Circuit for Faradaic and Non-Faradaic Biosensors.
Typical circuit for a) non-faradaic and b) faradaic interfaces in biosensors.

Figure 2.2 presents the two primary circuit models commonly employed to interpret impedance biosensor data, depending on whether a faradaic or non-faradaic approach is used. This section will now discuss the relationship between circuit components and their associated physical phenomena, although it should be noted that, in practice, model selection is often empirical, and distinct physical effects may be simplified into a single circuit element[43].

The solution resistance, R_{sol}, arises from the movement of ions within the bulk solution in response to an applied voltage, and it typically remains unaffected by target binding. Given the sensor geometry and solution conductivity—calculated from the diffusion coefficients of the solution's ions - R_{sol} can be theoretically predicted. However, in practice, it is generally treated as a fitting parameter since its exact value is often not critical.

The capacitance between the metal electrode and the ions in solution, C_{surf}, can be modelled as a series combination of surface modification capacitance and ionic double-layer capacitance. The component due to surface modification depends on the probe layer's thickness and dielectric constant and can be approximated as a parallel plate capacitor with capacitance

$$C = \varepsilon_r \varepsilon_0 \frac{A}{t} \tag{5}$$

where ε_r is the relative dielectric constant, A is the electrode area, and t is the insulator thickness. The ionic double-layer capacitance, arising from the electrostatic attraction of ions in solution to a charged electrode, will be further explored in the next section.

C_{surf} is frequently represented as a constant phase element rather than as a pure capacitance which will be discussed in **Section 2.2.6**. In parallel with the surface capacitance, a resistive pathway exists, modelled by R_{leak} for non-faradaic sensors,

or by the series combination of Z_w and R_{ct} for faradaic sensors. Ideally, R_{leak} would be infinite in the absence of redox-active species, but practically it is finite, as will be explained. The Warburg impedance, Z_w, is relevant only in faradaic electrochemical impedance spectroscopy (EIS) and represents the delay due to diffusion of electroactive species to the electrode[44]. Z_w becomes significant only at low frequencies, may be influenced by convection (rendering it invalid over certain experimental timescales), and presents a phase shift of -45°.

The charge transfer resistance, R_{ct}, represents the resistance associated with electron transfer between the electrode and redox species. Its magnitude reflects both the overpotential (energy potential related to the oxidation or reduction at the electrode) and the energy barrier encountered by redox species due to electrostatic repulsion or steric effects. In impedance biosensors, C_{surf} and R_{ct} are the two primary circuit elements used to detect affinity binding. In non-faradaic biosensors, changes in C_{surf} reflect modifications to the surface dielectric constant and/or thickness upon target binding. In contrast, in faradaic biosensors, R_{ct} changes as binding events modulate redox species access to the electrode.

2.3 Understanding Impedance Data

In electrochemical impedance spectroscopy, fitting an equivalent circuit model to the measured impedance spectrum allows researchers to estimate component values for resistances and capacitances, yet no single model universally represents all systems accurately. Typically, circuit models are selected based on prior assumptions, but the electrode-solution interface may exhibit behaviours that diverge from any idealized model, particularly at higher frequencies. Consequently, model selection can be more interpretive than prescriptive. Generally, raw impedance data are mapped onto a selected model, and changes in specific circuit parameters are analyzed as the output of the sensor. Alternatively, measurements

at a specific frequency may provide insights based on dominant elements of the circuit, with the relevant circuit component(s) determined by parameter values and shown in **Figure 2.3.**

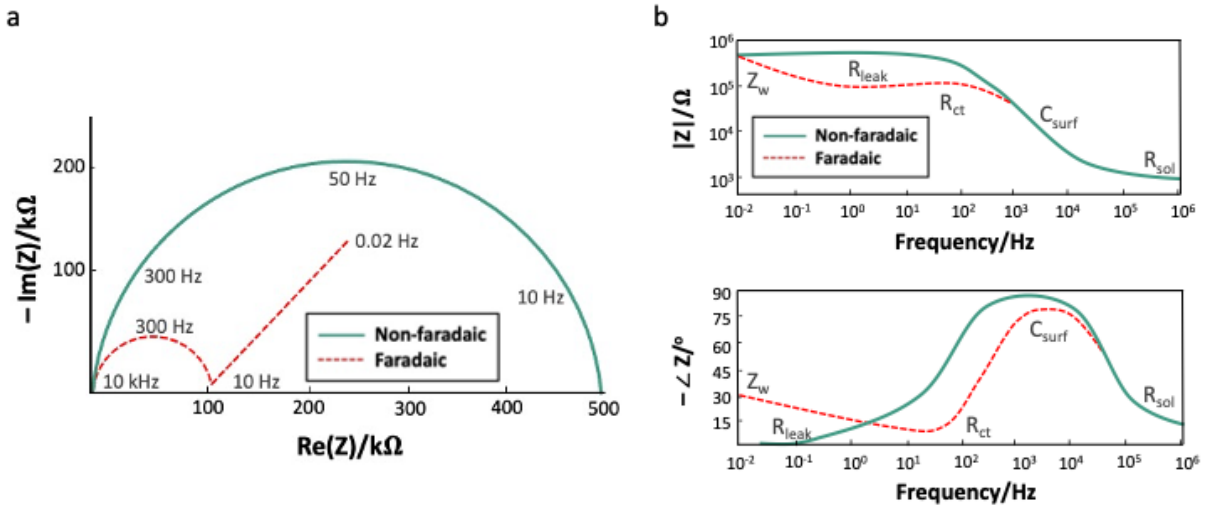

Figure 2.3 Example of Impedance data illustrating both Non-Faradaic and Faradaic responses.

a) Nyquist plot representation b) Bode plot representation. Data generated using the following parameters: solution resistance (R_{sol}) of 1 kΩ, surface capacitance (C_{surf}) of 10 nF with a roughness factor (mmm) of 0.9, leakage resistance (Rl_{eak}) of 500 kΩ, charge transfer resistance (R_{ct}) of 100 kΩ, and a Warburg impedance coefficient (Z_w)of 10^{-5}. Figure adapted from J.S.Daniels et al.,2007[41]

Complex nonlinear least squares (CNLS) fitting, a method that accommodates both magnitude and phase, is a standard approach for refining model parameters. This process is available in several software tools, both free (e.g., LEVM[a]) and commercial (e.g., ZView[45], ZSimpWin[46]). CNLS outputs include error bounds on the fitted parameters, though these are sometimes misinterpreted as experimental error bars in graphical representations. Despite its rigor, the interpretation of impedance spectra remains somewhat subjective.[47] When experimental data are suspected, the Kramers-Kronig transform provides an independent validation check for consistency and reliability.

2.3.1. Double Layer Capacitance

The interfacial region between an electrode and an electrolyte is notably inhomogeneous, characterized by variations in electronic density as well as spatial distributions of ions and solvent molecules. When a charged electrode is in contact with an electrolyte solution, counterions accumulate near the electrode's surface, while co-ions are depleted. This arrangement, known as the electric double layer (EDL), was initially conceptualized by Helmholtz in 1853.[48] The EDL is a structured region that forms when a charged surface interacts with a liquid medium, where the balancing counter charge from the electrolyte aggregates near the surface. Several theoretical models describe the EDL structure, each providing insights into the distribution and behaviour of ions at the solid-liquid interface. **Figure 2.4** illustrates the Helmholtz, Gouy–Chapman, and Stern models of the EDL, where Ψ represents the potential, Ψ_0 is the electrode potential, and IHP and OHP refer to the inner and outer Helmholtz planes, respectively, as defined in the Stern model.

The Helmholtz model provides a foundational yet simplified perspective on the spatial charge distribution at the interface of a double layer. According to this model, the charge on the solid conductive electrode is counterbalanced by oppositely charged ions positioned at a fixed distance, d, from the surface, corresponding to the centre of these counterions. This model views the EDL as a rigid layer of ions, neutralizing the electrode charge at a set distance. While it serves as a basic approximation, the Helmholtz model lacks the flexibility to account for the dynamic interactions and distributions observed in actual systems.[49]

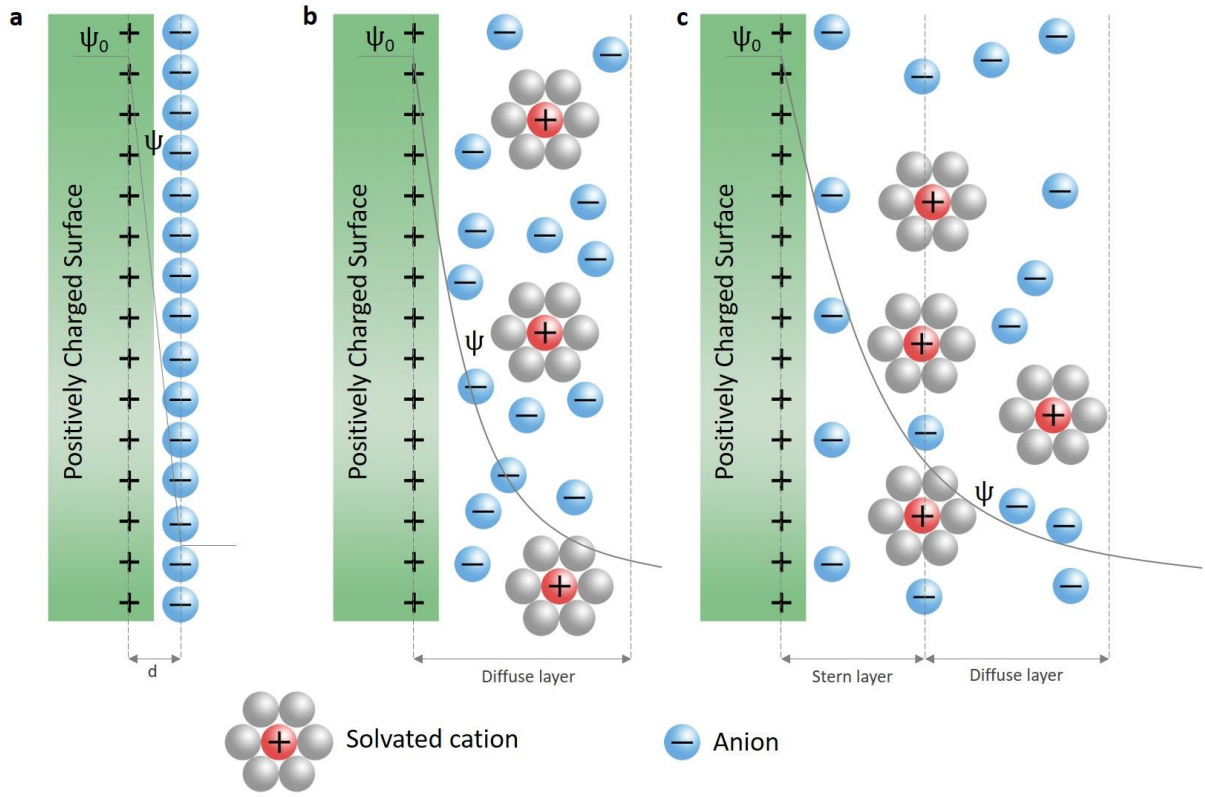

Figure 2.4 Schematic of EDL (Electric Double-Layer) models: Helmholtz model, Gouy-Chapman model, and Gouy-Chapman–Stern model.
Models of the electrical double layer (EDL) at a positively charged surface: a) the Helmholtz b) the Gouy-Chapman and c) the Stern model. In the figure, the inner Helmholtz plane (IHP) refers to the distance of closest approach of specifically adsorbed ions (generally anions), and the outer Helmholtz plane (OHP) refers to the non-specifically adsorbed ions (cations). The OHP is also the plane where the diffuse layer begins. d is the double layer distance described by the Helmholtz model. Ψ0 and Ψ are the potentials at the electrode surface and the electrode/electrolyte interface, respectively. Figure adapted from Meena et al.,2023[50]

The Gouy–Chapman model, or diffuse layer model, refines the understanding of the EDL by considering the mobile and dynamic nature of ions in the electrolyte.[51] According to Gouy, a counterbalancing ionic charge accumulates in the liquid surrounding the charged surface, yet these ions are not rigidly fixed at a set distance from the surface. Instead, they diffuse into the liquid phase until the counter potential generated by this redistribution of charge limits their spread. The thickness of this diffuse layer is partially dictated by the thermal energy of ions, causing them to adopt a concentration gradient near the surface, as described by a Boltzmann distribution. However, the Gouy–Chapman model struggles with

accurately predicting the behaviour of highly charged double layers, as experimentally observed double layers are often thicker than this model would suggest. While the Gouy–Chapman model advances beyond the Helmholtz approximation by addressing ionic mobility, it assumes that ions are point charges and may approach the electrode surface without constraint, which does not hold true in practice. Stern modified the Gouy–Chapman model by incorporating the finite size of ions, thereby restricting their proximity to the electrode. In the Stern model, ions in the first layer are positioned at a defined distance, delta (δ), from the surface. This distance forms the so-called Stern layer, which is divided into two regions: the compact layer, where ions are specifically adsorbed onto the electrode (the inner Helmholtz plane, IHP), and an outer layer where counterions accumulate but remain non-specifically adsorbed (the outer Helmholtz plane, OHP)[52]. This dual-layer structure incorporates the Helmholtz layer as the inner compact layer and the Gouy–Chapman layer as an outer diffuse layer.

The double layer capacitance, arising from the EDL, is a critical parameter in impedance biosensing as it captures the ability of the electrode-electrolyte interface to store charge. Changes in the EDL structure, induced by target binding or other interactions at the electrode surface, modify this capacitance, providing a basis for detecting biomolecular interactions. Non-faradaic impedance biosensing relies heavily on monitoring variations in double layer capacitance, as the absence of redox-active species means that capacitive changes dominate the impedance signal. The EDL models aid in understanding how target binding or surface modifications affect the distribution and accessibility of ions, thus influencing the measured capacitance. In practice, the Stern model's combination of compact and diffuse layers enables a nuanced interpretation of interfacial properties, especially in complex biological matrices where multiple factors can simultaneously affect the EDL and consequently the impedance response.

2.3.2. Constant Phase Element (CPE)

The constant phase element (CPE) is a critical component in electrochemical impedance spectroscopy (EIS), especially in biosensing, where it addresses non-ideal capacitive behaviour often observed at electrode interfaces.[53] The CPE accounts for deviations from ideal capacitance due to surface inhomogeneities, varying charge distributions, or electrode roughness, which standard capacitive elements fail to capture. Mathematically, the impedance of a CPE,

$$z_{c_{PE}} = \frac{1}{T(i\omega)^n} \tag{6}$$

where T is a frequency-independent constant, ω is the angular frequency, and n ($0 < n \leq 1$) denotes the phase element exponent. When n=1, the CPE behaves as a pure capacitor, and for n=0.5, it represents a Warburg impedance, indicating diffusion processes. In biosensor applications, where electrode surfaces interact dynamically with various biochemical targets, the CPE provides a robust model to describe frequency-dependent responses and heterogeneous interfacial properties.

In biosensors, calculating and incorporating the CPE is essential for accurately modelling the electrode-electrolyte interface. This is especially pertinent in scenarios involving double-layer capacitance, diffusion processes, and adsorption phenomena, as these introduce variability in the impedance response across different frequencies.[54] To extract CPE parameters in biosensors, complex nonlinear least squares (CNLS) fitting techniques are commonly used with software such as ZView[45] or EC-Lab[55] or Originlab[56]. By fitting experimental data to a circuit model that includes the CPE, one can obtain values for T and n, which help distinguish contributions from capacitive, resistive, or diffusive elements in the sensor response. Utilizing the CPE in equivalent circuits thus enhances the accuracy

of impedance-based measurements, supporting more precise identification and quantification of biomolecular interactions on the sensor's surface.

2.3.3. Debye Length

Debye length ($\boldsymbol{\lambda}_D$) is a measure of a charge carrier's net electrostatic effect in a solution and how far its electrostatic effect persists.[57] In biosensor applications, the Debye length is crucial because it defines the range over which an electrode's electric field can interact with biomolecules in an ionic solution. Essentially, the Debye length limits how far electrical signals can effectively travel from the electrode into the solution before they become shielded by ions. In physiological conditions, the Debye length is very short (< 1 nm), which is far less than the size of many target biomolecules, such as antibodies or DNA strands that can range from 10-15 nm. This disparity means that only molecules very close to the electrode are detectable, as signals from those further away are blocked by the ionic screening effect of the surrounding ions.

Understanding and managing the Debye length is therefore essential for enhancing biosensor sensitivity. To overcome this limitation, researchers have explored methods to extend detection capability beyond the Debye length. One approach involves designing electrode surfaces with specific geometries, like nanostructures or concave features, which confine ions in a restricted area. This crowding effect reduces the extent of charge screening, allowing electric fields to extend further. Another approach employs surface coatings, such as poly(ethylene glycol) (PEG), to control ion distribution near the electrode, which enhances detection range without disrupting molecular binding interactions.[58]

2.3.4. RC Circle Fitting of Impedance Data

The RC circle is a fundamental tool in analyzing impedance data, particularly in the context of biosensors. It represents the impedance response of an RC (Resistor-Capacitor) circuit, where the combination of resistive and capacitive elements creates a characteristic semi-circular shape in the complex plane. This RC circle provides insight into the sensor's interface properties, especially the charge transfer and capacitance behaviour, which are crucial in biosensor applications.

The RC circle fit is especially useful for biosensors due to its ability to model the interactions at the electrode-electrolyte interface. In biosensing, the interaction of biomolecules on an electrode surface affects the resistance and capacitance, altering the impedance response. The RC circle fit allows for clear identification of changes in resistance (related to binding events or surface modifications) and capacitance (related to the surface's dielectric properties). This makes it a suitable and sensitive approach for detecting and analyzing biomolecular interactions, where small changes in impedance can signify the presence of a target analyte.

Mathematical Representation of the RC Circle

The impedance Z of an RC circuit is expressed as:

$$Z = \frac{R}{1 + \omega^2 R^2 C^2} + i\frac{\omega R^2 C^2}{1 + \omega^2 R^2 C^2} \tag{7}$$

where: R is the resistance, C is the capacitance, ω is the angular frequency, and j is the imaginary unit. The impedance has two components:

$$Re(Z) = \frac{R}{1 + \omega^2 R^2 C^2} \tag{8}$$

$$Im(Z) = \frac{\omega R^2 C}{1 + \omega^2 R^2 C^2} \tag{9}$$

If we now divide Im(Z) and Re(Z) we can relate the angular frequency to the real and imaginary parts, we have:

$$\omega = \frac{Im(Z)}{Re(Z)RC} \tag{10}$$

If we now substitute the value of ω in equation of Re(Z), the impedance components satisfy the equation of a circle in the complex plane:

$$\left(Re(Z) - \frac{R}{2}\right)^2 + Im(Z)^2 = \left(\frac{R}{2}\right)^2 \tag{11}$$

with (R/2,0) on the real axis. This circular form enables precise fitting and parameter extraction, which is useful for biosensor calibration and response analysis.

2.4 Overview of state of the art in impedance sensing

This section consolidates extensive research findings as documented across technical literature. **Table 1** provides a concise overview of selected label-free affinity-based impedance biosensors, allowing for rapid comparison, while the accompanying text delves into additional significant studies. Notably, the reported detection limits for these sensors have not shown a consistent trend of improvement over time. This phenomenon may stem from various factors, including constraints inherent to the affinity binding step, variability in defining detection limits, common-mode noise affecting signal clarity, and growing awareness of reproducibility challenges in sensor performance. These limitations collectively highlight the complex nature of advancing sensitivity in biosensor technology.

Table 1: Overview of published art in the field of Impedimetric Biosensing.

Probe	Target	Limit of Detection (LOD)	Assay principle	Variable	Working electrode	Year	Comments
Antibody	hIgG	50 ng/ml	Antibody antigen interaction	Z at frequency	Polymer	1991 [59]	One of the first affinity impedance sensors
Aptamer	Lysozyme	0.38 µg/ml	Aptamer protein interaction	Z at Frequency	Graphene oxide	2014 [60]	Higher selectivity towards thrombin and BSA
Aptamer	thrombin	0.3 ng/ml	Aptamer protein interaction	Z at frequency		2013 [61]	Sensor with attractive anti fouling properties.
NH2-terminated Aptamer	IgE	0.03 µg/ml	Aptamer protein interaction	Change in double layer capacitance (C_{DL})	Nanocrystalline diamond	2011 [62]	
Anti AFM-1	Aflatoxin	1 pg/ml	Antibody- Antigen interaction	Z at frequency	Silver wire	2012 [63]	Milk samples was used
Anti-avidin	Anti-avidin antibody		Antibody-antigen interaction	Z at frequency	TiO_2	2005	
Anti insulin	insulin	1.2 pM	Antibody-antigen interaction	Z at frequency	Gold	2013 [64]	Blood serum samples were used for detection
Viral antibodies	H3N2 virus	0.79 fM	Antibody-virus interaction				Aneta Anna Dunjova (2020)
S-RBD antibody	S-RBD-protein	0.58 fg/ml	Antibody-antigen interaction	Z at frequency	Gold nanoparticles on ITO	2021 [65]	
Thiolated peptide	Spike protein	18.2 ng/ml	Peptide-protein interaction	Z at frequency	Gold Screen printed electrode	2022 [66]	Detection in 15 mins

Anti cTn-1	Cardiac troponin	0.05ng/ml	Antibody-antigen interaction	Z at frequency	SWCNT	2019 [67]	Paper based device
Polyclonal antibody	Atrazine	1 fg/ml	Antibody-antigen interaction	Z at frequency		2024 [68]	Portable device for herbicide detection
Carbon SPE	MCF-7 cells		Cell protein interaction	Capacitance change after binding of cells	Carbon SPE	2024 [69]	Special technique-potentiodynamic EIS was used
Paraquat specific antibody	Paraquat(herbicide)	0.05 ng/ml	Antibody-antigen interaction	Z at frequency	reduced Graphene oxide(rGO)	2024 [70]	Low volumes (20 µl) was used.
CPS antibody	Capsulated polysachharide(CPS)	0.1pg/ml	ELISA based		ZnO layer on top of gold electrode	2024 [71]	
HRP streptavidin	Hydrogen peroxide (H_2O_2)	10 µM		Z at frequency	Gold Electrode	2008 [72]	Rapid R_{ct} decrease on enzymatic reaction with hydrogen peroxide.
CdSe QDs & DNA	Streptavidin	0.65 pg/ml	DNA-protein interaction/ repulsion	Z at frequency	Modified gold electrode with quantum dots	2018 [73]	Steric hindrance based hybridization assay

Chapter 3: MATERIALS AND TECHNIQUES FOR SENSOR FABRICATION

In this chapter, we delve into the materials and methodologies employed in the fabrication of sensors and the investigation of lipid behaviour on nanoglass surfaces. The discussion begins with an exploration of what are phospholipids, focusing on their self-assembly and functional characteristics that make them ideal for biosensing applications. Subsequently, we examine the role of indium oxide as a semiconductor material, emphasizing its electronic properties and suitability for integration into advanced sensor platforms.

The chapter further addresses the techniques utilized for the precise deposition of these molecules on substrates, including lipid dip-pen nanolithography (L-DPN) and inkjet printing. Finally, the chapter transitions into the characterization techniques employed to analyze the fabricated surfaces, such as scanning electron microscopy (SEM), atomic force microscopy (AFM), and optical microscopy.

3.1 Phospholipids and their applications in Biosensors

Cell membranes are composed of a diverse array of phospholipids that contribute to their structural integrity and functional properties. The primary classes of phospholipids include **phosphatidylcholine (PC)**, **phosphatidylethanolamine (PE)**, **phosphatidylserine (PS)**, **phosphatidylinositol (PI)**, **phosphatidic acid (PA)**, and **sphingomyelin (SM)**. These molecules differ in their head groups and fatty acid compositions, influencing the membrane's biophysical properties, such as fluidity and curvature.

Phospholipids can be categorized based on their charge:

- **Neutral Phospholipids**: Phosphatidylcholine (PC) and phosphatidylethanolamine (PE) are zwitterionic, possessing no net charge at physiological pH. These lipids are primarily found in the outer leaflet of the membrane and play a structural role.
- **Negatively Charged Phospholipids**: Phosphatidylserine (PS), phosphatidylinositol (PI), and phosphatidic acid (PA) carry a net negative charge due to their head groups. These lipids are generally localized to the inner leaflet of the membrane and are involved in cell signalling, membrane trafficking, and electrostatic interactions with proteins.
- **Specialized Lipids**: Sphingomyelin (SM), although neutral, is unique in its involvement in membrane microdomains known as lipid rafts, which play a role in signal transduction.

The asymmetrical distribution of these phospholipids across the bilayer is critical for maintaining membrane dynamics and facilitating interactions with proteins, ions, and other biomolecules, making them integral to study cellular processes and for design of biosensors. Among the phospholipids, dioleoylphosphatidylcholine (DOPC) is widely used due to its low phase transition temperature and fluidity, making it ideal for forming stable and functional bilayers under physiological conditions.[74,75]. It has already been shown in previous studies from our group that lipids form two-dimensional membranes through stacks of single layer to bilayers when patterned on surfaces via L-DPN.[40,76–78] **Figure 3.1** shows the phospholipids used in this study and illustrate their chemical structures.

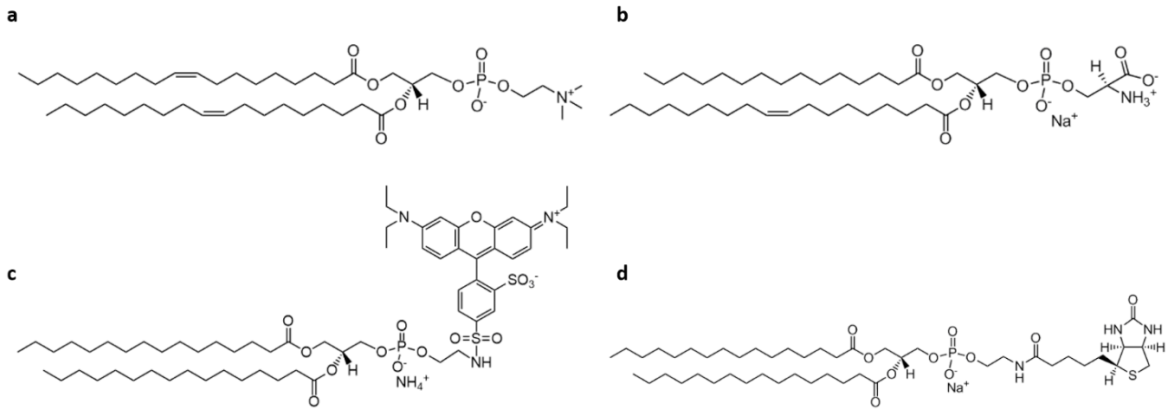

Figure 3.1 Phospholipids used in this study.
a) *18:1 DOPC (1,2-di-(9Z-octadecenoyl)-sn-glycero-3-phosphocholine), b) 16:0-18:1 POPS(1-palmitoyl-2-oleoyl-sn-glycero-3-phospho-L-serine (sodium salt), c) 18:1 Liss Rhod-PE (1,2-dioleoyl-sn-glycero-3-phosphoethanolamine-N-(lissamine rhodamine B sulfonyl) (ammonium salt) d) Biotin PE(1-(12-biotinyl(aminododecanoyl))-2-oleoyl-sn-glycero-3-phosphoethanolamine)*

Applications in Biosensors: A critical advantage of utilizing lipid membranes as matrices for recognition molecules in biosensor applications lies in their ability to mimic the natural orientation of receptor molecules, akin to their arrangement in biological cell membranes. This biomimetic alignment enhances the accessibility of specific binding sites, thereby significantly improving the efficiency and sensitivity of analyte detection. Furthermore, the density of recognition molecules immobilized on the sensor surface can be precisely tuned by modulating the lipid-to-receptor ratio within the liposomes employed for membrane fusion.[79] Such adaptability allows for the fine-tuning of sensor performance to meet the specific requirements of diverse analytical applications. These lipid-based systems provide a versatile platform for detecting biological and chemical analytes.[80]
Furthermore, lipid membranes serve as immobilization matrices for protein insertion for applications such as detection of toxins[81], DNA sequencing[82], studying post-translational modifications[83],etc. This functional versatility underpins their increasing application in diagnostics and environmental monitoring.

3.2 Biotin – Streptavidin binding

The biotin-streptavidin interaction is one of the strongest non-covalent bonds in nature, with a dissociation constant (K_d) on the order of 10^{-14} M,[84] making it highly specific, stable, and robust under a wide range of conditions. This exceptional affinity has been widely exploited in biotechnology, diagnostics, and nanotechnology.[85–87] In biology, biotin-streptavidin binding plays a critical role in anchoring biomolecules, enabling targeted labelling, and facilitating immobilization for various analytical and imaging applications. For instance (**Figure 3.2**), biotinylated antibodies or nucleic acids are often paired with streptavidin-conjugated substrates to create highly specific assay platforms for detecting analytes.

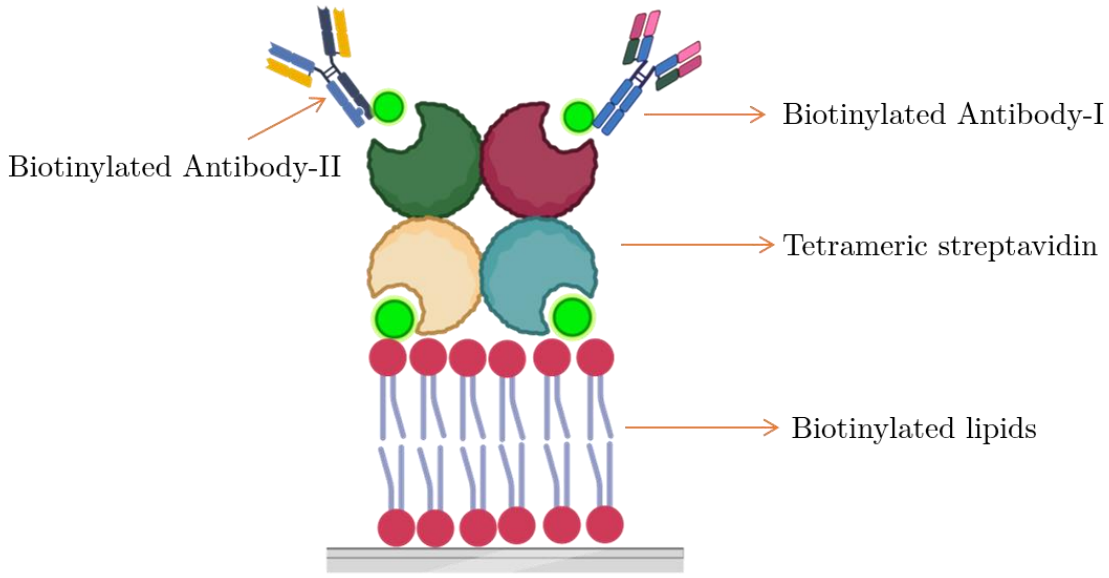

Figure 3.2 Streptavidin binding to specific biotinylated antibodies for disease detection.
Figure created in https://BioRender.com.

Biotin binds to streptavidin with remarkable specificity and high affinity through a combination of extensive hydrogen bonding and van der Waals interactions. The binding pocket within streptavidin is lined by hydrophobic residues, which facilitate the snug fit of biotin, while key polar interactions stabilize the complex. Notably,

flexible loops in streptavidin undergo conformational changes to enclose biotin tightly, enhancing the binding strength. This interaction serves as a model for molecular recognition and is pivotal in various biochemical applications such as biosensors, diagnostics, and targeted delivery systems.[88] The structure of tetrameric streptavidin and the interaction of biotin streptavidin is shown in **Figure 3.3.**

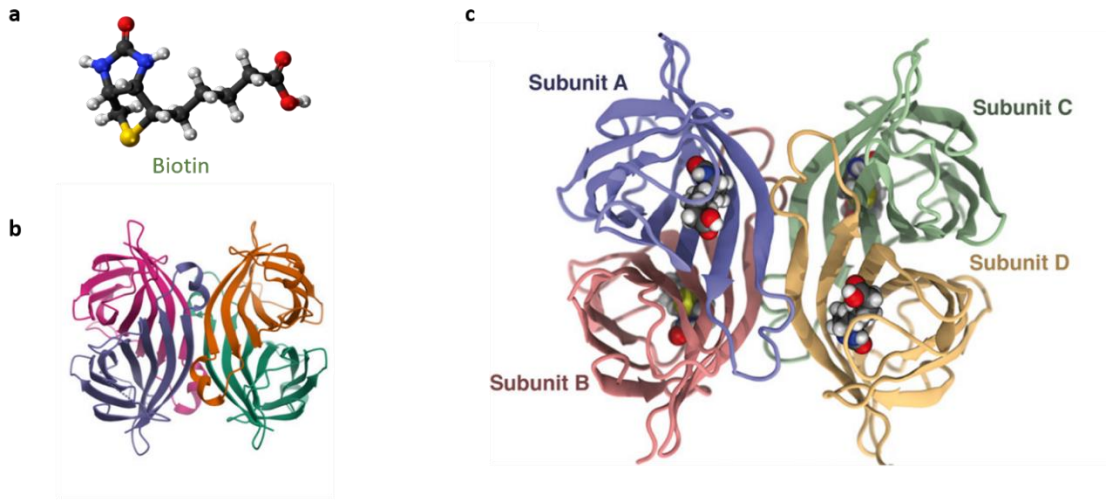

Figure 3.3 Structure of biotin, tetrameric streptavidin and biotin streptavidin binding.
a) *Structure of biotin. b) Structure of tetrameric Streptavidin(PDB code: 1SWC*[89] *c) Shows the interaction of each biotin molecule which can fit into each subunit of the tetrameric streptavidin.*[90]

In the development of electrochemical biosensors, this interaction is particularly valuable. The immobilization of biotinylated biomolecules onto streptavidin-modified electrodes allows for the creation of stable and functional sensing interfaces. Electrochemical impedance spectroscopy is a key technique employed in these biosensors, as it detects changes in surface resistance and capacitance caused by the binding events. These electrochemical changes serve as a direct readout of the molecular interaction, enabling sensitive detection of analytes like proteins and small molecules. Recent advancements in using electrochemical impedance spectroscopy have highlighted its effectiveness in quantifying the kinetics and strength of the biotin-streptavidin interaction, as well as its ability to discern

between specific and non-specific binding events, which is critical for biosensor reliability.

3.3 Indium oxide

Semiconductors exhibit electrical conductivities that fall between those of metals and insulators, with their electrical properties being tunable through factors such as doping, temperature variation, or optical excitation. This adaptability makes semiconductors highly versatile and attractive for numerous electronic applications.[91] While germanium was initially employed in the first-ever transistor, silicon (Si) rapidly replaced it due to its low cost, widespread availability, ease of doping, and excellent compatibility with both n-type and p-type doping. This balance between n- and p-type doped silicon has been a critical factor in the success of silicon-based electronics.

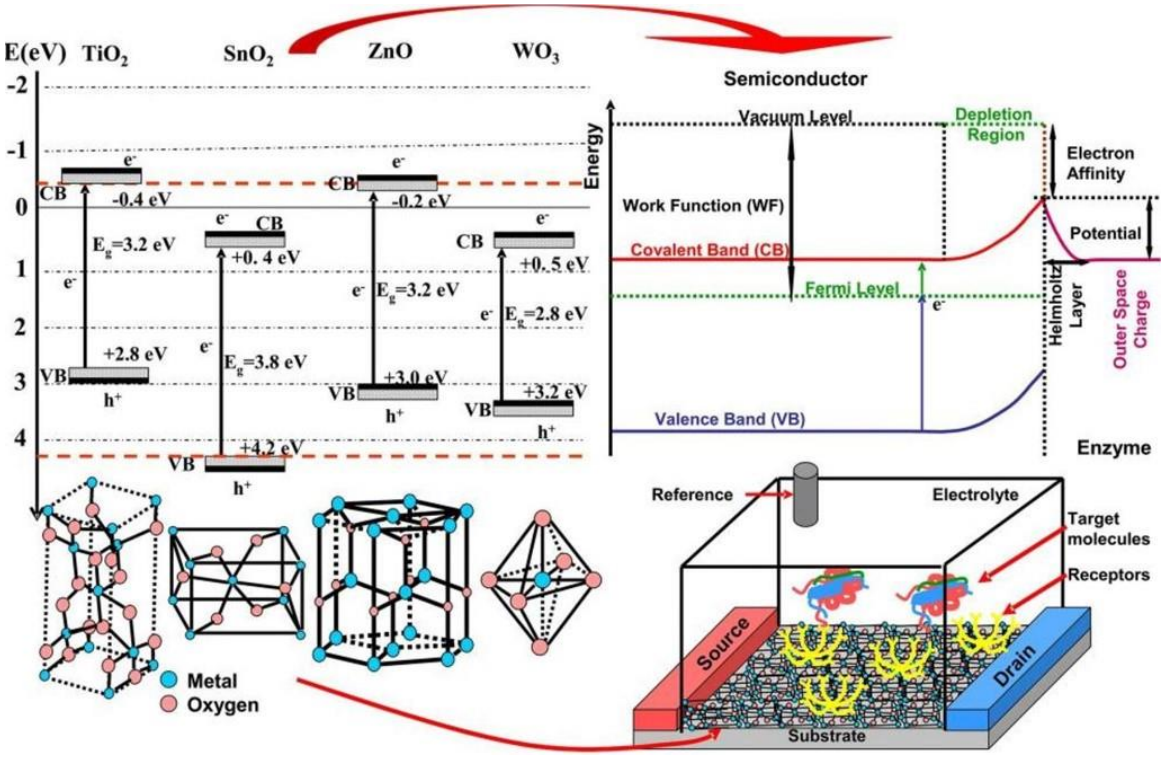

Figure 3.4 Typical MOS biosensors used: band energies and structure. Reproduced from Serban et al., 2020[92]

The most commonly used MOS based biosensors is shown in **Figure 3.4**. As the demand for real-time personalized healthcare monitoring continues to grow, metal-oxide semiconductor (MOS)-based biosensors are emerging as transformative tools in bioelectronics and biotechnology[92,93]. MOS-based biosensors have garnered significant attention due to their distinct advantages, including exceptional sensitivity, which is critical for detecting subtle surface property changes associated with specific biomolecules in complex biological matrices.[94] The functionalizability of MOS surfaces allows for the attachment of biomolecular recognition elements, such as antibodies or enzymes, thereby enhancing selectivity and enabling precise detection of targeted biomolecules.

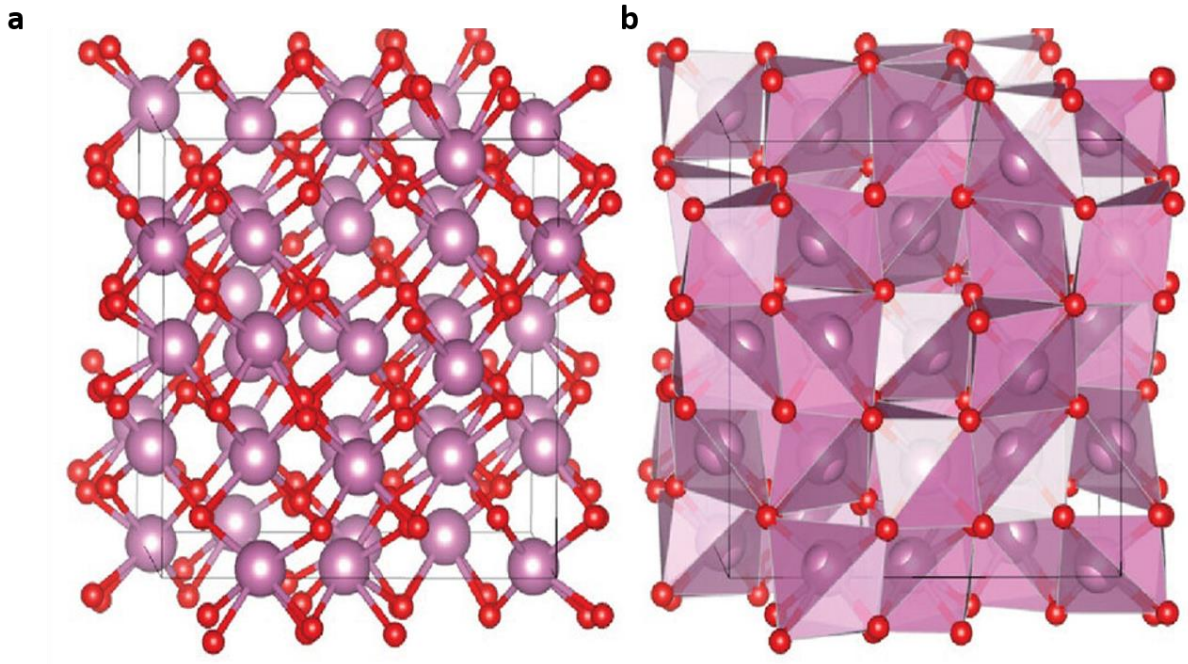

Figure 3.5 The atomic structure of crystalline indium oxide.
The red atoms represent oxygen and the purple atoms represent indium. a) Ball-and-stick model. b) Model highlighting InO_6 polyhedra. The unit cell is indicated by the thin black lines. Reproduced from Charnas et al., 2023.[95]

Metal oxides such as zinc oxide (ZnO), cuprous oxide (CuO), iron oxide (Fe_3O_4), tin (IV) oxide (SnO_2), manganese (IV) oxide (MnO_2), Indium oxide (In_2O_3) and

titanium dioxide (TiO_2) are widely utilized due to their biocompatibility, ease of synthesis, and non-toxic nature, which minimize interference with biological systems and reduce adverse reactions. These attributes, coupled with their cost-effectiveness and scalability, make MOSs highly suitable for point-of-care (PoC) diagnostics and portable sensor systems.[96] Furthermore, their long-term operational stability supports continuous and reliable monitoring, while their compatibility with miniaturization facilitates the development of advanced wearable biosensors. Specifically, indium oxide, in its crystalline state, predominantly adopts a body-centered cubic bixbyite structure, characterized by lattice parameters of approximately $a = 1.01\ nm$ and belonging to the space group *Ia-3*[97]. This structure comprises a relatively large unit cell containing 80 atoms, which is organized as an ordered arrangement of smaller polyhedral units, where each indium atom is coordinated with six oxygen atoms, as depicted in **Figure 3.5a**. A detailed view of these polyhedral arrangements is illustrated in **Figure 3.5b**. In the amorphous phase, the polyhedral units are preserved; however, there is an increased prevalence of corner-sharing connections and a reduction in edge-sharing interactions[98,99].

The semiconducting behaviour of these oxide materials arises from oxygen vacancies and metal interstitials in n-type oxides, while corresponding structural defects are responsible for p-type conductivity. In terms of electronic structure, the conduction and valence bands are derived from the overlap of metal ns orbitals and oxygen 2p orbitals. This configuration results in a highly dispersive conduction band and a localized valence band, leading to a significantly lower effective mass for electrons compared to holes. Consequently, n-type oxide semiconductors exhibit substantially higher electron mobility than their p-type counterparts, making them especially suitable for applications requiring high-speed charge transport and efficient signal transduction. This paradigm shift toward oxide semiconductors,

particularly n-type materials, underscores their critical role in advancing large-area electronics and biosensing technologies.[100] Their unique combination of transparency, scalability, and electronic properties positions them as key enablers for the next generation of flexible and cost-effective devices.

3.4 Materials & Methods

3.4.1 Lipid Ink preparation

All phospholipids, i.e., DOPC (1,2-dioleoyl-sn-glycero-3-phosphocholine), POPS (1-palmitoyl-2-oleoyl-sn-glycero-3-phospho-L-serine (sodium salt) and Rho-PE (1,2-dioleoyl-sn-glycero-3-phosphoethanolamine-N-(Lissamine rhodamine B sulfonyl)) were purchased from Avanti Polar Lipids (USA). The chloroform used as solvent was HPLC grade, from Sigma–Aldrich (Germany).

3.4.2 Indium oxide precursor ink

To create the channel for the oxide semiconductor through printing, we formulated a precursor solution. This solution comprised 0.05 M of indium nitrate hydrate ($In(NO_3)_3.xH_2O$), dissolved in a mixture of 8 ml of water and 2 ml of glycerol. After thorough mixing, the solution was filtered using polyvinylidene fluoride membrane filters with a pore size of 0.2 µm. The resulting precursor ink was then deposited onto ITO patterned substrates using a Dimatix DMP 2831 inkjet printer, with stage heated at 35°C. After printing, the devices were sintered at 400°C.

3.4.3 Proteins

Streptavidin from Streptomyces-avidini and BSA were purchased from Merck-Darmstadt, Germany. SARS-CoV2 Spike His Protein was purchased from R&D sytems, Mineapolis, USA.

3.4.4 Immobilization of Streptavidin

Initially, the surface was washed with PBS to remove excess lipids. Subsequently, 10 µL of PBS was added to measure the impedance of the bare electrode with lipids. Following this measurement, a 5 wt% BSA solution was added to the device, which was then incubated for 30 minutes. Post-incubation, the device was washed twice with PBS, and 10 µL of PBS was added to measure the impedance of the immobilized BSA on the surface. Thereafter, the surface was gently washed with PBS, and varying concentrations of streptavidin were applied to the electrode surface. After a 30-minute incubation, the device was washed twice with PBS before measuring the final impedance corresponding to the different streptavidin concentrations.

3.5 Structure and Deposition

3.5.1 Dip-Pen Nanolithography

Dip-pen nanolithography operates Dip-pen nanolithography (DPN) operates on the foundational principles of atomic force microscopy (AFM).[101] In DPN, the AFM tip, instead of being utilized for imaging, serves as a nanoscale "pen" for material deposition. The tip is first dipped into a liquid ink reservoir and then brought into contact with a substrate under controlled humidity conditions. This process facilitates the direct deposition of ink molecules through a water meniscus formed between the tip and the substrate, achieving lateral resolutions as fine as 100 nm.[102] The tip's motion is precisely controlled by piezoelectric actuators, enabling accurate patterning.

Early DPN experiments employed AFM tips to pattern organic thiol molecules, such as octadecanethiol (ODT) and mercaptohexadecanoic acid (MHA), onto gold substrates. The resulting feature sizes were influenced by parameters such as ink viscosity, dwell time, and ambient humidity.[103–106] Due to the small molecular

dimensions of thiols, the lithographic results were analyzed using AFM in lateral force mode. Subsequent advancements in DPN introduced organic inks with optical readouts, such as fluorescence microscopy[107], thereby expanding its application scope.

A significant milestone in DPN development was the transition from single-tip lithography to massively parallel patterning using two-dimensional cantilever arrays with up to 55,000 pens.[76,108] This innovation enabled high-throughput fabrication and introduced the capability for creating three-dimensional surface patterns using modified DPN techniques.

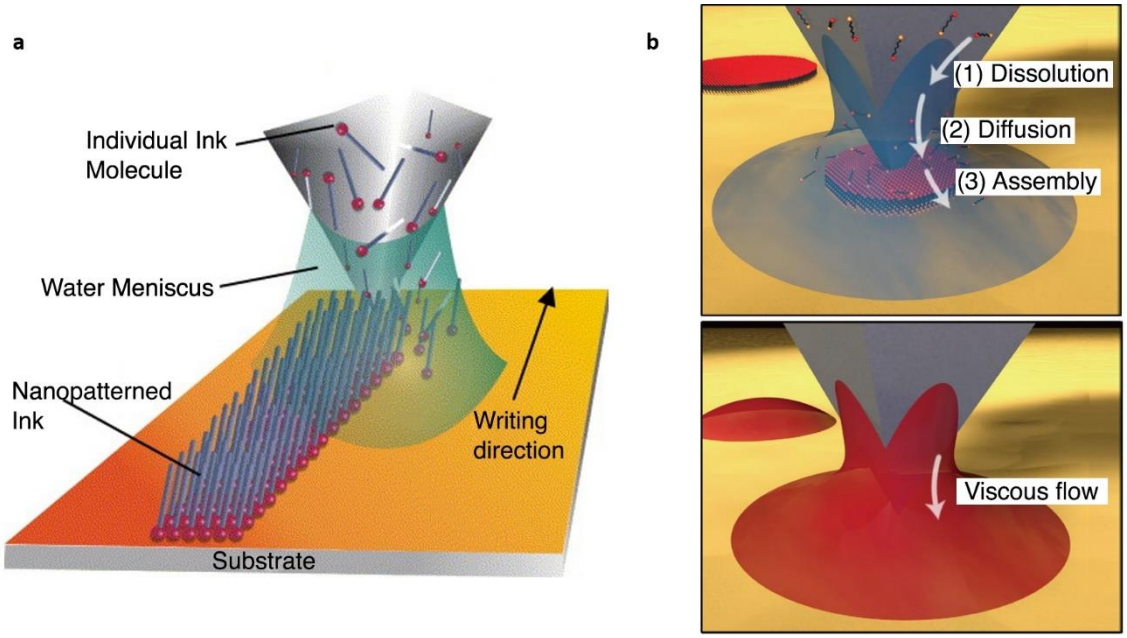

Figure 3.6 Schematic of the principle and working of DPN
a) Schematic of the L-DPN writing process. Reproduced from Haaheim et. Al.[109] b) Mechanism of transport of molecules through the water meniscus to the surface. Reproduced from Brown et al.,2013.[110]

DPN has been successfully employed for depositing a wide variety of materials, including proteins, DNA, nanoparticles, quantum dots, and even inks containing bacterial cells. However, the technique has found its most significant applications

in the field of biology. A particularly noteworthy material for biological applications is phospholipids, which are essential components of cell membranes.

L-DPN specializes in the deposition of phospholipids, such as dioleoyl phosphatidyl choline (DOPC), a major constituent of biological membranes. DOPC is often used as a carrier lipid in combination with functionalized lipids like 1-hexadecanoyl-2--(9Z-octadecenoyl)-sn-glycero-3-phospho-L-serine (POPS) and Phosphatidylinositol 4,5-bisphosphate (PIP2).[111,112] During the writing process (**Figure 3.6**), lipid mixtures spontaneously organize into neatly stacked membrane structures on the substrate.[113] This technique is particularly advantageous due to its nanoscale precision and the elimination of harsh chemical solvents or complex lift-off processes. To enhance scalability and throughput, specialized tips such as M-type(12 pens) and F-type have been developed for parallelized DPN.[114] These tips enable multiplexing, allowing the incorporation of different inks into a single pattern. This innovation has transformative implications, particularly in materials discovery.[115] For example, F-type tips equipped with 32 pens can simultaneously screen 32 different drugs, significantly accelerating the process and reducing complexity. **Figure 3.7** shows the optical micrographs of the A-type and M-type tips with the M-type inkwell.

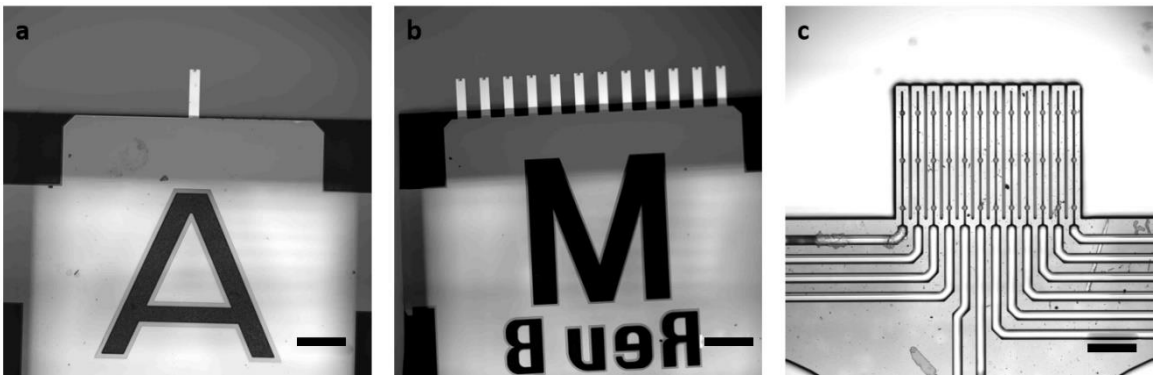

Figure 3.7 DPN cantilever and inkwell **a**) *A-type DPN cantilever. b) M-type DPN cantilever c) M-type inkwell. Scale bars equal 200 µm.*

The microfluidic inkwell (ACST, U.S.A.) was filled with 1 µL of lipid mixture (70 mol% DOPC and 30 mol% POPS). Lipid patterns were written using the DPN5000 system (Nanoink, U.S.A) with F-type cantilevers (ACST, U.S.A.) containing individual 32 pens. The cantilevers were mounted onto a holder and then dipped with the lipid mixture using a microfluidic inkwell at high humidity (≈75%). A series of test patterns were first written on a clean Si substrate to remove excess lipid ink before moving to the nanoglass/Indium oxide substrates. Here, in this thesis, all the experiments were performed with parameters kept at 2 µm/sec writing speed and 40% relative humidity. The ability to create precise, bioactive surface patterns on these substrates underscores the utility of DPN in biosensor fabrication and other advanced applications. The scalability, ease of use, and versatility of this technique make it an invaluable tool for developing nanoscale platforms in biotechnology and materials science.

Ink Transport in L-DPN: Ink transport in Lipid Dip-Pen Nanolithography (L-DPN) is a complex process that involves the transfer of materials from the AFM tip to the substrate through a well-defined sequence of stages. This process depends significantly on the physicochemical properties of the inks and their interaction with the environment, including relative humidity (RH) and substrate properties.

The DPN process for lipid inks typically involves three stages: **dissolution, diffusion, and assembly** as shown in **Figure 3.6**. Initially, lipid molecules at the AFM tip are hydrated upon exposure to water vapor in the surrounding atmosphere. This hydration allows the lipids to form a hydrated ink phase.[116]Once the tip is brought close to the substrate, a water meniscus condenses between the tip and the substrate, providing the medium for ink transport. The lipids dissolve into this meniscus at the tip-meniscus interface and migrate towards the substrate due to concentration gradients, a process governed by Fickian diffusion.[117]

At the substrate interface, lipids self-assemble into multilayer structures or bilayer membranes, depending on the environmental conditions and the lipid concentration.[105] The degree of hydration significantly affects the diffusion coefficient of lipids, dictating the rate of transport and the geometry of the deposited features.

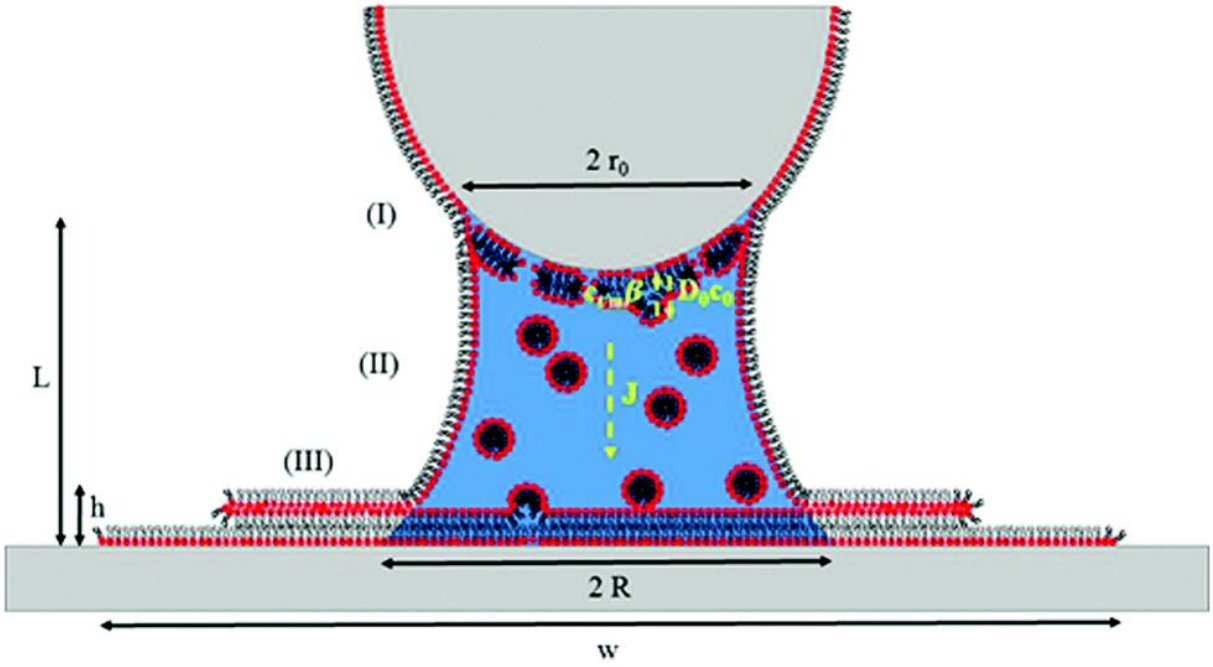

Figure 3.8 Scheme showing the three stages of ink transport of lipids via L-DPN
(I) ink-dissolution into the meniscus at the tip/meniscus interface of size $2r_{0,}$ *with a forward flow* $D_{0c0,}$ *where* D_0 *accounts for the diffusivity of the lipids with a concentration at the tip surface* c_0*, and a backward flow* $C_{tip/meniscus}\beta$*, where* $C_{tm} = C_{tip/meniscus}$ *is the concentration at the tip/meniscus interface and* β *represents the impingement and attachment rate; (II) flow J transport via a meniscus of size 2R and height L to the meniscus/substrate with an ink diffusivity D1, as a 1-D Fickian diffusion due to differences in concentrations* $C_{tip/meniscus}$ *and the concentration at the meniscus/substrate interface* $C_{meniscus/substrate}$*(III) spreading over the surface creates a 3-D circular feature with density* ρ*, width w and height h. Reproduced from Urtizberea et al.*[118]

From **Figure 3.8** for step (I), the ink detachment from tip, the net flow J can be calculated as

$$J = Doc_0 - C_{tip/meniscus}\beta \qquad (12)$$

With β being a detachment rate, assuming a gas kinetic for the flux[106]

$$\beta = \Pi r_0 \sqrt{\frac{k_b T}{2\Pi P_m}} e^{-E_A | K_b T} \tag{13}$$

After detachment, the ink has to transfer over the meniscus (Step (II)). Here, we assume the meniscus shape for the of the model as truncated cone of radii r_o and R at the top (tip/meniscus interface) and bottom (meniscus/substrate interface), respectively. With a 1D Fickian diffusion driven by concentration differences ate the tip/meniscus and meniscus/substrate interface we can describe the flow J around the meniscus as

$$J = \frac{D_1 \pi R r_0}{L} (C_{tip/meniscus} - C_{meniscus/substrate}) \tag{14}$$

Where D1 is the ink diffusivity in the meniscus and the term L/ $(D_1 \pi R r_0)$ represents the ink resistivity to flow, analogous to the resistance in an electrical circuit.

In step (III), the assembly and surface spreading of the ink, the description is more complicated for diffusive inks, as lipid ink features can grow into membrane stacks instead only as SAM structures. However, the deposited feature volume V should, for reasons of mass conservation, be related to the total flow J as

$$J = \rho \frac{V}{t} \tag{15}$$

Where t is the dwell time and S is the creature feature area. While the whole droplet feature shape is also governed by contact with the surface, the feature area S is depending on the bottom layer spreading and the accompanied flow. Taking this into account, it can be described as

$$\frac{J}{h} = \frac{J_{bottom}}{Z_t} = C_{meniscus/substrate} 2\pi \frac{Ds}{\ln(\frac{W}{2R})} \tag{16}$$

With Z_t being the bottom layer height and D_s the surface diffusivity of the substrate.

Lipid inks display a combination of liquid and diffusive properties, distinguishing them from purely molecular or liquid inks. This dual behaviour allows lipids to flow like liquids while simultaneously diffusing under concentration gradients. This combination facilitates the creation of intricate patterns with controlled geometry, which are critical for biological applications.[76] For instance, the amphiphilic nature of lipids enables them to form well-organized structures such as bilayers or multilayers, which are characteristic of cell membranes.

Relative humidity (RH) plays a pivotal role in controlling the ink's behaviour. Higher RH promotes larger meniscus formation, which enhances the flow of lipids and stabilizes the transport rate. Conversely, low RH conditions can limit the hydration of lipids, reducing their mobility and potentially altering the quality of the deposited features. The fluidity of lipid inks is further influenced by the lipid composition, including the length and saturation of carbon chains in the lipid molecules, which govern the transition temperature between solid and liquid phases.

Lipid inks like dioleoyl phosphatidylcholine (DOPC) are widely used due to their low transition temperature and high membrane fluidity under typical experimental conditions.[119] While the current understanding of lipid transport in DPN has advanced significantly, challenges remain. The dependence on environmental conditions like RH and temperature necessitates precise control during the patterning process. Furthermore, the interaction between lipids and substrates needs to be better understood to optimize deposition on non-conventional substrates such as nanoglasses or flexible polymers. Future studies focusing on the

dynamics of lipid self-assembly and the effects of substrate properties could open new avenues for designing advanced biosensors and functional biointerfaces.

3.5.2 Inkjet Printing

Inkjet printing represents a sophisticated, non-contact material deposition technique, particularly effective for creating precise patterns and structures. It operates on a *drop-on-demand* principle, ensuring controlled and minimal material usage, thereby reducing waste and enhancing precision. The fundamental mechanism involves a piezoelectric sheet integrated with the nozzles. A rough schematic of the inkjet printing is shown in **Figure 3.9**. This piezoelectric element responds to an applied sinusoidal electric potential, inducing mechanical stress that generates pressure waves. These waves propagate through the nozzle, ejecting ink droplets with highly controlled size and volume. The nozzle, typically with a diameter of around 20 µm, produces droplets approximately 10 picolitres in volume, enabling resolutions as fine as 20 µm. The nozzle's position is adjustable in three dimensions relative to the substrate, allowing precise deposition and pattern formation.

Key to achieving uniform films and accurate patterning is the concept of drop spacing, which is the distance between successive droplets. This parameter is critical as it determines whether droplets coalesce or remain discrete during deposition and drying. Alongside nozzle design, the rheological properties of the ink, such as viscosity and surface tension, are decisive in ensuring high-quality outcomes. Viscosity, in particular, governs droplet formation, flow characteristics, and film uniformity. In inkjet printing, the printability of an ink is characterized by the inverse of the Ohnesorge number (Z=1/Oh), which is a dimensionless parameter expressed as

$$Z = \frac{\sqrt{We}}{Re} \tag{17}$$

$$O_h = \frac{\eta}{\sqrt{\gamma \rho l}} \tag{18}$$

$$R_e = \frac{\rho v \cdot l}{\eta} \tag{19}$$

where W_e and R_e denote the Weber and Reynolds numbers, respectively. Optimal droplet formation occurs when $1<Z<10$. Below this range, the ink's viscosity is too high to allow proper droplet ejection, while exceeding it results in low-viscosity inks that form unwanted satellite droplets, reducing print accuracy. Typically, ink viscosity values between 1 and 10 cPs are preferred, striking a balance between smooth nozzle flow and the surface energy required for droplet cohesion.

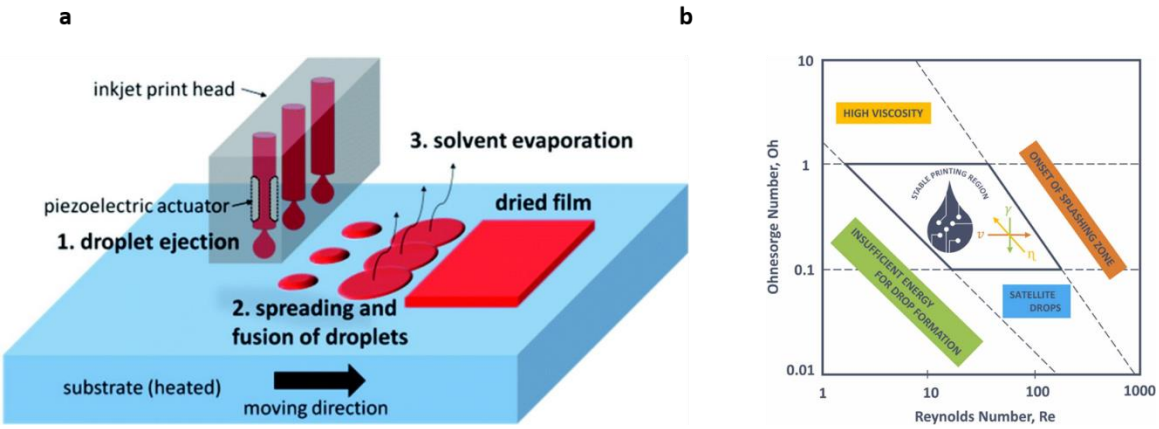

Figure 3.9 Schematic of inkjet printing and graph showing the sweet spot for printable inks *a) Schematic of Inkjet printing process b) Ohnesorge number plotted over Reynolds number, indicating the printable fluid window. Reproduced from Kacar et al.,[120] and Wu et al..[121]*

The application of a sinusoidal electric potential to the piezoelectric actuator plays a pivotal role in controlling droplet ejection. This waveform determines droplet size, volume, and velocity, influencing pattern resolution and film uniformity. Moreover, surface tension, which is inversely related to the Weber number, is

equally critical as it governs the wetting behaviour of the ink on the substrate. Substrate properties, such as surface energy, roughness, and chemical composition, significantly affect droplet adhesion and spreading. These factors can be engineered to optimize film formation and enhance the interaction between the ink and substrate.

Despite its precision, inkjet printing faces challenges, such as the *coffee ring effect*, where solute particles migrate to the droplet edges during evaporation, creating uneven deposits with thick rims and thin interiors. Strategies to mitigate this issue include solvent engineering and particle shape modification. For instance, incorporating a secondary solvent with a higher boiling point generates a surface tension gradient, altering evaporation dynamics and suppressing outward solute migration. Alternatively, using ellipsoidal particles enhances capillary interactions, promoting uniform deposition by preventing particle movement to the droplet edges.

Inkjet printing has established itself as a cornerstone technology in the fabrication of flexible and printed electronics due to its compatibility with solution-processed materials and cost-effective operation. Its ability to directly deposit electronically functional inks onto substrates without masks or vacuum systems makes it particularly advantageous for producing organic transistors, sensors, and microelectromechanical systems (MEMS). Seminal works in this domain have demonstrated the potential of inkjet-printed electronics. Sowade et al., for example, used organic inks to fabricate large scale organic thin film transistors on flexible substrates.[122] Similarly, Minemawari et al. highlighted the importance of controlling ink properties, such as surface tension, to achieve high-mobility organic single crystals for advanced electronic applications.[123]

The advantages of inkjet printing extend beyond its precision and adaptability. Its digital nature eliminates the need for traditional patterning methods such as masks and vacuum systems, reducing costs and complexity. Additionally, it is a non-contact method, mitigating contamination risks, and is compatible with roll-to-roll manufacturing, enabling the production of large-area electronics. The minimal material requirement, typically around 2 ml, further underscores its resource efficiency. Compared to other solution-based deposition techniques like spin coating and spray coating, inkjet printing offers unparalleled versatility, making it the preferred choice for producing high-resolution, cost-effective, and flexible electronic devices. Its continued evolution, driven by advancements in ink formulation and substrate engineering, promises to further expand its applications and capabilities in the field of modern electronics.

3.6 Techniques for fabrication and Characterisation

3.6.1 Scanning Electron Microscopy

In a scanning electron microscope (SEM), a tightly focused beam of high-energy electrons interacts with the sample surface, producing a range of signals that offer valuable insights into the sample's topography, composition, and other characteristics. The interactions between the electron beam and the sample are broadly classified into **elastic** and **inelastic scattering** processes.[53] The acceleration voltage and the working distance were 20 kV and 3.1 mm, respectively.

Elastic scattering occurs when the incident electrons are deflected by atomic nuclei or outer-shell electrons without significant energy loss. Electrons scattered at angles exceeding 90° are termed **backscattered electrons (BSEs)**. The intensity of the BSE signal is dependent on the atomic number of the elements in the sample, with higher atomic number elements yielding stronger signals. This property makes BSEs particularly useful for analysing both the morphology and composition of

materials. However, the spatial resolution of BSE imaging (~1 µm) is inferior to that of secondary electrons (~10 nm), as BSE signals originate from a larger interaction volume within the sample.

In contrast, **inelastic scattering** involves energy loss by the incident electrons as they interact with the specimen's atomic structure. This process generates **secondary electrons (SEs)**, which are emitted when specimen atoms are ionized. Due to their low energy (< 50 eV), SEs escape only from a shallow depth of a few nanometers below the sample surface, making them ideal for capturing detailed surface morphology. Beyond BSEs and SEs, the electron beam interaction also produces additional signals, such as characteristic X-rays, Auger electrons, and cathodoluminescence. Characteristic X-rays are essential for determining the chemical composition of samples, while Auger electrons provide chemical mapping and surface chemistry information.[124–126]

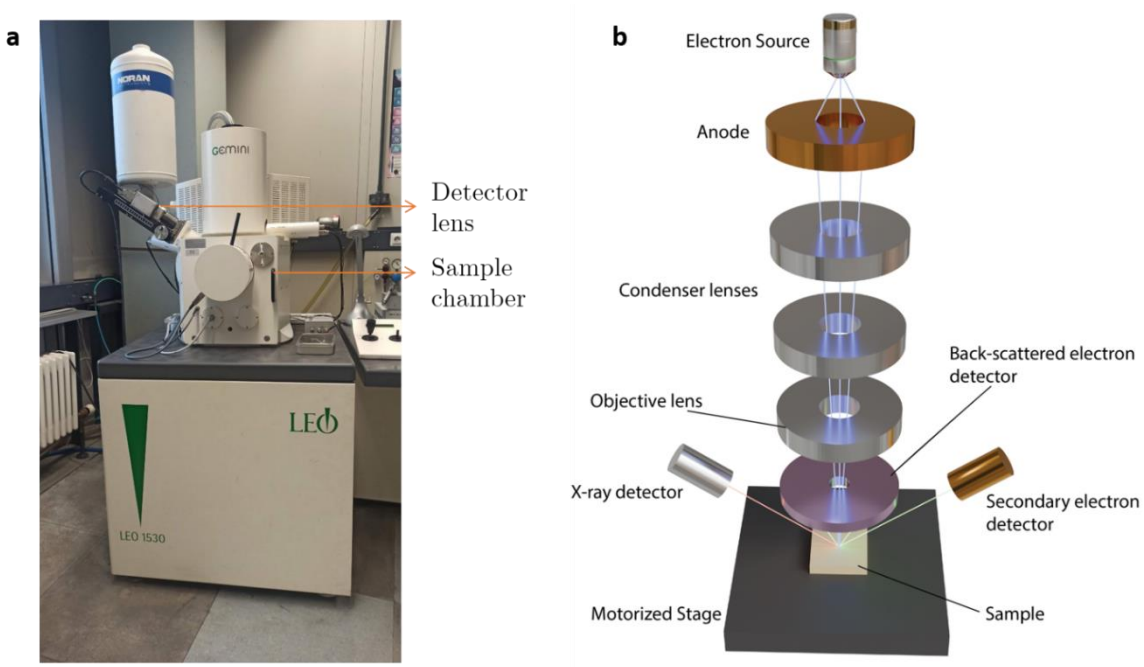

Figure 3.10 Working and principle of SEM.
a) *SEM Setup at INT, KIT. b) Working of the SEM and the interaction of Electron beam source with the sample.*

A typical SEM setup consists of several key components: an electron gun to generate the electron beam, a condenser lens to control the beam diameter, an objective lens to focus the beam onto the sample, detectors to capture SE and BSE signals, and a display unit to visualize the resulting images[126] and is shown in **Figure 3.10**. SEM can be applied to a wide variety of materials, including metals, ceramics, semiconductors, and biological specimens. However, non-conductive samples often require a conductive coating (e.g., a thin layer of gold or carbon) to mitigate charging effects during analysis. Additionally, SEM instruments generally operate under high-vacuum conditions to prevent electron beam deflection and ensure precise imaging.

In this thesis, experiments were performed with the acceleration voltage of 20 kV and working distance of 3.1 mm.

3.6.2. Atomic Force Microscopy

The atomic force microscopy (AFM) images were acquired using a Dimension Icon AFM system (Bruker, Germany) operating in tapping mode under ambient conditions. For imaging lipids and the surfaces of indium oxide and nanoglasses, Tap300AI-G (Budget Sensors) probes were used with resonance frequency of 300 kHz and force constant of 40 N/m. Data collection was conducted using NanoScope 9.7 software, while image processing and analysis were performed using the open-source software WsxM.[127] Collected data were flattened using either simple flatten or flatten discarding regions from the WsXM software for both nanoglasses and printed phospholipids for form removal.

Atomic force microscopy is a high-resolution surface characterization technique capable of resolving surface features at atomic scale, including both lateral and vertical dimensions. As a member of the scanning probe microscopy (SPM) family, AFM employs a nanoscale sharp tip to raster-scan the sample surface line-by-line.

The scanning mechanism and imaging outcome are influenced by the operating mode of the AFM system.

As depicted in **Figure 3.11** a nanoscale tip attached to the free end of a cantilever serves as a spring-like probe. As the tip approaches the sample surface, it is influenced by forces both attractive and repulsive – originating from the sample surface. These interactions cause the cantilever to bend, resulting in deflections at the tip. A laser beam is focused on a reflective coating on the back of the cantilever, and the deflected beam is detected by a split photodetector. When the tip encounters surface irregularities, such as elevations or depressions, the laser beam's reflection shifts on the photodetector. These positional shifts are converted into electronic signals, amplified, and processed to generate a detailed three-dimensional (3D) surface profile.

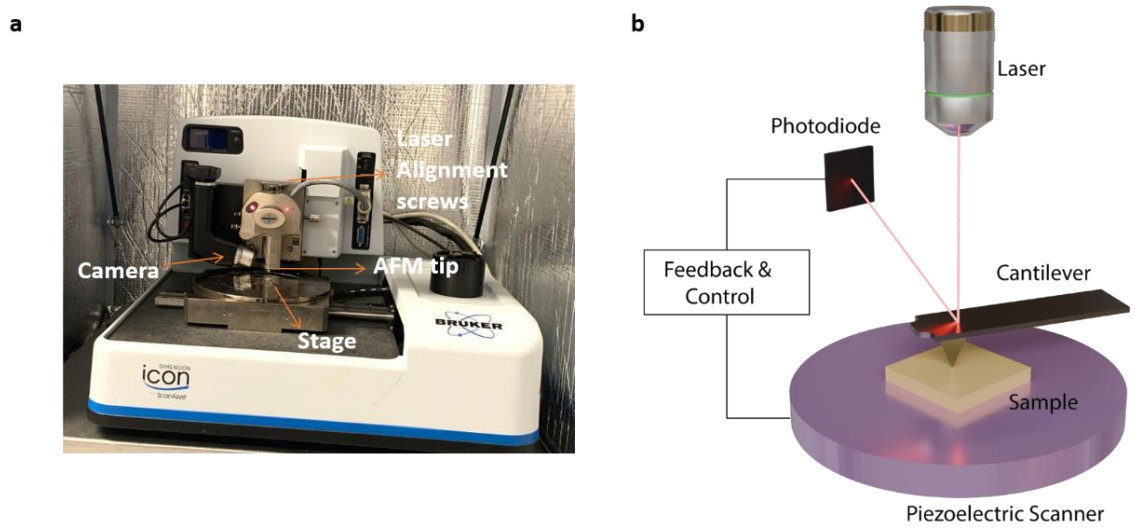

Figure 3.11 Working and principle of AFM
a) AFM from Bruker (Dimension Icon) at INT. b) Working of the Atomic force microscopy.

AFM can operate in two primary modes: **static (contact mode)** and **dynamic (tapping mode)**. In contact mode, the tip maintains constant contact with the surface, with an electronic feedback loop controlling the tip-sample interaction to ensure constant cantilever deflection. In contrast, tapping mode minimizes direct

contact, thereby reducing potential damage to both the sample and the tip. In this mode, the cantilever oscillates near its resonance frequency, and interactions with the surface modulate the amplitude of oscillation. A feedback mechanism adjusts the tip position to maintain constant oscillation amplitude, enabling high-resolution mapping of surface topography.

AFM provides not only surface morphology but also a wealth of additional information, including roughness and mechanical, electrical, magnetic, ferroelectric, piezoelectric, and thermal properties. For further insights into AFM principles, operations, and applications, comprehensive discussions are available in references.[128,129]

3.6.3 Contact Angle measurements

The sessile drop method is a fundamental technique for determining the water contact angle (WCA) on surfaces. In this method, a liquid droplet is carefully deposited on the surface, and the contact angle is measured at the three-phase contact point where the liquid interfaces with the solid and air. This is typically achieved through high-resolution digital imaging and computational analysis, which can also estimate surface energy when multiple liquids are employed. To minimize artifacts, the droplet size is kept small to reduce gravitational effects, and measurements are conducted before significant evaporation occurs. Additionally, dynamic adaptations of the method, such as recording time-dependent contact angle changes or tilting the surface to observe sliding behaviour, offer deeper insights into wetting phenomena. For this thesis, WCA measurements were performed using the sessile drop method, with the average of three independent measurements taken for each sample to ensure precision and repeatability.

3.6.4 Optical Microscopy

An upright Nikon Eclipse 80i optical microscope, equipped with a Nikon DS-Qi2 camera equipped with a TexasRed filter and a broadband excitation light source (C-HGFIE Intensilight from Nikon), was employed for imaging. The subsequent analysis and measurements of the devices were conducted using the NIS-Elements imaging software. In this thesis, optical microscopy was majorly used to image the L-DPN printed phospholipids and the inkjet-printed indium oxide.

Operational Principle:

Optical microscopy, often referred to as light microscopy, facilitates the magnified visualization of microstructures by employing visible light and a system of lenses. Its speed and ease of operation make it an indispensable preliminary characterization tool for imaging microscale patterns. The process begins with the placement of a sample on the microscope stage, where illumination from a light source is directed onto the substrate. A mirror reflects the light upwards through the sample, allowing it to pass into the objective lens, which provides the initial magnification of the image. This intermediate image is further magnified by the eyepiece lens, acting as a secondary magnifying glass, to enhance the final observation.

Various illumination techniques are available to optimize contrast and visualization depending on the nature of the sample. Bright-field illumination generates a dark image against a bright background, while dark-field illumination creates a bright image against a dark background, highlighting edges and boundaries. Polarized light techniques are particularly effective for examining the crystallographic orientation of metallic samples, offering insights into anisotropic structures. Additionally, phase contrast microscopy enhances contrast by exploiting differences

in refractive indices, allowing for the detailed observation of minute features within transparent or weakly scattering specimens.

Limitations of Optical Microscopy:

Despite its versatility, optical microscopy is inherently limited by the physical properties of visible light. The diffraction limit imposes a resolution cap of approximately 200 nm, meaning two points closer than this distance cannot be distinguished, even if they are visible. Furthermore, the maximum practical magnification achievable with conventional compound light microscopes is approximately 1000x. For detailed investigations of features below this threshold, advanced imaging techniques, such as scanning electron microscopy (SEM) or atomic force microscopy (AFM), are required. These methods circumvent the resolution limits imposed by visible light, enabling the characterization of nanoscale structures with exceptional precision.

3.6.5 Magnetron Sputtering

Two different sputtering systems were used for the growth of the amorphous films. The homogenous amorphous film and the nanoglass film with the 16 nm columns were prepared using RF magnetron sputtering, while DC magnetron sputtering was employed to grow the nanoglass film with the 60 nm columns.

In the case of RF magnetron sputtering an alloy target of nominal composition of $Cu_{60}Zr_{40}$ (at.%) was used. The sputtering system was used with a fixed distance between the substrate and target of 100 mm and a target tilt angle of 20°. A background pressure prior to deposition below 5.0×10^{-8} mbar was reached in the chamber. Thin films were deposited continuously on Si (100) wafers with a native oxide layer. Sputtering was performed with the temperature of a substrate of 293 K and power of 100 W with a substrate rotation velocity of 10 rpm. Films of two types: homogenous and columnar (16 nm columns) were prepared. Homogenous

films were deposited at a working pressure of 2.8×10^{-3} mbar and a constant Ar flow rate of 40 sccm. Columnar films were deposited at a working pressure of 8×10^{-3} mbar and a constant Ar flow rate of 100 sccm. **Figure 3.12** shows the magnetron sputtering setup with the DC and RF chamber and the main differences has been listed in **Table 2**.

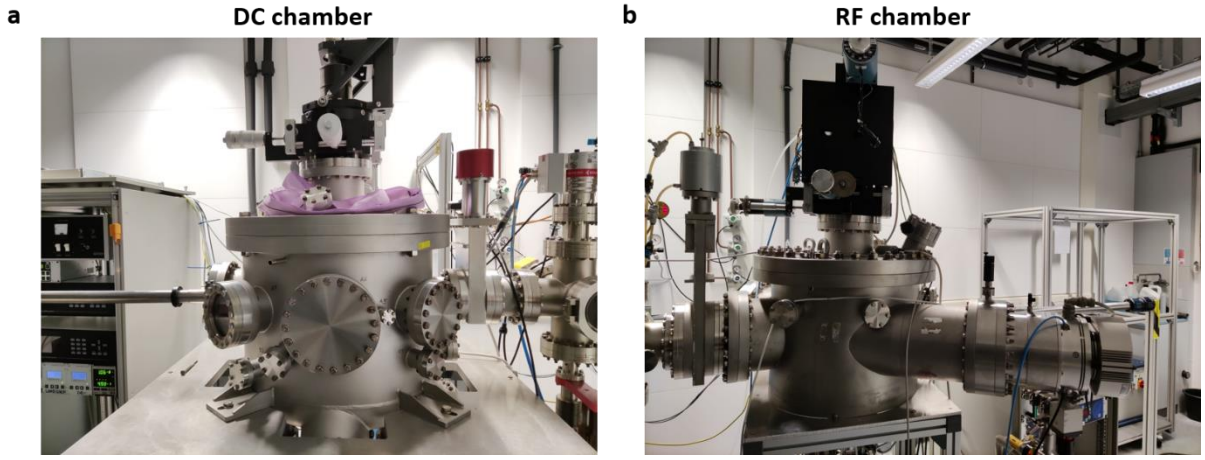

Figure 3.12 Lab setup of Magnetron sputtering.
a) DC chamber of the magnetron sputtering at INT, KIT. b) RF chamber of the magnetron sputtering at INT, KIT.

Table 2 Comparison of the DC chamber and RF chamber in magnetron sputtering used for the synthesis of CuZr nanoglasses in the thesis.

DC chamber	RF chamber
• 38° between target and substrate	• 20° between target and substrate
• RT of substrate	• RT and 200 °C substrate temperatures
• 100 mm substrate-target distance	• 100 mm substrate-target distance
• Working pressure $8x10^{-3}$ mbar	• Working pressure in range of $5x10^{-3}$ – $2.2x10^{-2}$ mbar
• Co-sputtering from Cu and Zr targets	• Sputtering from $Cu_{60}Zr_{40}$ target
• 100 Sccm Ar flow	• Various Ar flow
• No substrate rotation	• Substrate rotation

In the case of DC magnetron sputtering, the thin film samples were prepared by co-sputtering using two elemental targets of Cu and Zr with varying applied power. The sputtering system was used with a fixed distance between the substrate and target of 100 mm and a target tilt angle of 38°. The background pressure before deposition below 5.0×10^{-8} mbar was reached in the chamber. Thin films were deposited continuously on Si (100) wafers with a native oxide layer. Sputtering was performed with the temperature of the substrate of 293 K without the rotation of the substrate. Columnar films (60 nm columns) were produced using voltages of 80 W for Cu target, 100 W for Zr target, and a working pressure of 8×10^{-3} mbar.

3.6.6 Laser Ablation

Laser ablation of gold and ITO-coated substrates was performed using the TRUMPF TruMicro 5000 system to fabricate contact pads with distances (95-100 µm). The process involves high laser flux that generates plasma during material removal. Typically, laser ablation uses a pulsed laser with controlled pulse width and frequency, though continuous-wave lasers may also be employed.

Material differentiation relies on ablation thresholds, enabling selective removal of layers. In this work, gold was ablated from glass substrates due to its lower threshold, with minimal impact on the underlying material. Laser ablation is an environmentally friendly technique, eliminating the need for toxic solvents, though precautions such as fume extraction systems and protective eyewear are essential to ensure operator safety. Further details on laser ablation principles and methods can be found in references.[130,131]

III. RESULTS

Chapter 4: STABILITY-ENHANCED BIOMIMETIC LIPID MEMBRANES ON CuZr NANOGLASSES

Parts of this chapter are based on: Vasantham, S. K., Boltynjuk, E., Nandam, S. H., Eguiarte, E. B., Fuchs, H., Hahn, H., & Hirtz, M. (**2023**). Nanoscale Confinement of Dip-Pen Nanolithography Written Phospholipid Structures on CuZr Nanoglasses. Advanced Materials Interfaces, 11(2), 2300721. https://doi.org/10.1002/admi.202300721.

In this chapter, I focus on the synthesis of sputtered films exhibiting a nanograined columnar architecture—commonly referred to in the literature as nanoglasses—that is achieved through magnetron sputtering. This study investigates the interaction of these nanoglasses with biomimetic lipid membranes, emphasising the distinctive interactions that result in a unique arrangement of lipids on the nanoglass surface.

4.1 Introduction

Metallic glasses are uniquely characterised by the absence of crystalline long-range order, which precludes the presence of conventional crystal defects such as grain boundaries. As a result, homogenous metallic glasses demonstrate superior uniformity in both chemical composition and microstructure compared to crystalline materials. Recently, an innovative variant of metallic glass has been developed that consists of nanometre-scale, grain-like structures interspersed with interfacial defects. Termed 'nanoglasses', these materials are distinguished by their intricate internal nanostructuring, which differentiates them from traditional homogenous metallic glasses.[132] Structurally, nanoglasses are reminiscent of nanocrystalline materials composed of crystalline grains and grain boundaries.

However, in nanoglasses, both the core regions—analogous to the crystalline grains in nanocrystalline materials—and the interfaces—which resemble grain boundaries—are amorphous. These two components exhibit marked differences in atomic short- and medium-range order and density. Nanoglasses are primarily synthesised using bottom-up techniques, such as inert gas condensation (IGC)[133,134] and magnetron sputtering (MS).[135,136]

During IGC, amorphous nanoparticles are compacted into bulk pellets under high pressure, forming amorphous interfaces between the particles (clusters). In this study, nanoglasses were fabricated as thin films with a columnar nanostructure using MS (**Figure 2a**). Thus far, nanoglasses have been synthesised from a diverse range of binary alloys—including Si-M (M = Pd, Fe, Au, La); Ti-Pd; Au-La; Fe-Sc; Cu-Zr;[137] and Ni-Ti;[138]—and multicomponent systems such as Au-Ag-Pd-Cu-Si-Al[135] and Ti-Zr-Be-Fe-Cu.[139]

Nanostructured surfaces are generally recognised for their significant influence on cell adhesion as well as their ability to modulate cell behaviour, proliferation, and fate.[140–142] Nano-topographical structures have also been shown to play a crucial role in various bio-applications.[143,144] In this context, nanoglasses present a unique opportunity to integrate material and topographical cues. It has previously been reported that a Ti-based nanoglass exhibits a tenfold increase in osteoblast proliferation compared to a conventional (homogenous) metallic glass of the same chemical composition.[145] Identifying the underlying reasons for this pronounced difference between the two amorphous structures and exploring the effects of topography and material composition are significant challenges. Cells interact with surfaces via their outer membrane, which consists of a complex assembly of phospholipids (as structural components) and an array of proteins involved in adhesion, material exchange between the cell's interior and exterior, and signalling.

Since the structural state of the membrane can influence protein function[146,147] and plays a role in how cells sense their environment[148,149], understanding how phospholipids interact with nanoglass surfaces and how these interactions alter the lipid membrane is a critical first step in deciphering cell-surface interactions.

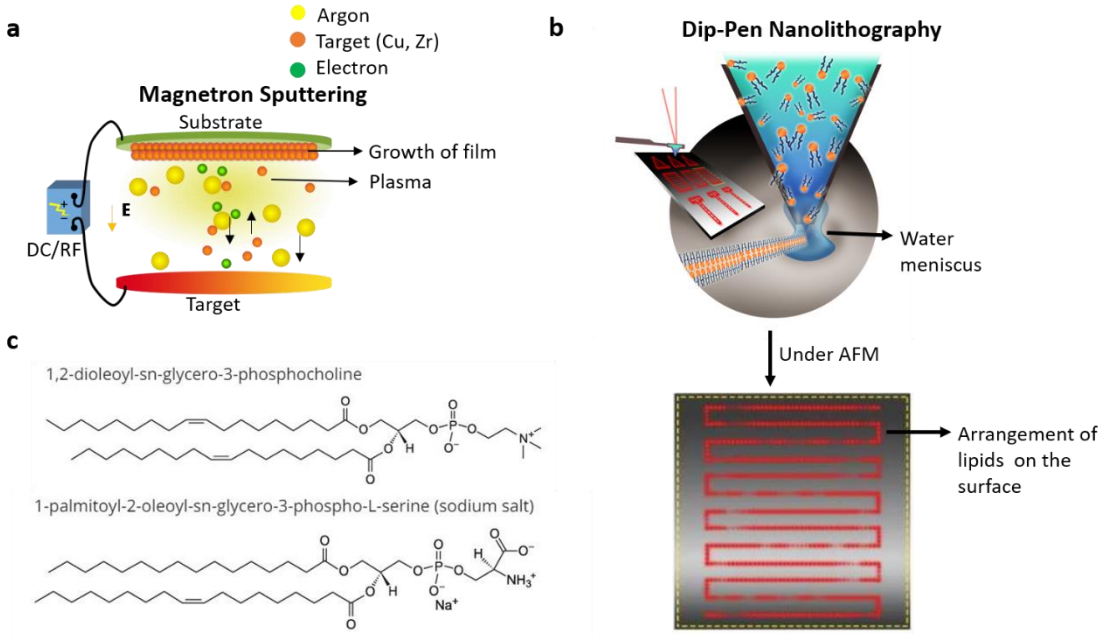

Figure 4.1 Schematic of fabrication of nanoglasses and lipid printing.
a) Schematic illustration of the magnetron sputtering used for the synthesis of nanoglasses. b) Lipid dip-pen nanolithography processes. c. Chemical structure of the written phospholipids (DOPC and POPS).

Here, I investigate the interaction of $Cu_{60}Zr_{40}$ nanoglasses, produced by MS, with biomimetic lipid membranes patterned using dip-pen nanolithography (L-DPN).[101,150] Dip-pen nanolithography for lipid patterning has been applied to a wide variety of substrates, including silicon, glass, polymers, graphene, polystyrene, and titanium.[40,151,152] L-DPN employs an atomic force microscopy (AFM) tip, dipped into a lipid mixture as ink (with 1,2-dioleoyl-sn-glycero-3-phosphocholine (DOPC) as the main carrier), to deposit biomimetic lipid membranes onto surfaces (**Figure 4.1**). L-DPN has been used in biomedical applications such as drug delivery, cell culture, biomarker detection, cancer cell detection, and protein

screening.[153–155] The overall behaviour of these lipid membranes under various substrates is influenced by factors such as wetting properties, surface roughness, and morphology, which make them effective probes for surface characterisation.

4.2 Synthesis and Characterisation of CuZr Nanoglasses

To minimise experimental complexity and focus on the interaction between nanoglasses and biomimetic membranes, specifically phospholipids, I opted to investigate $Cu_{60}Zr_{40}$ nanoglasses with varying columnar dimensions. This study aimed to compare the behaviour of lipid membranes on nanoglass surfaces with column sizes of 0 nm, 16 nm, and 60 nm. Initially, the experimental plan was to include columns up to 200 nm, as this resolution is compatible with lipid deposition via L-DPN. However, fabrication limitations restricted the maximum achievable column size to 60 nm, necessitating the use of these dimensions for the study. The working parameters to attain the specific composition have been shown in **Table 3**. Different compositions of CuZr nanoglasses were fabricated using magnetron sputtering (**refer to Chapter 3**). The X-ray diffraction studies confirm the amorphous nature of the synthesised nanoglasses. No crystalline peaks were seen in the samples even after annealing the samples for different compositions as shown in **Figure 4.2**. The EDS analysis proves the different elemental composition of the CuZr nanoglasses and the columns.

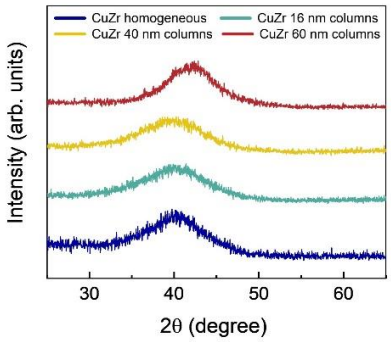

***Figure 4.2 XRD of the CuZr** homogenous, 16 nm, 40 nm, and 60 nm columnar nanoglass samples.*

Table 3. Various sputtering conditions and their corresponding chemical composition of the synthesised CuZr nanoglasses using magnetron sputtering.

Sample	Sputtering conditions	Working pressure (Pa)	Working Power (W)	Chemical composition, at. %	
				Cu	Zr
Homogeneous	RF, binary target	2.8×10^{-1}	100 for CuZr	58.55 ± 0.38	41.45 ± 0.38
16 nm columns	RF, binary target	8×10^{-1}	100 for CuZr	56.38 ± 0.48	43.62 ± 0.48
40 nm columns	DC, two elementary targets	8×10^{-1}	45 for Cu, 100 for Zr	54.69 ± 0.31	45.31 ± 0.31
60 nm columns	DC, two elementary targets	8×10^{-1}	80 for Cu, 100 for Zr	68.69 ± 0.28	31.31 ± 0.28

The structural characterisation of the films was conducted using scanning electron microscopy (SEM) to assess both the overall morphology and the dimensions of the columnar features (**Figure 4.3 a–c**). Given the critical influence of surface roughness on lipid deposition, AFM was employed to further investigate the surface topography of the films. Notable differences in surface roughness were observed across the samples, with average roughness values measured at (0.1 ± 0.1) nm for the homogeneous films, (0.8 ± 0.1) nm for the 16-nm columns, and (2.8 ± 0.6) nm for the 60-nm columns (**Figure 4.3 d–f**).

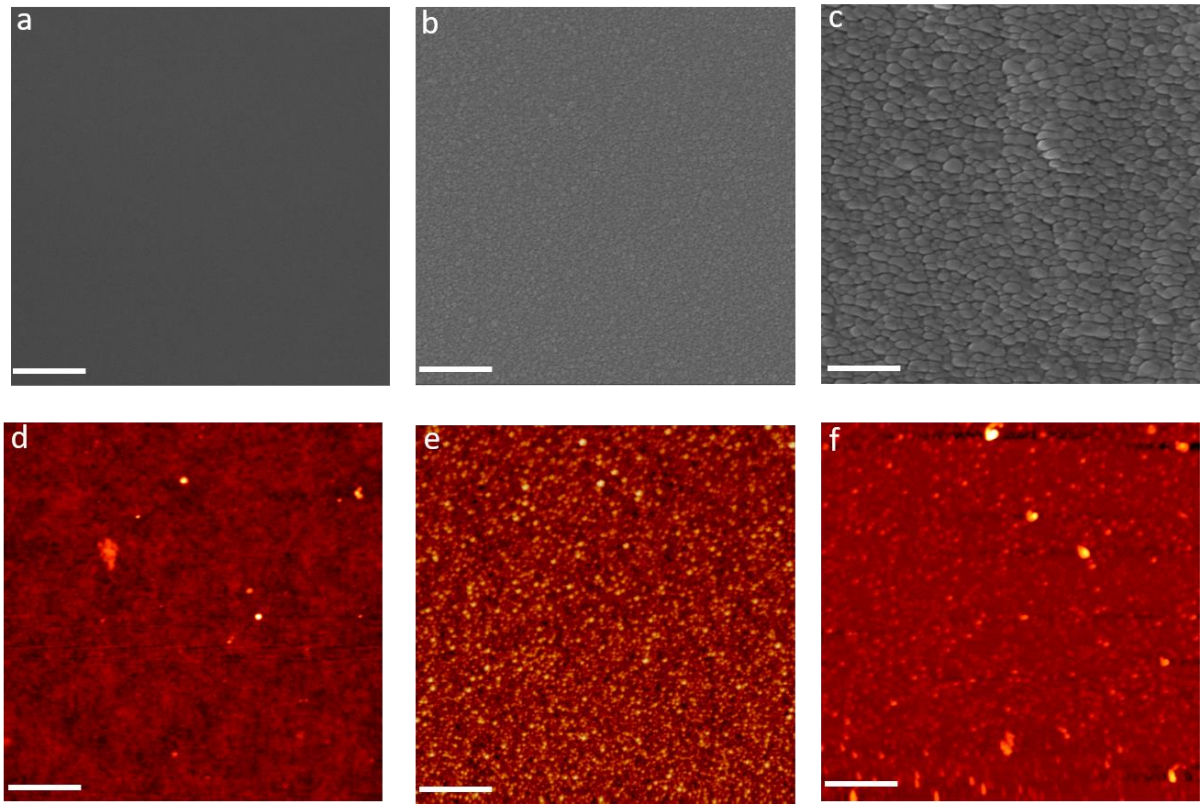

Figure 4.3 SEM images of surface topography of a) homogenous, b) 16-nm column, and c) 60-nm column films.
Scale bars for (a–c) equal 200 nm. Surface morphologies of the thin d) homogenous, e) 16-nm column, and f) 60-nm column films. Scale bars for (d–f) equal 1 µm.

The water contact angle (WCA) is a key metric for evaluating the wetting behaviour of a surface, which is crucial for understanding its interaction with biomolecules. This is particularly important in the context of lipid deposition via dip-pen nanolithography (DPN), as the wetting properties of the substrate directly influence the adsorption, spreading, and overall organisation of lipids on the surface. Consequently, precise characterisation of WCA is essential for optimising surface-lipid interactions and achieving controlled lipid patterning. WCA was measured for homogenous, 16 nm and 60 nm columnar films as shown in **Figure 4.4**. It was found that the CuZr films are hydrophobic, with insignificant differences in the contact angles (homogenous: 96.2°; 16 nm columnar: 98.1°; and 60 nm columnar: 98.6°). These findings indicate that the deposition of lipids onto the

surface of these films is not expected to exhibit significant variation across different substrates.

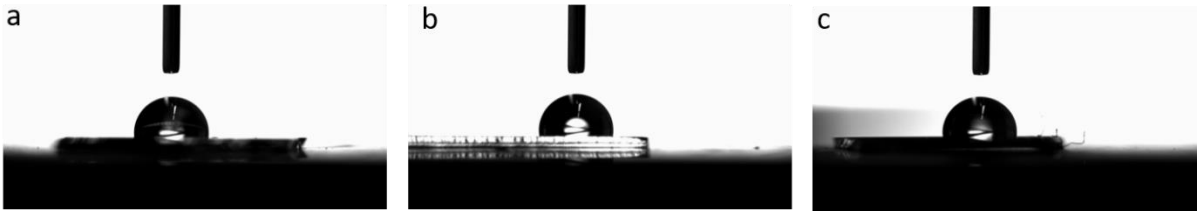

Figure 4.4 Contact angle measurement on *a) a homogenous film, b) a 16-nm columnar film, and c) a 60-nm columnar film.*

4.3 Lipid Dip-pen Nanolithography on Nanoglasses

The schematic representation of the L-DPN writing process, along with the lipid patterns created in this study, is depicted in Figure 1. For the lipid mixture used in L-DPN, a solution containing 70 mol% 1,2-dioleoyl-sn-glycero-3-phosphocholine (DOPC) and 30 mol% 1-palmitoyl-2-oleoyl-sn-glycero-3-phospho-L-serine (POPS) was selected. While a wide variety of lipid mixtures are commonly employed as biomimetic models of the cell membrane,[156] the choice of the DOPC/POPS combination was based on its proven efficacy in L-DPN applications as well as its prevalent use in biophysical studies. To facilitate the imaging of the patterned structures using fluorescence microscopy, the lipid mixture was doped with 1 mol% of 1,2-dioleoyl-sn-glycero-3-phosphoethanolamine-N-(Lissamine rhodamine B sulfonyl) (Rho-PE). As a test pattern for L-DPN, various geometric shapes—triangles, squares, and T-shapes—were defined with hatch lines spaced at 400 nm intervals to ensure different writing orientations and angles relative to the writing tip (**Figure 4.5**). The same conditions and pattern were applied to print a neutral lipid mixture, composed of DOPC and rhodamine, onto the substrates (**Figure 4.6**).

L-DPN was successfully performed on all three films, producing the intended patterns as shown in **Figures 4.5** and **4.6**. However, a noticeable difference can be

observed in the optical micrographs. On the homogeneous substrate, the hatch lines have merged, resulting in smoother patterns, whereas, on the columnar nanoglasses, the hatch lines remain distinguishable. Additionally, the outlines of the shapes are less defined on the homogeneous substrate. This distinction suggests increased spreading of the lipid membrane stacks on the homogeneous surface. Surface wettability plays a pivotal role in the spreading of lipid features during L-DPN and, thus, influences the merging of the hatch lines. On substrates sufficiently hydrophilic to promote a 'heads to substrate' membrane orientation—typically observed on surfaces such as glass and silicon oxide—the membranes written in the air form a monolayer configuration with subsequent layers of 'tail out' membranes.[113] Conversely, on substrates with greater hydrophobicity, L-DPN results in a 'tails to substrate' membrane configuration, leading to direct stacking of 'tail out' membranes in air, without the formation of an initial monolayer.[40] These contrasting orientations and stacking behaviours have also been observed in comparisons of L-DPN on hydrophilic graphene oxide and hydrophobic graphene, as further validated by molecular dynamics simulations.[157]

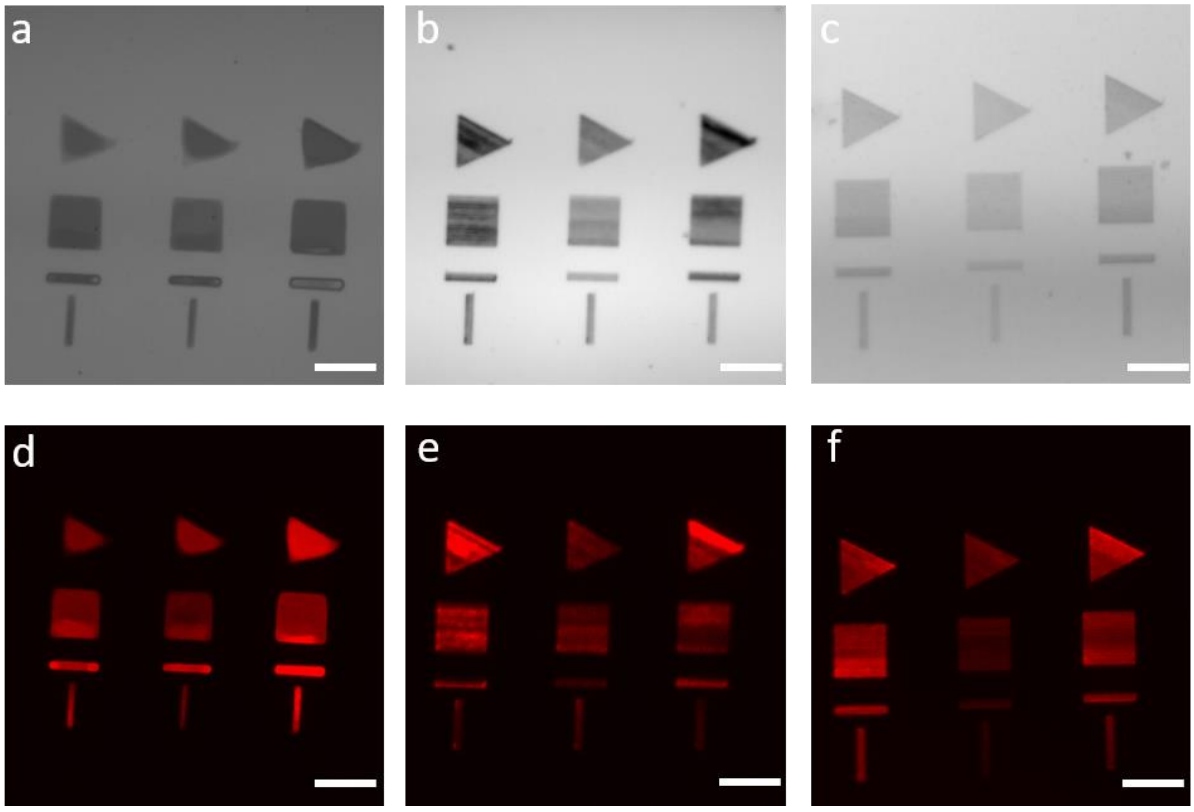

Figure 4.5 Optical bright field and corresponding fluorescence microscopy images of patterned phospholipid structures.
a) and d) homogenous Cu60Zr40; b) and e) 16-nm columns; and c) and f) 60-nm columns. The lipid structures on homogenous film show—in contrast to the ones on the columnar nanoglasses—the spreading of the lipids, resulting in less-defined structures. Scale bars equal 15 µm for all images.

A similar behaviour was observed in the ink containing only DOPC-rhodamine, where the hatch lines on the homogeneous films merged, while those on the 16-nm and 60-nm columnar films remained distinct and visible. Additionally, lipid spreading during deposition typically results in the formation of monolayers or bilayers, depending on the hydrophobic or hydrophilic nature of the substrate.[158] Structures generated by L-DPN in the air tend to spread more extensively on hydrophilic surfaces—which exhibit lower WCA, indicating higher surface energy—as has been demonstrated in comparisons of glass and polystyrene substrates[151] as well as the hydrophilic/hydrophobic, self-assembled monolayers used in L-DPN.[159] However, it is important to note that exceptions to this trend have been observed, such as the 'tails out' membrane configuration written by L-DPN on graphene,

likely due to the strong interaction between graphene and the carbon tails of phospholipids.[40] In general, the spreading behaviour in L-DPN can be viewed as analogous to the behaviour of supported lipid bilayers in liquid environments,[160] although lipid mobility is typically greater in water than in air, which can be exploited to merge hatch lines into continuous membranes when transferred to liquid.[154]

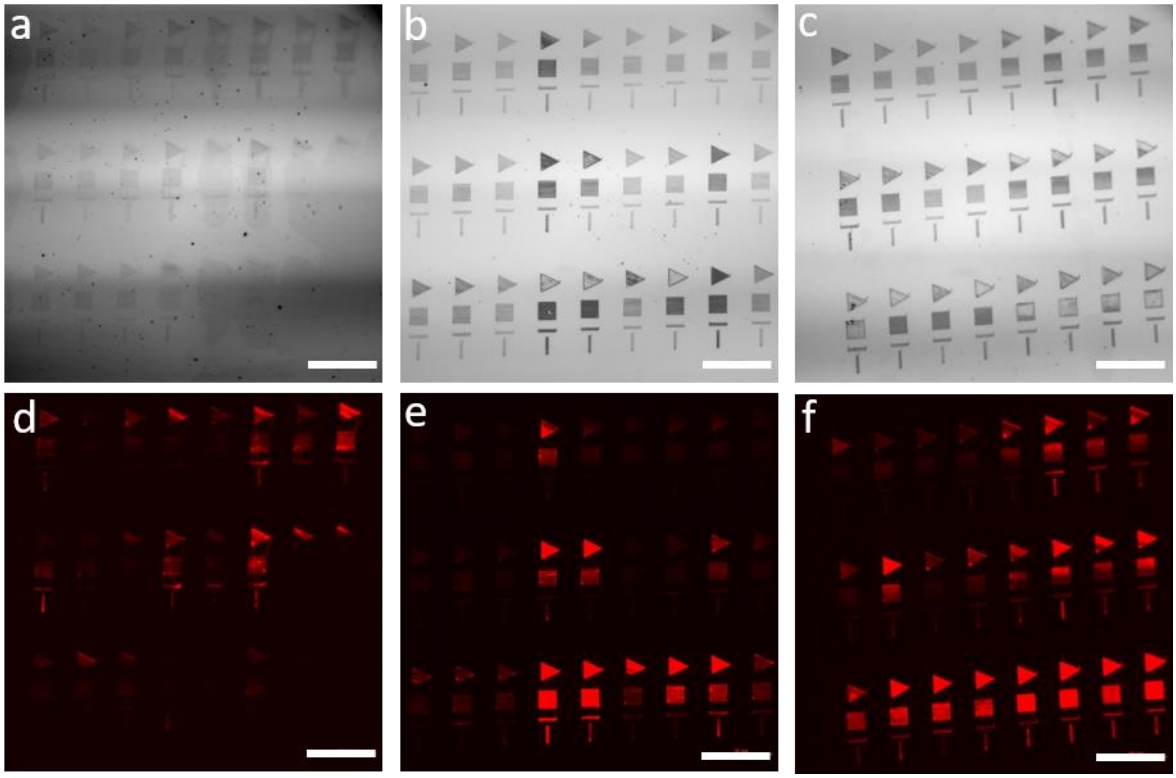

Figure 4.6 Optical micrographs of lipid dip-pen nanolithography written structures on various substrates using DOPC with Rho-PE admixing as phospholipid ink.
a) b) and c) show bright field images of homogenous; 16-nm and 60-nm columnar films and d) e) and f) show corresponding fluorescence images. Scale bars equal 50 µm.

In the present study, however, the WCA values for the three substrates are quite similar- (96.2 ± 0.6)°, (98.1 ± 3.3)°, and (98.6 ± 1.6)° for the homogeneous, 16-nm, and 60-nm films, respectively (see **Figure 4.4**) and these differences in WCA do not appear to be large enough to account for the significant variations in spreading behaviour. Furthermore, while the surface roughness of the films is

notably different, it also does not seem sufficient to fully explain the differences observed in the spread. Although nano roughness can affect the phase state and mobility of lipids in liquid environments,[161] the roughness variation between the homogeneous and 16-nm columnar nanoglass (0.1–0.8 nm) is comparable to that observed in typical L-DPN substrates, such as silicon with a native oxide layer (≈0.1 nm) and glass surfaces (≈0.2–1.9 nm), wherein no such abrupt changes in spreading behaviour have been reported.[162–164]

4.4 Surface Characterisation of Printed Lipids on $Cu_{60}Zr_{40}$ Films

To gain deeper insight into the morphology of the lipid structures, AFM imaging was employed across all samples. Despite maintaining consistent writing conditions for all substrates, notable differences in surface structure were observed. On the homogeneous substrate, the lipids formed flat layers with an approximate height of 6 nm (**Figure 4.7a**). In contrast, on the 16-nm (**Figure 4.7b**) and 60-nm (**Figure 4.7c**) columnar substrates, the hatch lines of the lipid structures (with a pitch of 400 nm) remained distinctly visible, with average heights of approximately 50 nm and 30 nm, respectively.

To further quantify these differences in spreading behaviour, systematic experiments were conducted under identical writing conditions on freshly prepared substrates, and AFM images were used to calculate the average area covered and volume deposited. **Figure 4.8b** presents the average area covered by square patterns on each substrate, while **Figure 4.8a** compares the average volume deposited during printing. In summary, the results demonstrate that under constant writing conditions across all substrates, the confinement of phospholipids on the columnar nanoglasses results in more well-defined lipid structures. While the material flow to the surface remains unchanged, leading to a nearly constant deposited volume, the area covered by the lipids is significantly reduced.

Consequently, the lipid structures on the columnar nanoglasses are taller, as the lipids are restricted from spreading, compared with the flatter, more dispersed structures observed on the homogeneous glass.

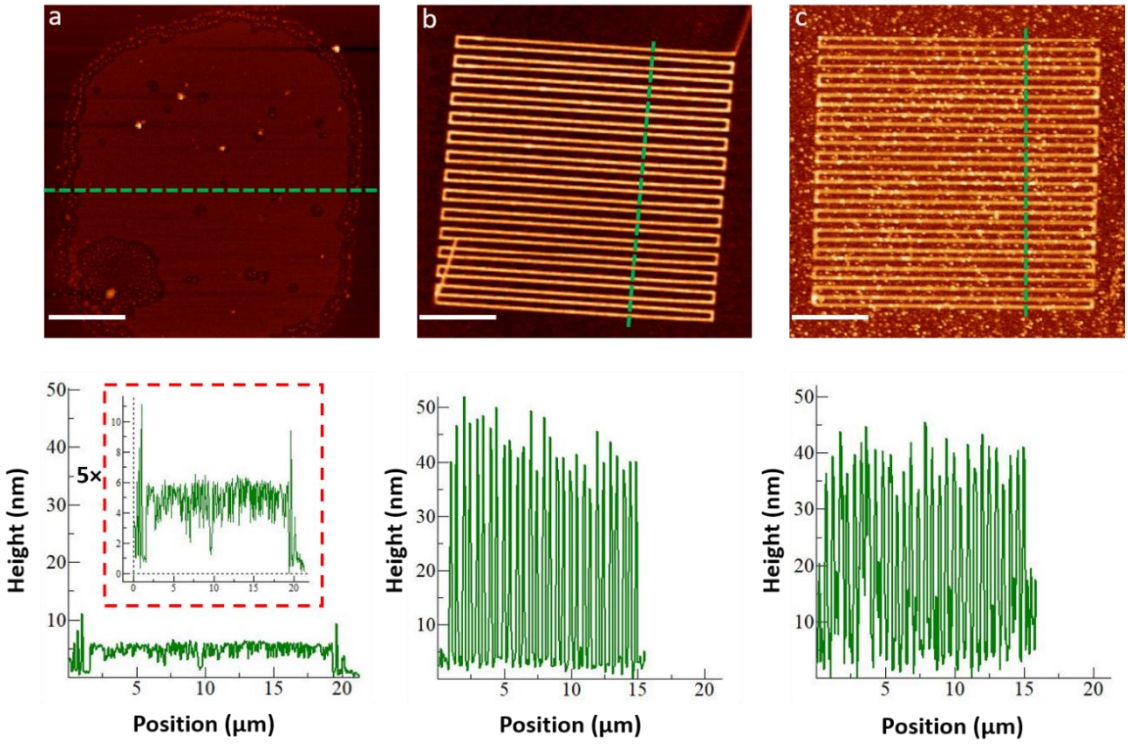

Figure 4.7 AFM topographic images after lipid patterning on different substrates.
a) The homogenous film shows the complete spreading of lipids and the corresponding profile shows a height of 6 nm. b) The 16-nm film shows the stability of lipids with heights of 50 nm. c) The 60-nm columnar also shows good stability with a variable height of 30 nm. Scale bars equal 4 µm.

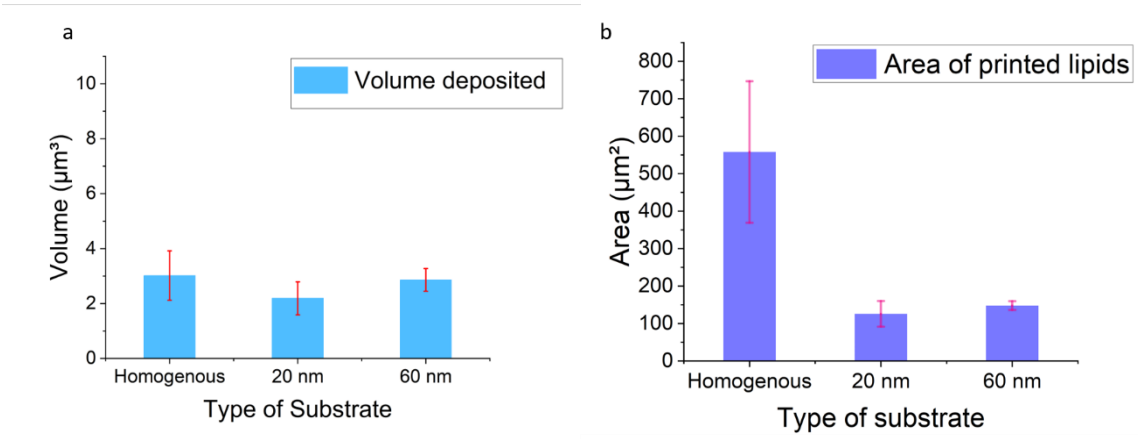

Figure 4.8 Panels a) and b) show the average area and volume of the lipids patterned (from six measurements each).

4.5 Nanoscale Confinement of Phospholipids on Columnar Nanoglasses

Examining the finer details of the patterns formed on the columnar substrates via AFM, the data (**Figure 4.7**) reveals the most striking observation: the lipids organise into distinctive structures of regular lines that are perpendicular to the direction of the hatch line writing. In areas where the hatch lines are noncontinuous (**Figures 4.9a and 4.9b**), unusual grenade-shaped lipid patches are observed, aligning perpendicularly to the writing direction. Despite the supporting nanoglass having an average column size of 16 nm, these lipid features exhibit diameters of (110 ± 33) nm along the writing direction for the main structure and (42 ± 9) nm for the smaller side feature. To rule out any imaging artefacts caused by a double-tip, the structures were re-scanned with a fresh AFM tip. Notably, the columnar features of the substrate did not exhibit any corresponding side features. The most plausible explanation for the appearance of these peculiar lipid structures is that they were generated unintentionally during the writing process, potentially due to the DPN tip picking up material and forming a double tip. This serendipitous occurrence has yielded a compelling insight: nanoconfinement on the nanoglass substrates enables the formation of features smaller than typically achieved with L-DPN, wherein the standard line width is approximately 100 nm.

For the continuous hatch lines (**Figures 4.9c and 4.9d**), the regular pattern condenses into stripes that are oriented perpendicular to the hatch-line-writing direction. In this case, the substrate employed had a column size of 60 nm, yet the periodicity of these perpendicular stripes was measured to be (44 ± 6) nm, which is even smaller than the object size observed on the 16-nm columnar substrate.

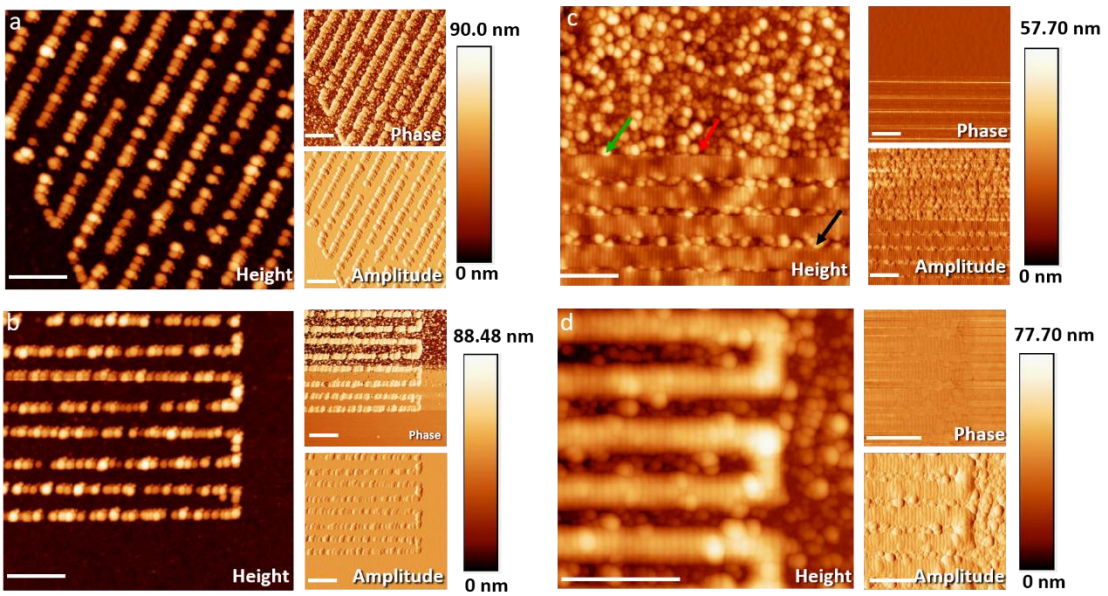

Figure 4.9 Zoomed-in AFM images of square and triangle patterns of lipids from the 16-nm columnar substrates and 60 nm substrates

16 nm columnar nangolasses shown in a) and b) and the 60-nm columnar substrates shown in c) and d). The arrows in c) indicate the step pinning arrangement. The scale bar equals 1 µm for all images.

These nanoscale arrangements were not observed consistently across all written patterns, and they appear to diminish as the structure height increases (**Figure 4.10, Figure 4.11, Figure 4.12 and Table 4**). The stripes also form perpendicular to the fast-writing direction of the AFM tip (**Figure 4.13**), which suggests that this phenomenon may be substrate-mediated either during the writing process or through reorganisation afterwards. This could influence the arrangement of the initial membrane layers whereas subsequent layers become increasingly decoupled. Interestingly, the size of these objects and the periodicity of the stripes do not correspond to the domain sizes of the substrate, indicating that this pattern formation cannot be attributed solely to alignment with the underlying domains.

Table 4. An overview of the observation of stripe substructure on 16-nm and 60-nm columnar films.

Type of sample	Average height of lipid measured (AFM)	Nanoarrangement observed (Yes/No)
16-nm columnar	25 nm	Yes
	35 nm	Yes
	20 nm	Yes
	35 nm	No
	15 nm	No
	18 nm	No
60-nm columnar	50 nm	No
	55 nm	No
	15 nm	Yes
	35 nm	Yes
	20 nm	Yes
	40 nm	No

However, close inspection of the hatch lines reveals that the confinement and stabilisation of the lipids within these lines (contrasting the extensive spreading observed on homogeneous substrates) seem to be associated with interfacial regions of the nanoglass. This is not purely due to mechanical edge pinning, as lipid spreading halts not only at the boundaries between columns of different heights (**Figure 4.9c**, green arrow indicating high-to-low transition, black arrow for low-to-high transition) but also between columns of similar height (red arrow). It can be seen that the regular stripe substructure in the confined lipid lines appears less pronounced with increasing structural height. This indicated that each lipid layer (4-5 nm) acts as a cushion layer, thereby hindering the observations of the stripe substructure.

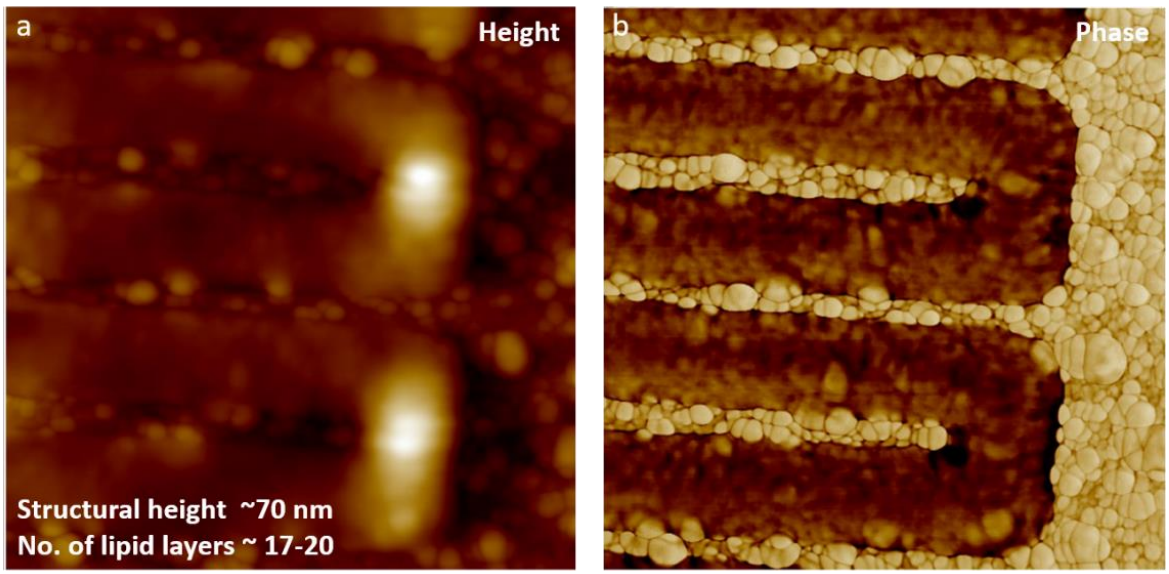

Figure 4.10 a) Topography and b) phase images of substructures in the nanoconfined lipid structures on the 60-nm columnar films for lipid structures of height 70 nm.

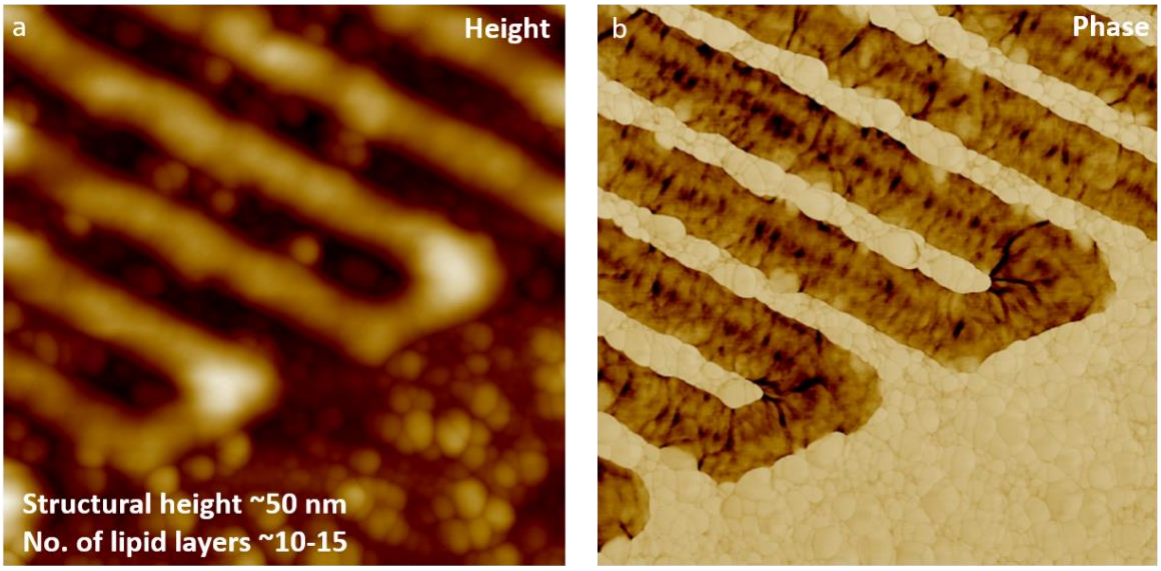

Figure 4.11 a) Topography and b) phase images of substructures in the nanoconfined lipid structures on the 60-nm columnar films for lipid structures with height about 50 nm and 10-15 lipid layers.

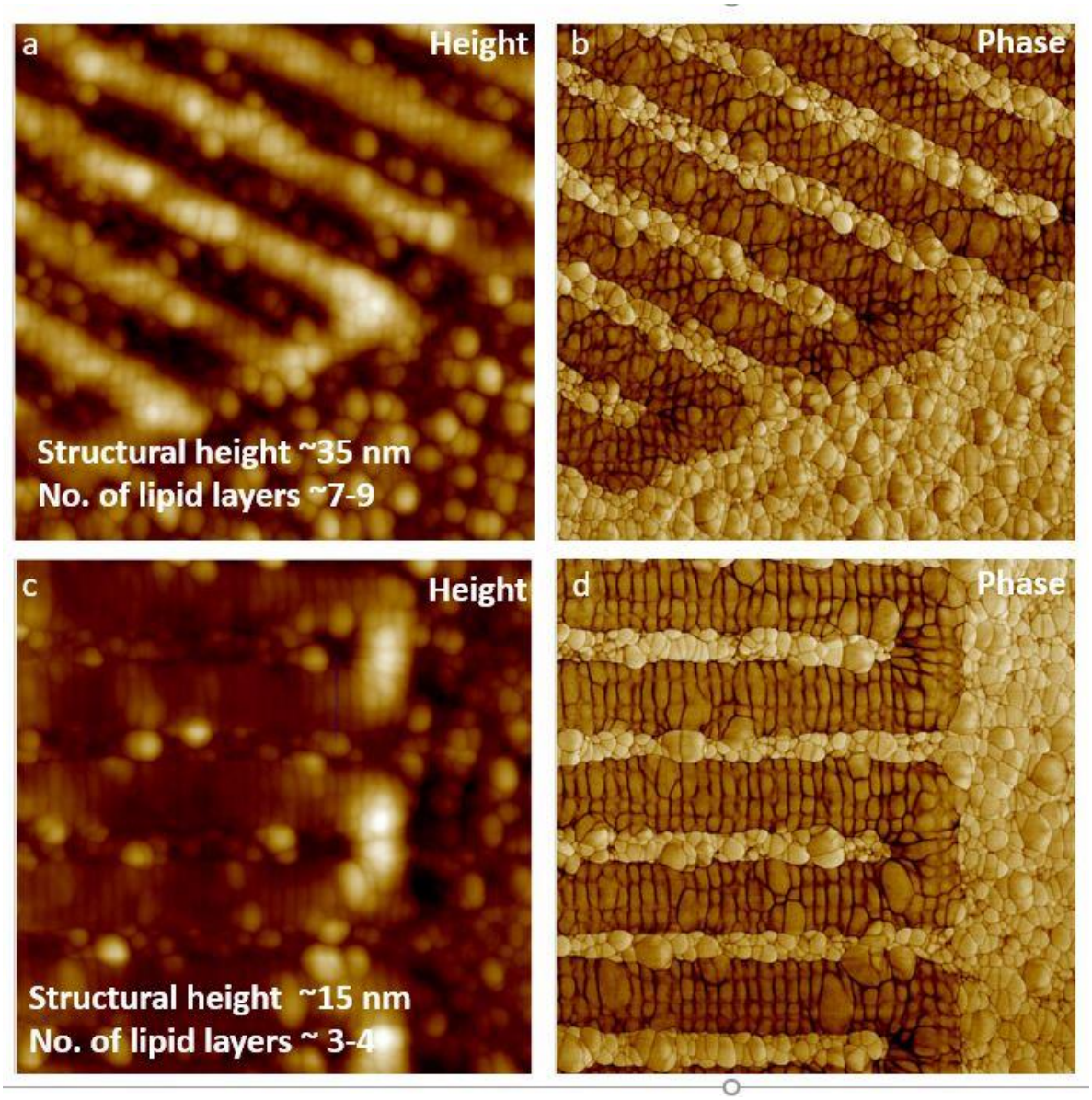

Figure 4.12 Topography and phase images of substructures in the nanoconfined lipid structures on the 60-nm columnar films for lipid structures with heights about 35 nm in a,b and 15 nm in c,d respectively.

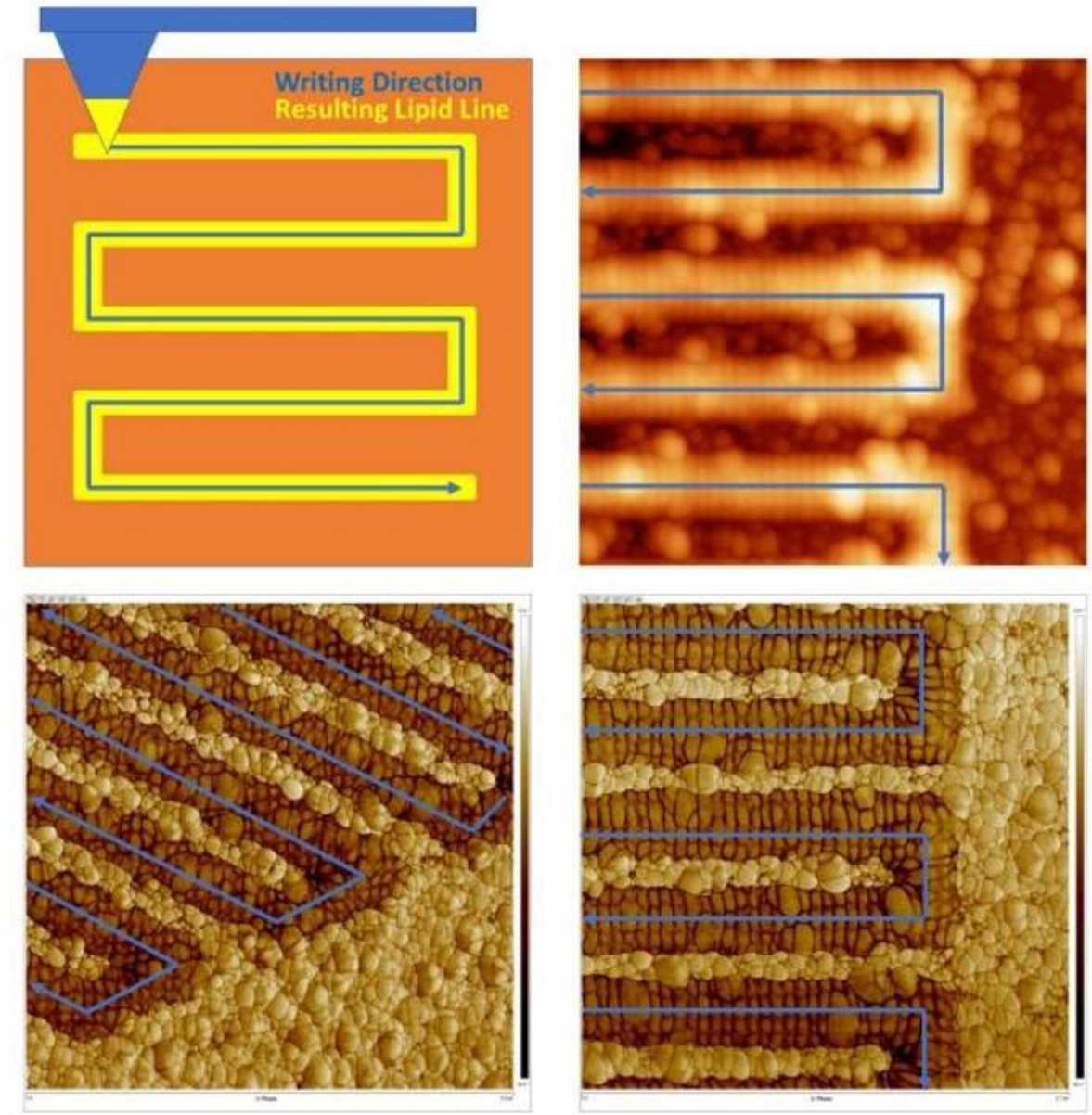

Figure 4.13 Scheme of writing directions and resulting stripe patterns.
The hatch lines of the L-DPN pattern are written in a zig-zag fashion, thus intrinsically performing different writing directions in regard to the substrate during patterning (top left). The AFM image of Figure 5d with superimposed writing path (top right). In the phase images, the resulting stripe pattern perpendicular to the respective writing direction is easier to distinguish (bottom right). Lines with smaller inclinations on the stripes are still ordered across the writing direction, though at inclination (bottom left). This is probably caused by the faster movement along the x-axis, compared with the y-axis, to generate the line that is much more extended in the x-direction than in the y-direction, with the stripes aligning perpendicular to the fastest component of the writing movement.

4.6 Discussion

Phospholipid membranes were successfully patterned on different amorphous $Cu_{60}Zr_{40}$ substrates (both homogenous and columnar) with sub-micron resolution using L-DPN (**Figure 4.5**). Striking differences in lipid spreading behaviour were observed, with the columnar nanoglasses confining the lipids more effectively than the homogenous substrates of the same composition (**Figure 4.7**). Based on these findings, a model for the nanoscopic organisation of lipid membranes on these substrates is proposed (**Figure 4.14**). The confinement of lipid structures on columnar nanoglasses is attributed to the influence of amorphous interfaces present within the 16-nm and 60-nm columnar substrates, which impede spreading. The sub-structures observed in the lower layers of the lipid hatch lines exhibit a distinct form of self-organisation, which could be linked to meniscus instabilities during the writing process (reminiscent of stripe pattern phenomena in Langmuir-Blodgett (LB) transfer of phospholipids[165]) and/or subsequent reorganisation influenced by the nanoglass substrate. In this analogy, the oscillating water meniscus in the LB transfer—that is responsible for liquid-expanded/liquid-condensed (LE/LC) phase monolayer deposition in alternating stripes—is mimicked by the meniscus formed between the DPN tip and the nanoglass surface. While in LB transfer, the substrate is lifted through the water meniscus, in DPN the meniscus itself is moved across the substrate by the DPN tip, resulting in a very similar relative motion and geometry in both cases. Similarly, the surface could induce or stabilise a ripple phase of ordered/unordered membrane segments in the written lipid lines as observed in separate lipid bilayer phases during phase transition in lipid bilayers.[166–168] This could also explain the fading seen with additional layers as they move further away and become more decoupled from the surface.

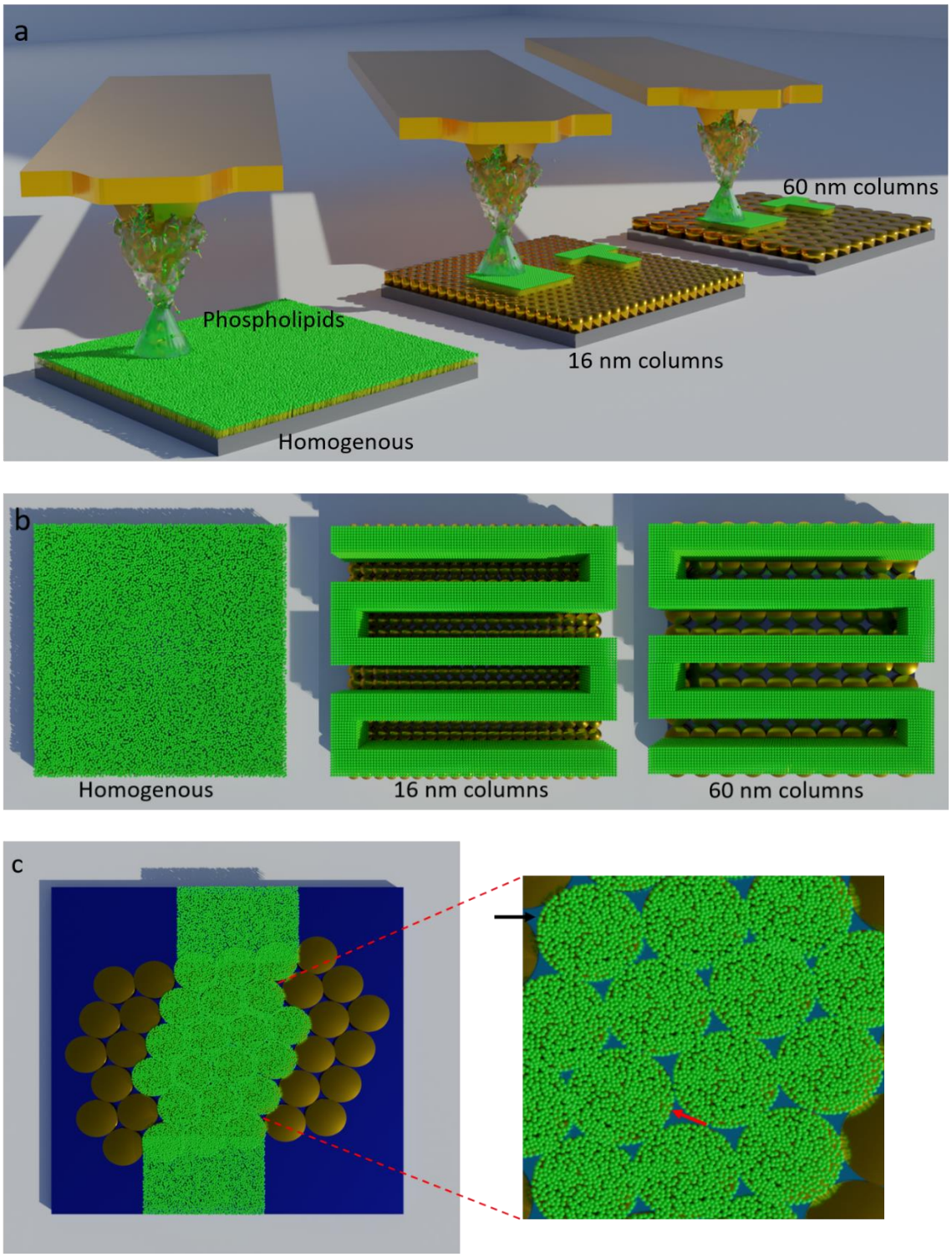

Figure 4.14 Schematic illustration of the lipid organisation on homogenous, 16-nm, and 60-nm columnar nanoglasses.

a) Patterning of phospholipids using L-DPN. b) Top view of lipid organisation after patterning. c) Scheme of stabilisation of the written phospholipid lines by halting the spreading at the boundaries of the columnar nanoglasses. The inset shows a magnified image of the influence of columnar boundaries (red and black arrows) on the stability of the phospholipids after writing.

Although these experiments—conducted with model lipid membranes in the air rather than in a liquid—differ from a realistic biological cell/nanoglass interface, the discovery of the distinct differences between the homogenous amorphous substrates and nanoglasses— with respect to lipid–surface interaction that does not rely on surface geometry but rather on the presence of columnar interfaces—provides a plausible explanation for the observed variations in cell behaviour that do not manifest on chemically and topographically similar surfaces. Since many cellular processes are modulated by the state and fine structure of their lipid membranes (e.g., through lipid-modulated proteins), nanoglass surfaces may offer unique stimuli to cells by influencing their lipid membranes. Although research on the structure and properties of columns and interfaces in nanoglass thin films remains limited, progress is being made in understanding the CuZr system.[136] It is anticipated that a correlation between the experimental findings reported in this study and structural investigations will be established in the future, enabling a deeper understanding of the processes governing lipid–nanoglass surface interactions. This would, in turn, allow for the production of nanoglass films with tailored properties either by alloying CuZr or employing systems of other chemical compositions. Furthermore, a detailed characterisation of the interfacial regions between the nanoglass columns could provide insight into the specific molecular mechanisms responsible for the confinement effect. The findings of this study could inspire future research with more realistic bio-membrane models or living cells, focusing specifically on these types of interactions.

Chapter 5: LOW-VOLUME IMPEDIMETRIC SENSOR FOR PROTEIN DETECTION

Major parts of this chapter are based on: Srivatsan K. Vasantham, Dora Zalka, Angelika Lepek, Navid Hussain, George Matthew, Evgeniy Boltynjuk, Surya Abhishek Singaraju, Jacek Ryl, Michael Hirtz* and Jasmin Aghassi-Hagmann.

Low Volume Lipid Membrane Based Impedimetric Sensor for Protein Detection. (**2024**) Small (**In-Review**).

This chapter explores the development and potential application of indium oxide—a metal oxide semiconductor—as a biosensor. The emphasis is on the unique properties of indium oxide, which distinguish it from other semiconducting materials, particularly in the context of biosensing. The study further highlights the material's suitability for full-scale printed fabrication and demonstrates how indium oxide can be combined with phospholipids to form highly sensitive and specific sensors for protein detection, particularly streptavidin.

5.1 Introduction

In contemporary diagnostics, biosensors emerge as pivotal tools, as they facilitate the detection of biomarkers in analytes with unparalleled efficiency. This capability enables clinicians to access crucial information swiftly, aiding in both treatment strategies and early detection protocols.[155,169,170] Over recent decades, extensive scientific work has been dedicated to enhancing biosensor technology, with a particular emphasis on augmenting stability, sensitivity, and rapid detection capabilities.[171–173] Among these advancements, electrochemical sensors have garnered significant attention owing to their inherent advantages, including facile sensing methodologies, label-free detection modalities, and cost-effective fabrication techniques.[172]

A common principle for electrochemical biosensors is chronoamperometry, wherein charges generated by enzymatic reactions with the analyte are detected (e.g., during enzymatic conversion of glucose into gluconic acid).[174] However, this approach is significantly limited in detecting biomolecules that do not undergo enzymatic or redox reactions. Here, electrochemical impedance spectroscopy (IS) offers a better approach, as binding of analytes to immobilised receptors can also be detected, even when no redox or enzymatic reactions occur.[175] Empirically validated applications of IS-based biosensors have demonstrated the technique's remarkable versatility in protein detection and its ability to achieve exceptional levels of accuracy for an expanding array of protein targets.[176–178]

Recent advancements in rapid screening methodologies have increasingly leveraged semiconductor-based biosensors, which offer enhanced sensitivity, precision, real-time detection, and the capability for integrated multiplex sensing.[179–183] To date, a number of printable impedimetric biosensors with low limits of detection (LOD) have been reported.[184–187] A wide variety of biosensors using semiconductors as transducer elements have been demonstrated as forms of field effect transistors (FETs), Organic Electrochemical Transistors (OECTs), Thin Film Transistors (TFTs), etc.[2,188,189]

In this study, the proof-of-principle concept of an in-plane, label-free, and biomimetic phospholipid membrane functionalised impedimetric sensor for protein detection using streptavidin as a model protein is presented. Historically, investigations into the interaction between avidin and biotin have predominantly relied on fluorescent ligands, as both entities are conventionally considered electrochemically inactive. However, recent progress has highlighted the use of electrochemical techniques for elucidating the intricate dynamics of avidin–biotin interactions, thereby enriching the arsenal of analytical approaches available for their comprehensive characterisation.[190,191] As a transducer element, I chose indium

oxide (In_2O_3), a well-established n-type semiconductor, renowned for its utility in biosensor applications. In_2O_3 can be inkjet-printed and used in multiple electronic devices as transistors and diodes.[192,193]

The devices were fabricated with In_2O_3 channel material via inkjet printing, using indium tin oxide (ITO) and gold electrodes as contacts to investigate also the influence of different contacts on the sensor performance. For immobilization of the receptor elements to the semiconductor, I functionalised the semiconductor material with biomimetic phospholipid membranes. This allows for the easy introduction of specific binding sites (here biotinylated lipids) while creating an anti-fouling surface that prohibits unwanted off-target protein adsorption.[194] For deploying the lipid membranes specifically to the device channels, I employed L-DPN, which can create phospholipid membranes on a variety of materials ranging from metals to polymers and nanoglasses.[40,112,151]

The in-plane geometry of the device together with the potential for a fully-printed production process—as well as the miniaturised design of our device with precise deposition of minute volumes of reagents—enables efficient utilisation of biomolecules, potentially reducing production costs.[195] The deployed methodologies are not only scalable but also cost effective for industrial manufacturing applications. This represents the first utilisation of a hybrid system combining inkjet-printed In_2O_3 and L-DPN patterned phospholipids for high-sensitivity detection of proteins via IS.

5.2 Device Fabrication and Characterisation

This sensor design incorporates either ITO or gold electrodes with In_2O_3 as the channel material, printed using inkjet printing with a channel length of 100 µm, serving as the primary transducer in our devices. On top of the In_2O_3, a lipid mixture comprising 1,2-dioleoyl-sn-glycero-3-phosphocholine (DOPC) and

biotinylated phosphatidylethanolamine (Biotin-PE) was patterned using L-DPN. A comprehensive depiction of the device fabrication steps is provided in **Figure 5.1.**

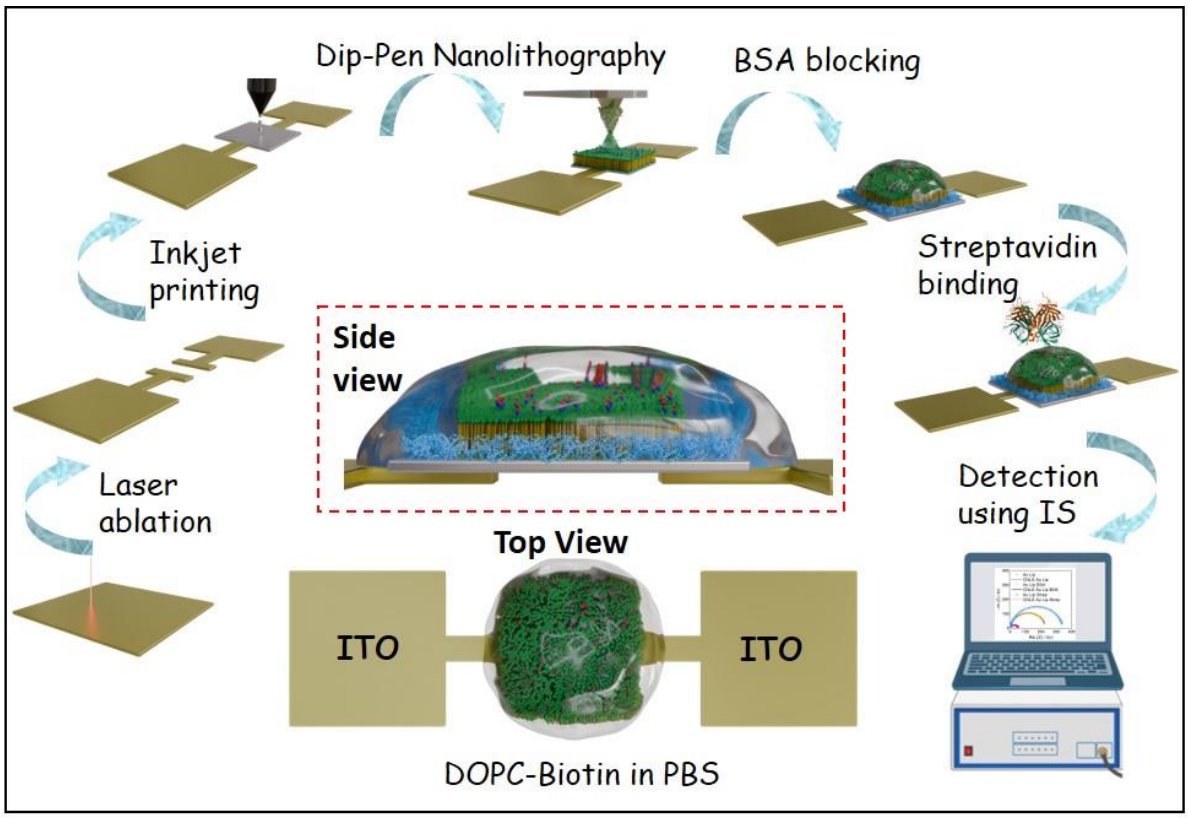

Figure 5.1 Schematic illustration of device fabrication and impedimetric sensing.

A two-electrode planar electrochemical cell configuration, as depicted in **Figure 5.1**, was employed for this biosensor platform. Two different electrode configurations (gold/In_2O_3 and ITO/In_2O_3), as the difference in work functions would result in different contacts between electrodes and the semiconductor (Ohmic vs. Schottky for ITO and gold, respectively). Molecular binding at the transducer/electrolyte interface, schematically illustrated in **Figure 5.2**, was utilised for the precise quantification and detection of streptavidin in phosphate-buffered saline (PBS).

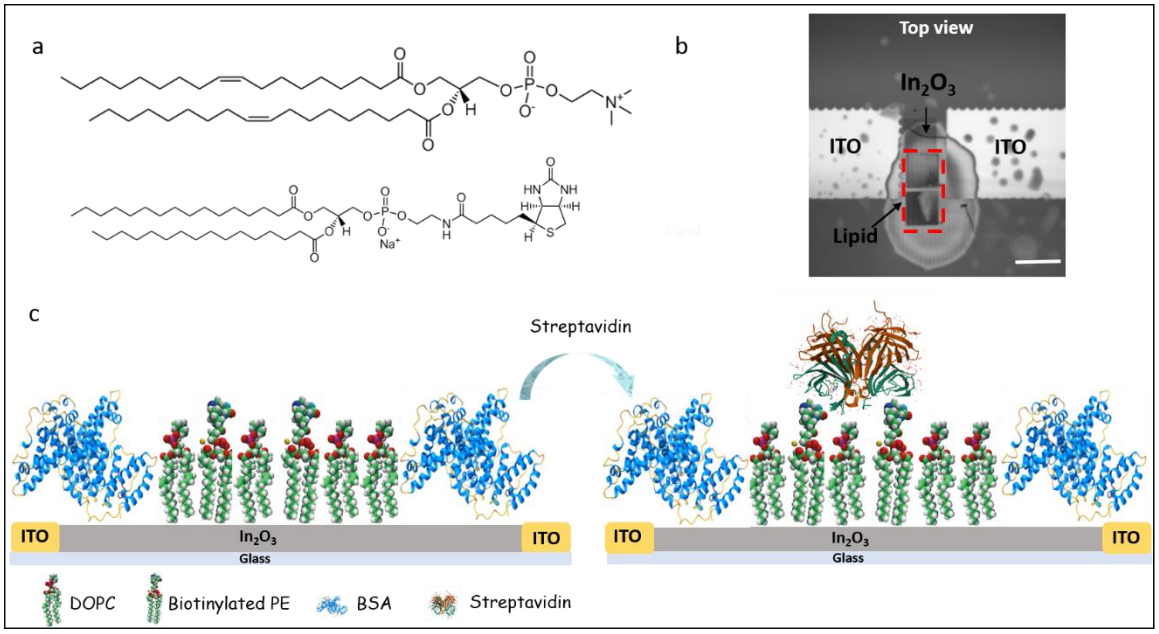

Figure 5.2 Optical microscopy of device and structures of lipid and schematic of their interaction with streptavidin.
a) Chemical structure of 1,2-dioleoyl-sn-glycero-3-phosphocholine (DOPC) and 1,2-dipalmitoyl-sn-glycero-3-phosphoethanolamine-N-(biotinyl) (sodium salt). b) Bright field image of the device structure with inkjet printer In_2O_3 and 5% Biotin-DOPC. c) Schematic illustration of the mechanism of biotin-PE binding to streptavidin following BSA blocking (side view).

Figures 5.3a and **5.3b** present AFM images of ITO and inkjet-printed In_2O_3, respectively, with root mean square roughness (r_{rms}) values of 0.116 nm and 4.253 nm, respectively. While the ITO roughness is comparable to silicon oxide surfaces that are routinely used in L-DPN, the higher roughness of the In_2O_3 is in the range of the thickness of a lipid bilayer in air (~4 nm).[37] Nevertheless, L-DPN can successfully deposit a homogeneous lipid membrane layer onto the In_2O_3, as the cohesion of the lipids within the membrane layer allows spanning over the rough substrate, with only minor penetration of the layer from some of the semiconductor film peaks. **Figure 5.3c** depicts a scanning electron microscopy (SEM) image of the printed In_2O_3 film, both with and without lipid coverage. **Figure 5.3d** illustrates the energy-dispersive X-ray spectroscopy (EDS) mapping for indium (In) and carbon (C). The EDS mapping indicates that the atomic ratio of indium is consistent between lipid-covered and non-covered areas, whereas the carbon concentration in the lipid-covered regions is nearly double that in the non-covered

regions, which indicates the presence of phospholipids in the L-DPN–functionalised area. The surface morphology of gold electrodes and optical profilometry measurements of the thickness of the In_2O_3 film are shown in **Figure 5.4**.

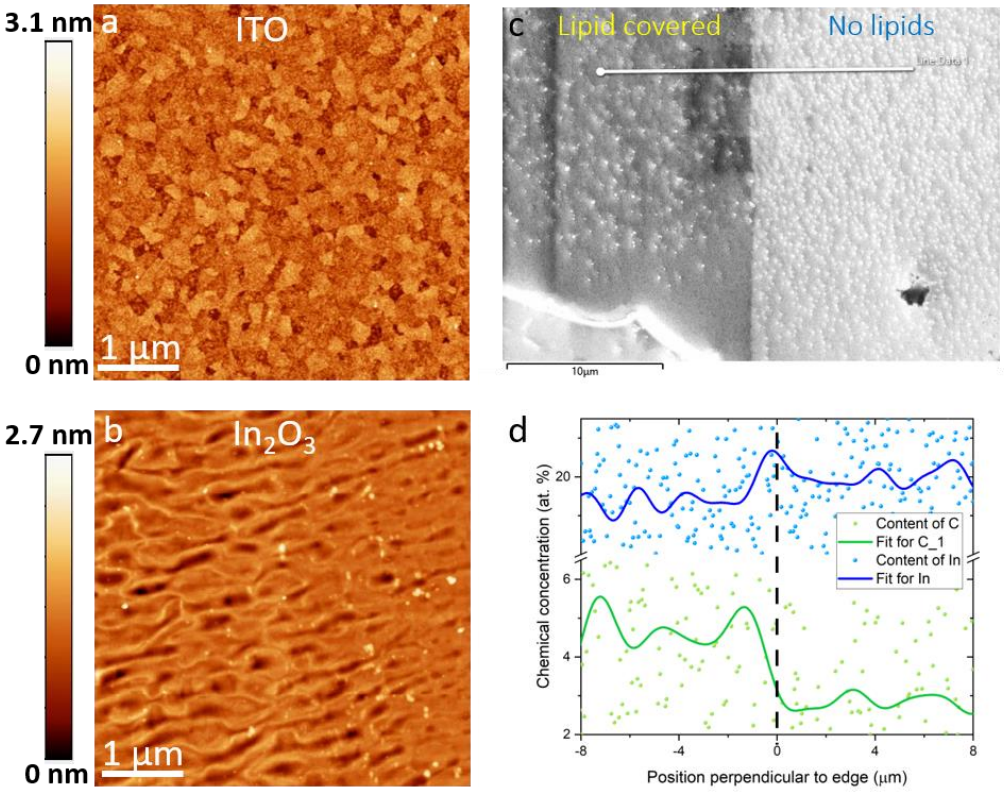

Figure 5.3 Surface morphologies of fabricated device.
a) *laser-ablated ITO thin film and b) inkjet-printed* In_2O_3 *annealed at 400°C. c) shows SEM images of surface topography of printed lipids on* In_2O_3*. d) shows the atomic per cent of the carbon and indium contents along the profile line as shown in c). Obtained signals were smoothed using a fast Fourier transform (FFT) filter.*

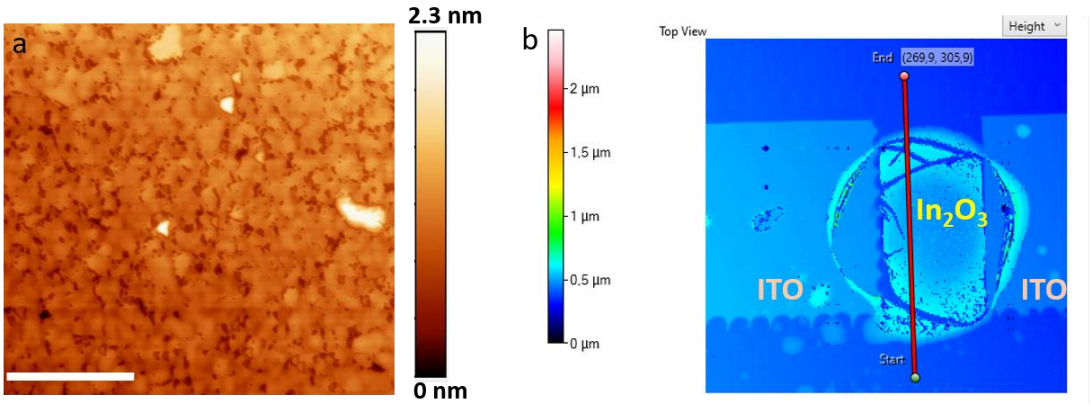

Figure 5.4 Morphology and optical profilometry of fabricated device.
a) Surface morphology of Gold contact. b) Optical Profilometry to investigate the thickness of In_2O_3 *layer printed with inkjet printing.*

5.3 Comparative Analysis of Device Performance Using Gold and ITO Contacts

IS is recognised as an effective method for the investigation of both internal and surface electrical properties in electrode systems, providing precise measurements of parameters associated with electrochemical reactions. When biomolecular interactions occur on modified surfaces, measurable alterations in surface properties can be detected through IS analysis.[196] In this study, IS was utilised to compare the performance of gold and indium tin oxide (ITO) as electrode materials for impedimetric biosensors. Gold, known for its excellent conductivity and biocompatibility, serves as a benchmark, while ITO offers the added benefit of transparency, advantageous for optical measurements when integrated with electrochemical detection.[197] Results derived from IS indicate that ITO exhibits greater sensitivity in detecting streptavidin binding.

At frequencies below 1 kHz, impedance is primarily governed by the leakage resistance of interdigitated electrodes (IDEs), a factor strongly dependent on the electrode material.[198] At frequencies exceeding 100 kHz, solution resistance begins to dominate the overall impedance, introducing greater measurement inaccuracies due to parasitic capacitances and inductances.[199,200] In the frequency range of 1 kHz to 100 kHz, the detection of affinity binding on IDEs is influenced by the electrode surface capacitance, which is attributed to interfacial and molecular polarisation effects.[201]

Consequently, most impedimetric biosensors operate within this frequency band, typically around 10 kHz, as it provides a stable signal and emphasises changes in interfacial impedance response.[202,203]

The leakage resistance (R_{leak}) was determined from the diameter of the semicircles in Nyquist plots, particularly in the high- and mid-frequency regions. By comparing

these values for devices functionalised with a lipid layer (+lipid), subsequently incubated with bovine serum albumin (BSA) to block nonspecific adhesion (+BSA), and then exposed to streptavidin for sensing (+streptavidin), the basic functionality of the biosensor devices was confirmed (**Table 5**).

Table 5. Complex non-linear fitting (CNLS) results of the ITO and Gold contacted In_2O_3 channels under different sample conditions (+lipid: after functionalisation of the channel with lipids; +BSA: after subsequent BSA incubation; and +streptavidin: after subsequent incubation).

CNLS fitting	R_s [Ohm]	R_{leak} [Ohm]	Q_{surf}	α
ITO + lipid	4028	$1.48 \cdot 10^{6}$	$1.97 \cdot 10^{-8}$	0.988
ITO + BSA	4059	21540	$3.17 \cdot 10^{-8}$	0.977
ITO + streptavidin	6 002	$6.71 \cdot 10^{6}$	$1.96 \cdot 10^{-8}$	0.987
Au + lipid	227.3	235622	$7.97 \cdot 10^{-8}$	0.927
Au + BSA	168.9	57117	$9.61 \cdot 10^{-8}$	0.838
Au + streptavidin	412.7	348 757	$7.49 \cdot 10^{-8}$	0.892

After the patterning of phospholipids onto the surface of indium oxide (In_2O_3), electrochemical impedance spectroscopy (EIS) revealed leakage resistance in the megaohm (MΩ) range for devices with ITO contacts and in the kilo-ohm (kΩ)

range for those with gold contacts, consistent with previously published reports.[17,204] Upon incubation with BSA, a sharp decline in resistance—in the kΩ range for both types of contacts—was observed. Following the incubation of streptavidin, the resistance increased once again, reaching the MΩ range for ITO-contacted devices and the kΩ range for those with gold contacts.

To understand this behaviour more thoroughly, the impedimetric biosensor was modelled using an equivalent circuit consisting of a constant phase element (CPE) and resistors as illustrated in **Figures 5.5a and 5.5b**.[199] The series resistance (R_s) represents a small resistance primarily attributed to ion drift within the solution bulk in response to an applied voltage. R_{leak} corresponds to a high impedance in parallel with the surface capacitance, which can be approximated as an ideal capacitor, though it is more accurately modelled using a constant phase element (Q_{surf}). The impedance of the CPE is expressed as $Z_{CPE} = 1/Q_{surf}(j\omega)\alpha$, where Q_{surf} represents a series combination of the surface modulation capacitance and the electric double-layer capacitance within the biosensor. This arises due to the dielectric layer formed by the bio-recognition element solution on the conductive gold or ITO electrodes. Notably, the CPE reflects capacitance dispersion within a heterogeneous interface, and for α approaching 1, the electric double layer is considered homogeneous. It is worth noting that the substrate type influences the homogeneity of biotin-PE patterning, likely affecting the electrostatically driven organisation of the phospholipid membrane, with ITO being identified as the preferential substrate.

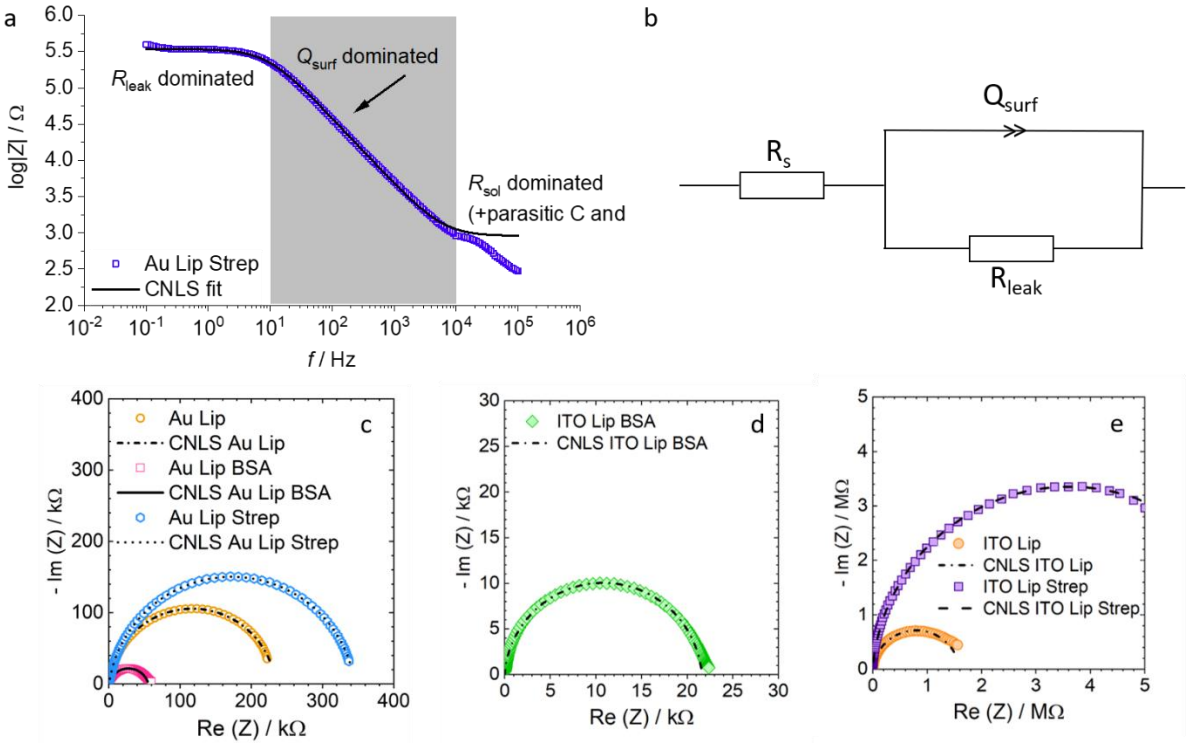

Figure 5.5 Complex plot representations of ITO-In_2O_3 and Gold-In_2O_3 devices.
a) Magnitude plot for a typical biosensor through one of the impedances measured on the Au/In_2O_3/lipid/streptavidin system. b) The equivalent circuit used for CNLS fitting. c) Complex plane representation of the measured impedance spectra on the gold biosensor and the corresponding fit results. d) and e) Complex plane representations of the measured impedance spectra on the ITO biosensor and the corresponding fit results. The concentration of streptavidin used was 0.01mg/ml in both devices.

To validate the accuracy of the proposed equivalent circuit, a differential relaxation time (DRT) analysis was performed to elucidate the presence of multiple time constants, thereby determining the occurrence of diffusion processes within our devices. DRT facilitates the conversion from the frequency domain to the time domain and, while it is predominantly utilised in battery analysis, I applied it to validate the accuracy of the equivalent circuit model. The devices showed a single peak, indicating that a single time constant suggests no diffusion occurring at the surface. The identification of a single time constant in the DRT analysis (see **Figure 5.6**) corroborated the correctness of the equivalent circuit model, pointing to the absence of diffusion-related processes within the system.

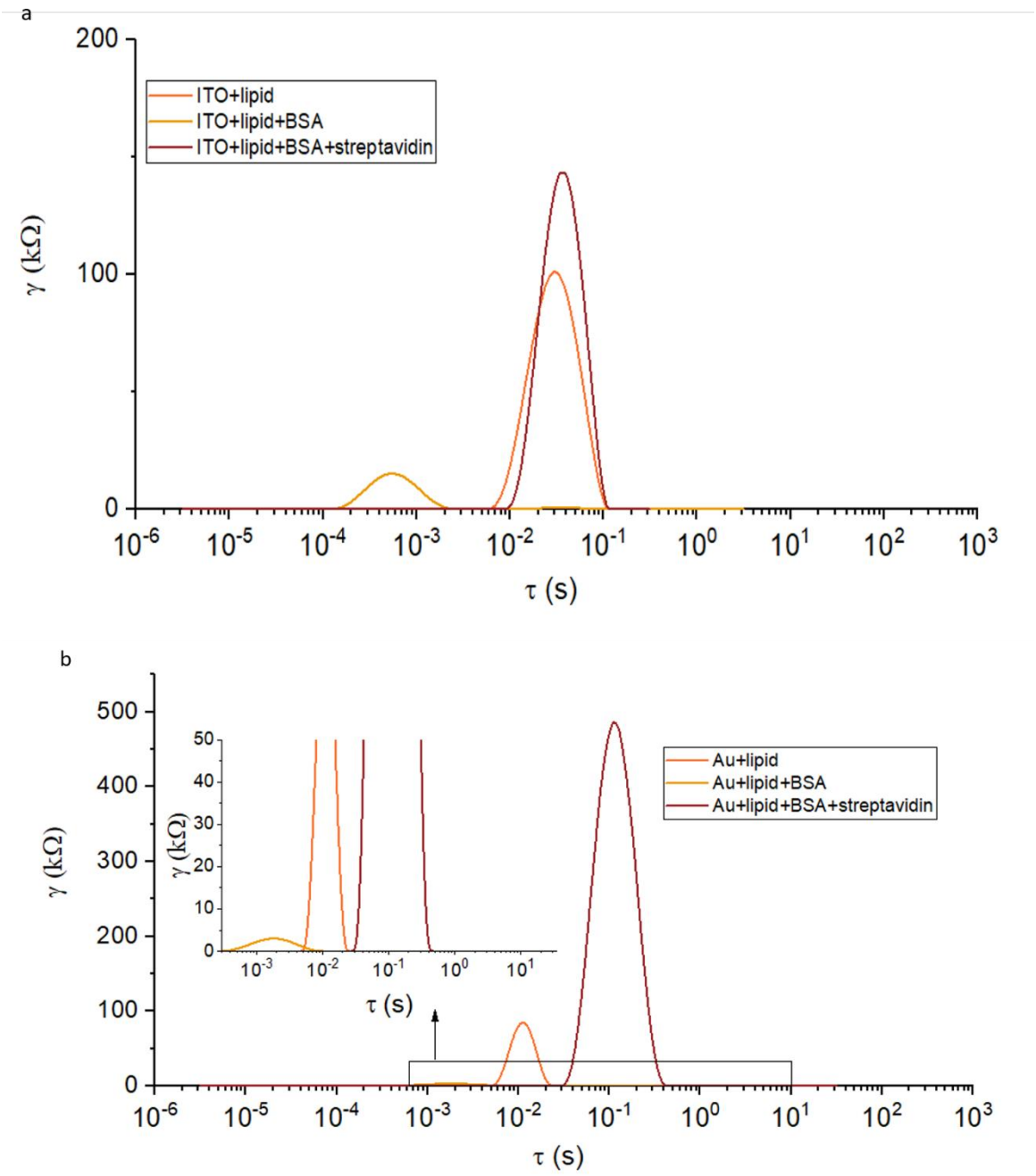

Figure 5.6 DRT analysis of *a) ITO-In_2O_3 devices and b) Gold-In_2O_3 devices.*

The reduction in impedance following the addition of BSA (**Figure 5.7**) can generally be attributed to conformational changes within the BSA molecules and electrostatic interactions. A further plausible explanation for the observed decrease in impedance due to BSA blocking is related to the charges on the BSA macromolecules. At pH 7.4, BSA possesses 17 net negative charges, which may create new conductive pathways or enhance pre-existing ones on the In_2O_3 surface

by binding to uncovered lipid areas and, to some extent, adhering to the lipid layer itself. Another contributing mechanism could be the additional passivation of the semi-conducting surface by BSA, leading to a further reduction in impedance.[205] Additionally, the adsorption of BSA onto the surface may induce conformational changes in the protein structure, potentially increasing the density and reorientation of BSA molecules, resulting in more compact layers that facilitate electron transfer, thus lowering impedance.[206]

To definitively confirm that the observed impedance changes are directly attributable to the interaction between BSA and the In_2O_3 channel material rather than to the ITO electrodes or other contact materials such as gold, a series of control experiments were performed. These controls included devices both with and without the In_2O_3 channel material as well as devices with and without lipid layers.

Figure 5.7 presents six subplots comparing three electrical properties (R_s, R_{leak}, and Q_{surf}) for both gold (Au) and indium tin oxide (ITO) contacts under various sample conditions (Lip, Lip BSA, and Lip Strep). A key similarity between the gold and ITO contacts is the observed reduction in both R_s and R_{leak} after BSA binding, followed by a significant increase in these parameters after streptavidin binding. Although this recovery of resistance may initially seem counterintuitive, it is likely driven by the highly specific and competitive binding interaction between streptavidin and biotinylated lipids.[207] Streptavidin's stronger binding affinity displaces the loosely bound BSA on the lipid film, thereby modulating the electrical properties of the system. This interpretation is supported by changes in Q_{surf}, which reflect a higher packing density and increased homogeneity in the ITO + streptavidin layer.[208] Only at higher concentrations of streptavidin does the resistance decrease again, as the nearly neutral streptavidin[209] begins to modulate the In_2O_3 channel.

When comparing the performance of devices with gold and ITO electrodes, it is evident that the contact resistance is likely higher for ITO overall (even when comparing Au + lipid and ITO + lipid resistances). However, the sensor capabilities are superior with ITO contacts, as they exhibit greater sensitivity to streptavidin addition as evidenced in **Table 5** and **Figure 5.7**. The sensitivity (in terms of changes in surface capacitance and resistance) of the ITO system is higher by an order of magnitude.

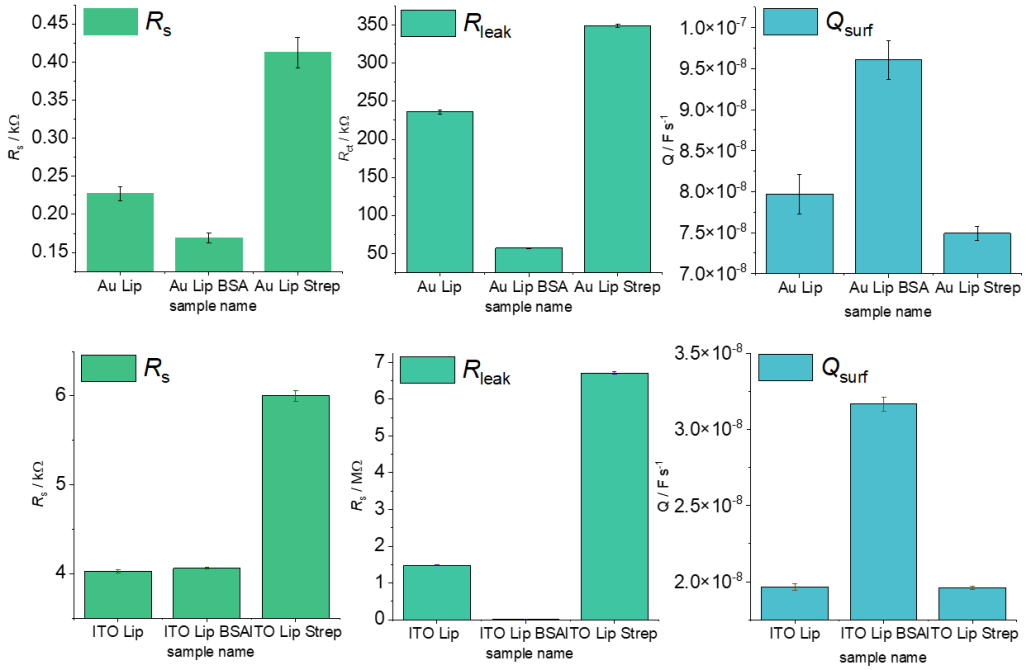

Figure 5.7 The results of the CNLS fitting with the corresponding standard errors.
a) b) and c) CNLS fitting results of devices with gold contacts. d) e) and f) The CNLS fitting results of devices with ITO contacts. The streptavidin concentration was 0.01 mg/ml for both Au as well as ITO devices.

5.4 Control Experiments for Understanding Device Functionality

To elucidate the functionality of the sensor, it was critical to investigate the device's behaviour in the presence and absence of indium oxide, BSA, and lipids. A series of control experiments were conducted, examining the Nyquist plots across varying device compositions to explore the interactions between these components. Two

sets of experiments were performed on four different devices, each prepared under identical conditions, except for the presence (**Figure 5.8b**) or absence (**Figure 5.8a**) of BSA across different concentrations of streptavidin. The results indicated that BSA blocking significantly improved the signal-to-noise ratio, facilitating a clearer differentiation of streptavidin concentrations (**Figure 5.4.1**). Thus, it can be concluded that BSA blocking is essential for all devices to enhance the precision and clarity of signal detection, allowing for more effective concentration differentiation.

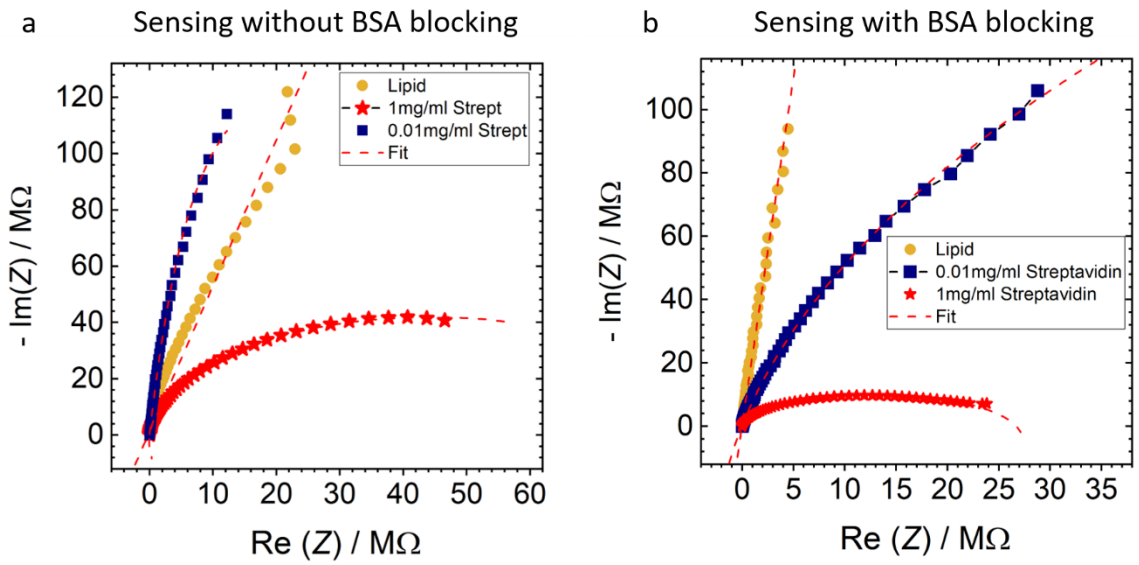

Figure 5.8 Comparison of complex plane representations of *a) devices without BSA blocking and b) devices with BSA blocking.*

The subsequent set of experiments aimed to determine the role of the channel material, indium oxide, in the detection process. To this end, experiments were conducted in the absence of the indium oxide channel material to assess its necessity (**Figure 5.9b**). Additionally, it was essential to evaluate whether the lipids patterned via DPN were integral to the detection mechanism. Consequently, experiments were performed to detect streptavidin with and without lipid layers on devices lacking the indium oxide channel material.

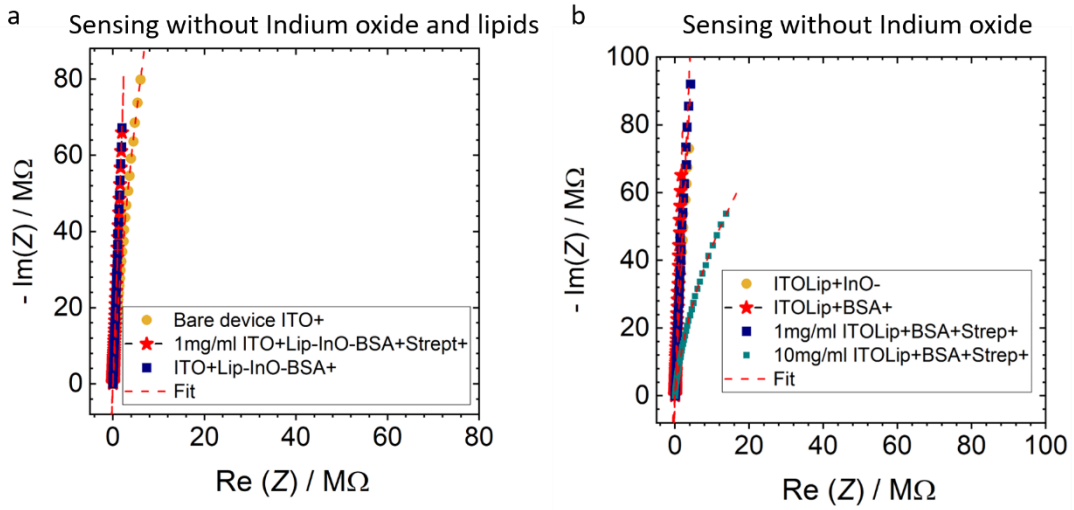

Figure 5.9 Comparison of complex plane representations of *a) devices without indium oxide and lipids and b) devices without indium oxide but with the presence of lipids printed with DPN.*

The results demonstrated that indium oxide plays a critical role in facilitating streptavidin detection (**Figure 5.9**). Moreover, BSA, when incubated on devices without lipids, exhibited an unusual inductive behaviour at low frequencies (**Figure 5.10a**). While the precise mechanism underlying this phenomenon remains unclear, it is noteworthy that biomolecular interactions behave differently in the absence of lipid layers. It is hypothesised that BSA molecules may bind to residual lipid patches where biotin is absent, potentially contributing to the sensor's enhanced specificity.

The experimental data further confirmed that the detection of low streptavidin concentrations becomes highly challenging without the simultaneous presence of both lipids and the indium oxide channel material. This suggests that the synergistic interaction between these components is crucial for optimal sensor performance. **Figures 5.9** and **5.10** illustrate the difficulty of detecting streptavidin at low concentrations in the absence of lipids and the channel material, reinforcing their indispensable roles in the device's functionality.

The results, therefore, unequivocally demonstrate that the impedance variations are specifically linked to the interaction between BSA and In_2O_3. These

experiments highlighted the significance of the In_2O_3 channel as a transducer, enabling the detection of a clear signal from streptavidin binding, even on a relatively small area, whereas lipid writing on a single electrode had no significant effect on device characteristics. This is likely due to the low proportion of the electrode area covered by lipids relative to the total electrode area under the liquid. Furthermore, these findings underscore the critical role of In_2O_3 as a channel material, enhancing both the signal response and the sensitivity, thereby improving the ability to distinguish between different concentrations.

a

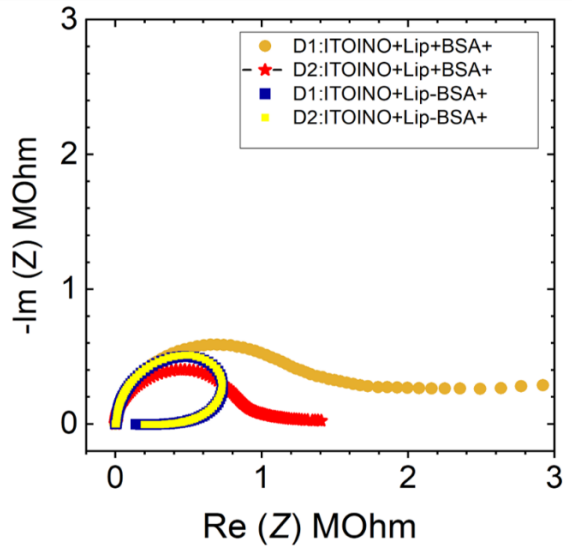

b

Sample name	What does it mean?
Lip+	With lipid functionalisation
Lip-	Without lipid functionalisation
INO+	Contains indium oxide
INO-	Does not contain indium oxide

Figure 5.10 Complex plane representations of different devices with BSA and without the presence of phospholipids.
a) *Devices with BSA with and without lipids b) Table showing various abbreviations of the devices shown in Figure 5.9 and Figure 5.10.*

5.5 Analytical Performance and Sensitivity of ITO-In_2O_3 Biosensor

The analytical performance of the EIS sensor for streptavidin detection was thoroughly assessed over a broad concentration range, spanning from 1 µg/ml to 500 mg/ml. Given the importance of the Nyquist plot in revealing the electrical characteristics of the biosensor and the electrochemical interactions at the

electrode-electrolyte interface, the complex impedance responses at varying streptavidin concentrations were analysed to gain insights into the detection mechanism. The resulting data is illustrated in **Figure 5.11a.** The sensor demonstrated a robust and sensitive response to varying concentrations of streptavidin across five orders of magnitude, reflected in significant changes in R_{leak}. IS revealed that R_{leak} increased at lower streptavidin concentrations compared to the BSA-blocked device. This effect is likely due to the replacement of highly charged BSA molecules loosely bound to the lipid membrane by streptavidin, which reduced the impedance. Conversely, at higher streptavidin concentrations, a marked decrease in R_{leak} was observed, correlating with the increased binding of streptavidin and enhanced electron transfer within the system.

The comparison of circuit elements across different streptavidin concentrations, presented in **Table 6,** provides further insight into the sensor's electrical behaviour.

The usable concentration window between the maximum and minimum signal response defines the dynamic range of the sensor (**Figure 5.11b**). This range was calculated from the detection limit to the saturation level of the biosensor signal. It is crucial to recognise that the linear detection range is inherently a trade-off against sensitivity.

A higher sensitivity typically results in a smaller detection range, as the saturation level is reached at a lower target concentration. This phenomenon is evident in the present study, where the sensor exhibited a linear dynamic range between 0.01 and 0.2 $mg \cdot ml^{-1}$ streptavidin concentration. While the performance of the present sensor in regard to streptavidin might be limited, in future developments, where the bound streptavidin will be used for attaching of antibodies as specific recognition elements for diagnostically relevant proteins, the linear range could be larger as of the lower affinity of such analytes compared to streptavidin. From a

fit to the linear range (**Figure 5.12**) a LOD of 5.78 x 10^{-3} mg/ml is derived and a high sensitivity (144 MΩ/(mg/mL)) promises accurate analysis at small sample quantities and trace analyte concentrations. Furthermore, controlled pre-dilution of the analyte can shift the analyte concentration to allow measurements of the relevant diagnostic range in the linear range of the device.

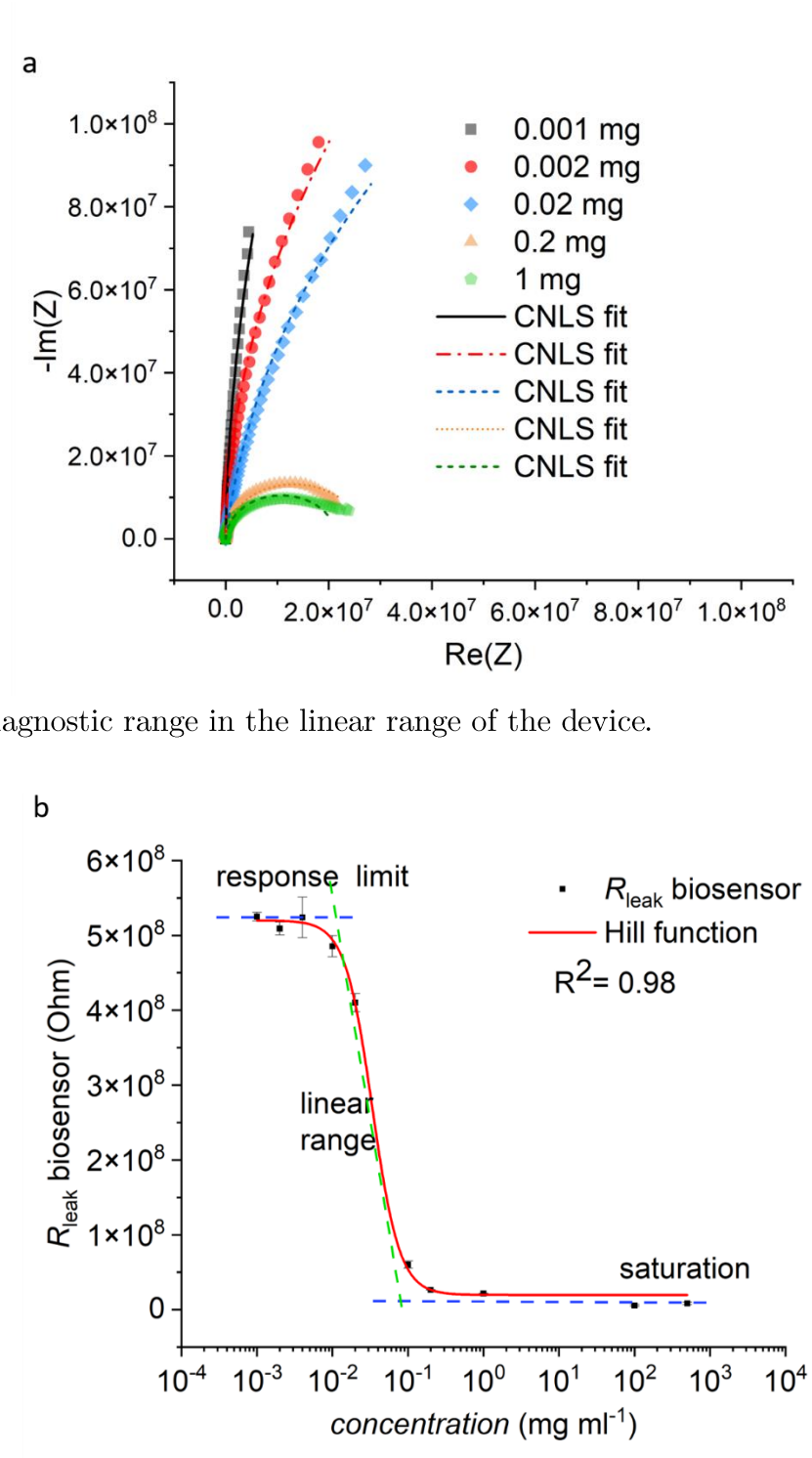

Figure 5.11 Analytical performance of the biosensor

a) Complex plane diagrams of different concentrations of streptavidin. b) Change in log concentration vs R_{leak} of the ITO-In_2O_3 devices.

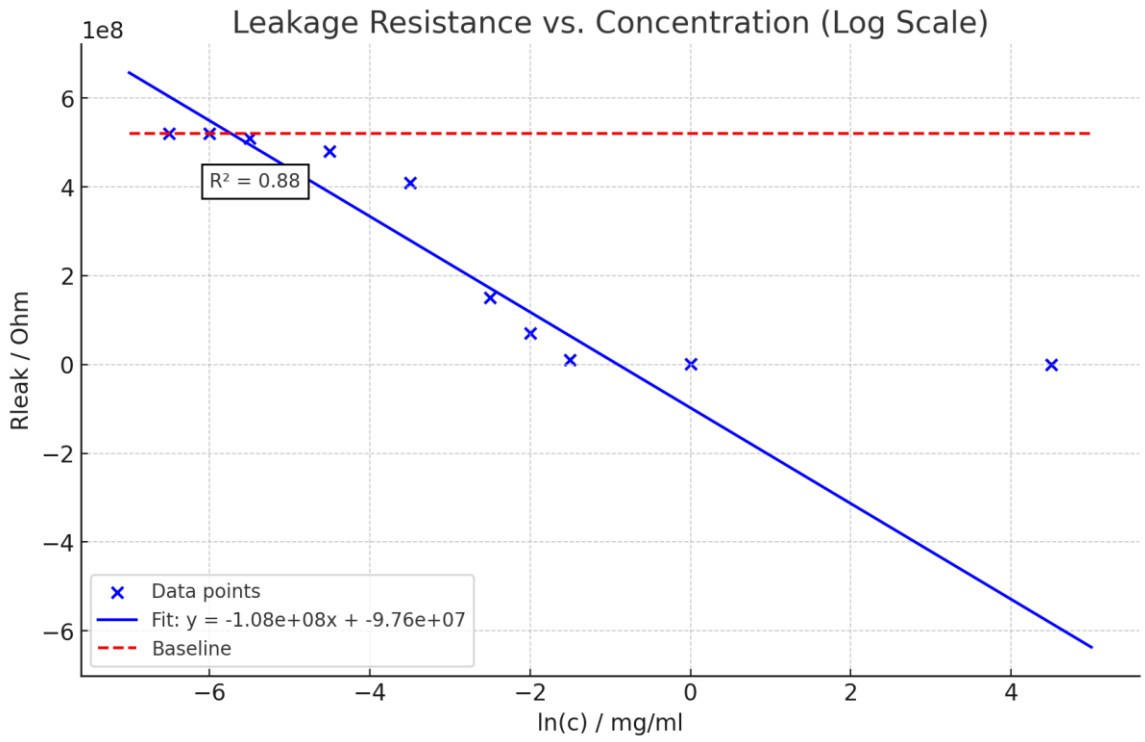

Figure 5.12 Calculation of the LOD.
For the quantification of the LOD, a linear fit (blue line) was applied to the linear range of the sensor device (0.004 to 0.2 mg/ml streptavidin). The dashed red line marks the response limit of the device (5.25 x 10^8 Ohm). The intersection of these two lines gives the LOD concentration to 0.006 mg/ml. The sensitivity of the sensor is given by the slope of the linear range to 144 MΩ/(mg/ml).

The sensor's specificity was rigorously tested using a non-target protein, the SARS-CoV-2 Spike His protein (**Figure 5.13**); no significant response was detected, confirming the high selectivity of the system towards streptavidin. The overall findings underscore the sensor's remarkable performance, exhibiting high sensitivity, selectivity, and stability, with a well-defined dynamic range tailored for streptavidin detection.

Table 6. Values of various circuit elements of the ITO-In_2O_3 devices for different concentrations of streptavidin.

Concentration mg/ml	**Rs** Ohm	**Qsurf** F x $s^{(a-1)}$	**Alpha**	**R_{leak}** Ohm	**Chi^2/|Z|^2**
500	2325.69	2.76 x 10^{-8}	0.95	8,44 x 10^{6}	9.07
100	2306.45	3.28 x 10^{-8}	0.96	5,65 x 10^{6}	7.02
1	3.34 x 10^{3}	1.85 x 10^{-8}	0.97	2,17 x 10^{7}	0.28
0.2	3.79 x 10^{3}	2.18 x 10^{-8}	0.99	2,66 x 10^{7}	0.12
0.1	4076.58	1.88 x 10^{-8}	0.98	6,02 x 10^{7}	0.87
0.04	2767.51	1.55 x 10^{-8}	0.98	5,24 x 10^{8}	0.21
0.02	3817.44	1.64 x 10^{-8}	0.93	4,10 x 10^{8}	0.06
0.01	3836.76	1.26 x 10^{-8}	0.96	4,85 x 10^{8}	0.10
0.002	4034.89	1.58 x 10^{-8}	0.99	5.09 x 10^{8}	0.08

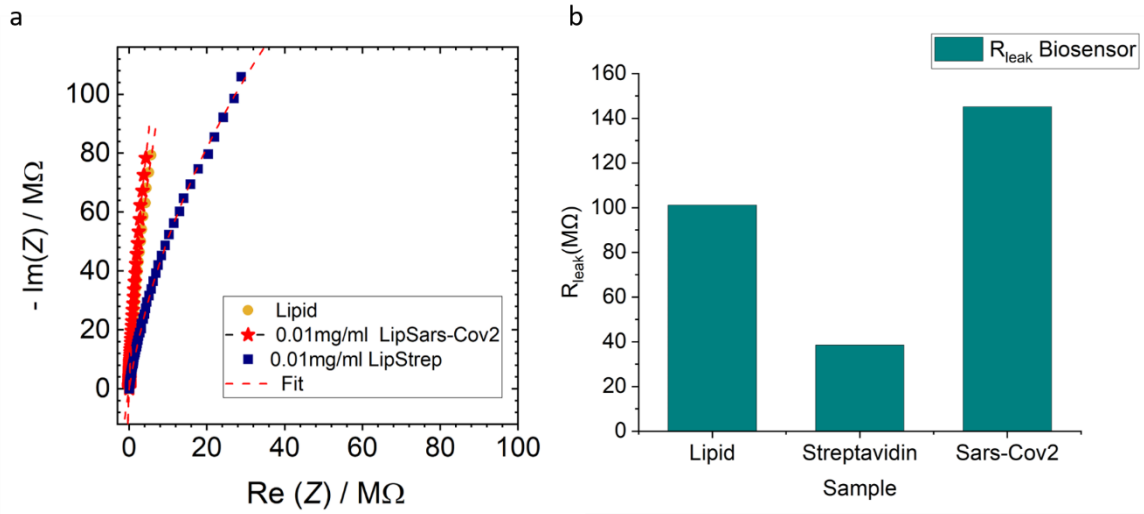

Figure 5.13. Specificity of the sensor.
a) Complex plot representation of ITO-In_2O_3 devices (printed with biotin-DOPC) with streptavidin and Sars-Cov-2 protein.b) Graph showing the change in R_{leak} resistance after the addition of streptavidin and Sars-Cov-2 protein.

5.6 Discussion

This study demonstrates the successful fabrication, development and characterization of a hybrid In_2O_3/phospholipid membrane based electrochemical sensor for the selective and sensitive detection of proteins. Taking advantage of the unique properties of In_2O_3/phospholipid membrane hybrid structure as a transducer (offering inherent anti-fouling properties to avoid unwanted protein adhesion, but still offering specific binding sites) and employing inkjet printing and lipid dip-pen nanolithography for device fabrication, we have established a platform that holds significant potential for point-of-care diagnostic applications.

Our findings reveal that indium tin oxide (ITO) electrodes as contacts, when compared to gold electrode contacts, offer superior sensitivity up to one magnitude higher for the ITO based devices in detecting streptavidin through EIS. This enhanced sensitivity, combined with the scalability and cost-effectiveness of our fabrication methods, positions this biosensor as a promising candidate with potential for future development into a fully printable, multiplexed biosensor system. The comprehensive evaluation of the biosensor's performance across a wide concentration range (1 µg/ml to 1 mg/ml) underscores its robustness and reliability. The Hill function reveals that above the linear range, the sensor hits its detection limit (5.78×10^{-3} mg/ml) and reaches saturation above 1 mg/ml.

The demonstration of the device with streptavidin as model protein offers a straight-forward way for future developments, as the demonstrated biotinylated lipid membrane/streptavidin construct can itself be utilized for binding of further recognition elements as e.g. biotinylated antibodies in ordered fashion, which elevates activity by the directional binding, preventing of denaturation and enhanced lateral mobility. The existing library of biotinylated antibodies offer almost limitless options for highly specific targeting of antigens. This work not only

advances the field of electrochemical biosensing but also opens avenues for the development of sophisticated diagnostic tools capable of simultaneous multi-disease detection.

Chapter 6: Conclusions and Outlook

6.1 Conclusions

In conclusion, this thesis has elucidated the interaction of phospholipid with different materials relevant to biosensors and demonstrated the fabrication and characterization of a printed electrochemical biosensor that leverages a hybrid indium oxide/phospholipid membrane structure for protein detection. By combining the semiconducting properties of indium oxide and the biomimetic qualities of phospholipid membranes, this sensor platform offers a promising path forward for sensitive, selective, and scalable point-of-care diagnostics. Additionally, the exploration of amorphous nanoglass substrates provides insights into lipid interactions on non-crystalline materials, adding more understanding of lipid-surface interactions at the nanoscale.

The major contributions of this thesis are:

1) **Fabrication and Development of Hybrid Biosensor**: A hybrid indium oxide (In_2O_3)/phospholipid membrane electrochemical sensor was successfully developed and comprehensively characterized, exhibiting exceptional specificity and sensitivity for the selective detection of streptavidin. The device utilized inkjet printing and lipid dip-pen nanolithography, paving the way for scalable, high-sensitivity biosensing.

2) **Enhanced Sensitivity with ITO Electrodes**: It was demonstrated that ITO electrode contacts significantly improve sensor sensitivity, achieving up to an order of magnitude greater sensitivity than gold electrodes in detecting streptavidin through electrochemical impedance spectroscopy.

3) **Large Detection range**: Performance evaluation was conducted over a wide concentration range (**1 µg/ml to 1 mg/ml**), showing that the sensor remains

robust and reliable. The Hill function analysis indicates a sensitivity threshold near 10^{-3} mg/ml, with saturation above 10 mg/ml.

4) **Insights into Lipid Confinement on Nanoglass Substrates**: It was revealed that columnar nanoglass substrates, particularly those with amorphous interfaces, restrict lipid spreading, suggesting a mechanism of confinement attributable to nanostructural morphology rather than surface geometry alone.

5) **Potential for Applications**: The findings of the research imply that nanoglass surfaces may influence lipid membrane behaviour in a way relevant to cell interactions, offering potential applications in biomaterial design for biomedical research and therapeutic applications. Additionally, the CuZr nanoglasses have the potential to be used as electrodes for biosensor applications.

6.2 Outlook

The potential of oxide semiconductors, as solution-processible and printable FETs and is well established, yet their integration into biosensors remains underexplored. While most existing Bio-FETs rely on organic materials, metal oxide semiconductors present unique opportunities for enhancing sensitivity and selectivity in biosensing applications. Their interactions with biomolecules can yield more precise and responsive devices. Further research is essential to advance these devices towards practical, real-world diagnostic applications, particularly in human sample analysis. A few possible directions are listed here:

1) **Enhancement of Selectivity and Sensitivity**: Incorporating a reference electrode to monitor leak resistance changes could significantly improve sensor selectivity and expand the detection range. This approach could

enable detection limits in the pM and nM ranges, enhancing precision for low-concentration biomarkers.

2) **Application in Real-World Biological Samples**: Extensive studies using real biological fluids, such as blood and urine, are essential to confirm the device's efficacy and precision in real-time diagnostics for potential clinical applications.

3) **Exploration of additional Biomarkers for disease detection**: Expanding the scope of detectable biomarkers and evaluating their printability and stability on sensor platforms is crucial. Therefore, conducting simulation studies on the conduction mechanisms within oxide-based Bio-FETs will provide deeper insights into device operation.

4) **Integration of Nanoglass Materials for Sensing**: The novel nanoglass materials explored in this thesis show potential as electrode materials in electrochemical biosensors. Evaluating their performance with indium oxide channels could reveal new interactions and enhance device sensitivity even more.

5) **Development of Simulation Models**: Computational models to simulate metal oxide-biomolecule interactions, including device behaviour, would offer predictive insights. This could guide the optimization of sensor performance and facilitate rapid, iterative design improvements.

These future directions collectively aim to advance metal oxide-based Bio-FETs towards clinical-grade reliability and will open avenues for broad diagnostic applications.

List of Publications

1. Berganza, E., Apte, G., **Vasantham, S. K.,** Nguyen, T. -H., & Hirtz, M. Integration of Biofunctional Molecules into 3D-Printed Polymeric Micro-/Nanostructures. Polymers, 14(7), 1327. (**2022**). https://doi.org/10.3390/polym14071327

2. Berganza, E.; Ebrahimkutty, M.P.,**Vasantham, S.K.,**Zhong, C.,Wunsch, A., Navarrete, A., Galic, M.,Hirtz, M. A multiplexed phospholipid membrane platform for curvature sensitive protein screening. Nanoscale **2021**, 13, 12642–12650. DOI: 10.1039/D1NR01133B

3. M.K. Saghafi, **S.K. Vasantham**, N.Hussain, G.Mathew, F.Colombo, B.Schamberger, E.Pohl, G.C. Marques, B.Breitung, M.Tanaka, M. Bastmeyer, C.Selhuber-Unkel, U.Schepers, M.Hirtz, J.A.Hagmann. Printed Electronic Devices and Systems for Interfacing with Single Cells up to Organoids Advanced Functional Materials 34 (20), 2308613, (**2024**), https://doi.org/10.1002/adfm.202308613

4. S K Vasantham, E. Boltynjuk, E.B. Eguiarte, S.H. Nandam, H. Hahn, M. Hirtz. Nanoscale Confinement of Dip-Pen Nanolithography Written Phospholipid Structures on CuZr Nanoglasses,Advanced Materials Interfaces 11 (2), 2300721, **(2024)**, https://doi.org/10.1002/admi.202300721

5. R. Kumar, S. Llewellyn, **S. K. Vasantham**, Kaiwen Nie, S. Sekula-Neuner, A. Vijayaraghavan & M. Hirtz. Protein spot arrays on graphene oxide coatings for efficient single-cell capture. Sci Rep 12, 3895 (**2022**), https://doi.org/10.1038/s41598-022-06225-4

6. **S. K. Vasantham**, G.Matthew, N.Hussain, S.A. Singaraju, E.Boltynjuk, J.Ryl, M. Hirtz, Aghassi-Hagmann. Low Volume Lipid Membrane Based Impedimetric Sensor for Protein Detection Small, (**2024**). (Under review)

Conference presentation

1. Nanoscale Confinement of Dip-Pen Nanolithography Written Phospholipid Structures on CuZr Nanoglasses, MRS spring, Seattle, USA, **2024**.

References

[1] R. A. Picca, K. Manoli, E. Macchia, L. Sarcina, C. Di Franco, N. Cioffi, D. Blasi, R. Österbacka, F. Torricelli, G. Scamarcio, L. Torsi, *Adv. Funct. Mater.* **2020**, *30*, 1904513.

[2] F. Torricelli, D. Z. Adrahtas, Z. Bao, M. Berggren, F. Biscarini, A. Bonfiglio, C. A. Bortolotti, C. D. Frisbie, E. Macchia, G. G. Malliaras, I. McCulloch, M. Moser, T.-Q. Nguyen, R. M. Owens, A. Salleo, A. Spanu, L. Torsi, *Nat. Rev. Methods Primer* **2021**, *1*, 1.

[3] P. Seshadri, K. Manoli, N. Schneiderhan-Marra, U. Anthes, P. Wierzchowiec, K. Bonrad, C. Di Franco, L. Torsi, *Biosens. Bioelectron.* **2018**, *104*, 113.

[4] J. Rivnay, S. Inal, A. Salleo, R. M. Owens, M. Berggren, G. G. Malliaras, *Nat. Rev. Mater.* **2018**, *3*, 1.

[5] M. T. Hwang, M. Heiranian, Y. Kim, S. You, J. Leem, A. Taqieddin, V. Faramarzi, Y. Jing, I. Park, A. M. van der Zande, S. Nam, N. R. Aluru, R. Bashir, *Nat. Commun.* **2020**, *11*, 1543.

[6] Q. Liu, C. Zhao, M. Chen, Y. Liu, Z. Zhao, F. Wu, Z. Li, P. S. Weiss, A. M. Andrews, C. Zhou, *iScience* **2020**, *23*, 101469.

[7] J. Kim, Y. S. Rim, H. Chen, H. H. Cao, N. Nakatsuka, H. L. Hinton, C. Zhao, A. M. Andrews, Y. Yang, P. S. Weiss, *ACS Nano* **2015**, *9*, 4572.

[8] Y. S. Rim, S.-H. Bae, H. Chen, J. L. Yang, J. Kim, A. M. Andrews, P. S. Weiss, Y. Yang, H.-R. Tseng, *ACS Nano* **2015**, *9*, 12174.

[9] K. M. Cheung, K.-A. Yang, N. Nakatsuka, C. Zhao, M. Ye, M. E. Jung, H. Yang, P. S. Weiss, M. N. Stojanović, A. M. Andrews, *ACS Sens.* **2019**, *4*, 3308.

[10] I. Bontidean, C. Berggren, G. Johansson, E. Csöregi, B. Mattiasson, J. R. Lloyd, K. J. Jakeman, N. L. Brown, *Anal. Chem.* **1998**, *70*, 4162.

[11] F. Yin, *Anal. Lett.* **2004**, *37*, 1269.

[12] L. F. E. Huerta-Nuñez, G. Gutierrez-Iglesias, A. Martinez-Cuazitl, M. M. Mata-Miranda, V. D. Alvarez-Jiménez, V. Sánchez-Monroy, A. Golberg, C. A. González-Díaz, *Sci. Rep.* **2019**, *9*, 6419.

[13] H. Wang, N. Sobahi, A. Han, *Lab. Chip* **2017**, *17*, 1264.

[14] L. L. Crowell, J. S. Yakisich, B. Aufderheide, T. N. G. Adams, *Micromachines* **2020**, *11*, 832.

[15] O. Purrucker, H. Hillebrandt, K. Adlkofer, M. Tanaka, *Electrochimica Acta* **2001**, *47*, 791.

[16] Z. Lu, D. van Niekerk, A. Savva, K. Kallitsis, Q. Thiburce, A. Salleo, A.-M. Pappa, R. M. Owens, *J. Mater. Chem. C* **2022**, *10*, 8050.

[17] H. Hillebrandt, G. Wiegand, M. Tanaka, E. Sackmann, *Langmuir* **1999**, *15*, 8451.
[18] M. H. Shamsi, H.-B. Kraatz, in *Handb. Nanoelectrochemistry Electrochem. Synth. Methods Prop. Charact. Tech.* (Eds: M. Aliofkhazraei, A.S.H. Makhlouf), Springer International Publishing, Cham, **2016**, pp. 1073–1094.
[19] Y. Hirata, S. Yabuki, F. Mizutani, *Bioelectrochemistry* **2004**, *63*, 217.
[20] M. V. Mirkin, B. R. Horrocks, *Anal. Chim. Acta* **2000**, *406*, 119.
[21] Y. He, S. L. Dreyer, T. Akçay, T. Diemant, R. Mönig, Y. Ma, Y. Tang, H. Wang, J. Lin, S. Schweidler, M. Fichtner, H. Hahn, T. Brezesinski, B. Breitung, Y. Ma, *ACS Nano* **2024**, *18*, 24441.
[22] K. Jüttner, *Electrochimica Acta* **1990**, *35*, 1501.
[23] S. Asghari, A. Mokmeli, M. Samavati, *Int. J. Hydrog. Energy* **2010**, *35*, 9283.
[24] J. Bausells, H. Ben Halima, F. G. Bellagambi, A. Alcacer, N. Pfeiffer, M. Hangouët, N. Zine, A. Errachid, *Electrochem. Sci. Adv.* **2022**, *2*, e2100138.
[25] A. Chakraborty, P. Dutta, A. Wakankar, C. RoyChaudhuri, *Biosens. Bioelectron. X* **2022**, *12*, 100253.
[26] A. Susloparova, D. Koppenhöfer, X. T. Vu, M. Weil, S. Ingebrandt, *Biosens. Bioelectron.* **2013**, *40*, 50.
[27] T. Wadhera, D. Kakkar, G. Wadhwa, B. Raj, *J. Electron. Mater.* **2019**, *48*, 7635.
[28] D. Sadighbayan, M. Hasanzadeh, E. Ghafar-Zadeh, *TrAC Trends Anal. Chem.* **2020**, *133*, 116067.
[29] J. Kim, J. Jeong, S. H. Ko, *Bio-Des. Manuf.* **2024**, *7*, 548.
[30] X. Ye, T. Jiang, Y. Ma, D. To, S. Wang, J. Chen, *Biosens. Bioelectron. X* **2023**, *13*, 100301.
[31] L. C. T. Shoute, G. N. Abdelrasoul, Y. Ma, P. A. Duarte, C. Edwards, R. Zhuo, J. Zeng, Y. Feng, C. L. Charlton, J. N. Kanji, S. Babiuk, J. Chen, *Microsyst. Nanoeng.* **2023**, *9*, 1.
[32] D. Zhang, Y. Lu, Q. Zhang, L. Liu, S. Li, Y. Yao, J. Jiang, G. L. Liu, Q. Liu, *Sens. Actuators B Chem.* **2016**, *222*, 994.
[33] D. Grieshaber, R. MacKenzie, J. Vörös, E. Reimhult, *Sensors* **2008**, *8*, 1400.
[34] J. Hölzl, F. K. Schulte, *Springer Tracts Mod. Phys.* **1979**, *85*, 1.
[35] A. Way, J. Luke, A. D. Evans, Z. Li, J.-S. Kim, J. R. Durrant, H. K. Hin Lee, W. C. Tsoi, *AIP Adv.* **2019**, *9*, 085220.
[36] Y. S. Rim, H. Chen, B. Zhu, S.-H. Bae, S. Zhu, P. J. Li, I. C. Wang, Y. Yang, *Adv. Mater. Interfaces* **2017**, *4*, 1700020.
[37] N. Aroonyadet, X. Wang, Y. Song, H. Chen, R. J. Cote, M. E. Thompson, R. H. Datar, C. Zhou, *Nano Lett.* **2015**, *15*, 1943.

[38] Q. Liu, Y. Liu, F. Wu, X. Cao, Z. Li, M. Alharbi, A. N. Abbas, M. R. Amer, C. Zhou, *ACS Nano* **2018**, *12*, 1170.

[39] X. Feng, A. Scholz, M. B. Tahoori, J. Aghassi-Hagmann, *IEEE Trans. Electron Devices* **2020**, *67*, 4918.

[40] M. Hirtz, A. Oikonomou, T. Georgiou, H. Fuchs, A. Vijayaraghavan, *Nat. Commun.* **2013**, *4*, 2591.

[41] J. S. Daniels, N. Pourmand, *Electroanalysis* **2007**, *19*, 1239.

[42] V. Tsouti, C. Boutopoulos, I. Zergioti, S. Chatzandroulis, *Biosens. Bioelectron.* **2011**, *27*, 1.

[43] D. D. Macdonald, *Electrochimica Acta* **2006**, *51*, 1376.

[44] J. Kieninger, *Electrochemical Methods for the Micro- and Nanoscale: Theoretical Essentials, Instrumentation and Methods for Applications in MEMS and Nanotechnology*, De Gruyter Oldenbourg, **2022**.

[45] "ZView Software | Download Latest Version | AMETEK SI," can be found under https://www.ameteksi.com/products/software/zview-software-en,

[46] "ZSimpWin Software | Download Latest Version | AMETEK SI," can be found under https://www.ameteksi.com/products/software/zsimpwin,

[47] M. E. Orazem, P. Agarwal, L. H. Garcia-Rubio, *J. Electroanal. Chem.* **1994**, *378*, 51.

[48] H. Helmholtz, *Ann. Phys.* **1853**, *165*, 211.

[49] V. S. Bagotsky, *Fundamentals of Electrochemistry*, John Wiley & Sons, **2005**.

[50] D. Meena, R. Kumar, S. Gupta, O. Khan, D. Gupta, M. Singh, *J. Energy Storage* **2023**, *72*, 109323.

[51] "Electrochemical Methods: Fundamentals and Applications, 2nd Edition | Wiley," can be found under https://www.wiley.com/en-kr/Electrochemical+Methods%3A+Fundamentals+and+Applications%2C+2nd+Edition-p-9780471043720,

[52] L. L. Zhang, X. S. Zhao, *Chem. Soc. Rev.* **2009**, *38*, 2520.

[53] S. M. Gateman, O. Gharbi, H. Gomes de Melo, K. Ngo, M. Turmine, V. Vivier, *Curr. Opin. Electrochem.* **2022**, *36*, 101133.

[54] A. Yavarinasab, S. Janfaza, N. Tasnim, H. Tahmooressi, A. Dalili, M. Hoorfar, *Anal. Chim. Acta* **2020**, *1109*, 27.

[55] EC lab manual, can be found under https://mmrc.caltech.edu/BioLogic%20Echem/ECLab%20Manuals/EC-Lab%20software%20Techniques%20and%20Applications%20manual.pdf,

[56] "OriginLab - Origin and OriginPro - Data Analysis and Graphing Software," can be found under https://www.originlab.com/,

[57] M. Braus, *Zur Theorie der Elektrolyte. I. Gefrierpunktserniedrigung und verwandte Erscheinungen* **2019**.
[58] V. Kesler, B. Murmann, H. T. Soh, *ACS Nano* **2020**, *14*, 16194.
[59] R. F. Taylor, I. G. Marenchic, R. H. Spencer, *Anal. Chim. Acta* **1991**, *249*, 67.
[60] A. Erdem, E. Eksin, M. Muti, *Colloids Surf. B Biointerfaces* **2014**, *115*, 205.
[61] H. Qi, L. Shangguan, C. Li, X. Li, Q. Gao, C. Zhang, *Biosens. Bioelectron.* **2013**, *39*, 324.
[62] D. T. Tran, V. Vermeeren, L. Grieten, S. Wenmackers, P. Wagner, J. Pollet, K. P. F. Janssen, L. Michiels, J. Lammertyn, *Biosens. Bioelectron.* **2011**, *26*, 2987.
[63] G. Bacher, S. Pal, L. Kanungo, S. Bhand, *Sens. Actuators B Chem.* **2012**, *168*, 223.
[64] M. Xu, X. Luo, J. J. Davis, *Biosens. Bioelectron.* **2013**, *39*, 21.
[65] E. B. Aydın, M. Aydın, M. K. Sezgintürk, *Sens. Actuators B Chem.* **2021**, *345*, 130355.
[66] D. Soto, J. Orozco, *Anal. Chim. Acta* **2022**, *1205*, 339739.
[67] S. Vasantham, R. Alhans, C. Singhal, S. Nagabooshanam, S. Nissar, T. Basu, S. C. Ray, S. Wadhwa, J. Narang, A. Mathur, *Biomed. Microdevices* **2019**, *22*, 6.
[68] J. C. K. Spiro, K. K. Mishra, V. N. Dhamu, A. Bhatia, S. Muthukumar, S. Prasad, *Sens. Diagn.* **2024**, DOI 10.1039/D4SD00234B.
[69] E. Fuhry, V. Guglielmotti, I. Wachta, D. Pallarola, K. Balasubramanian, *Anal. Sens.* **2024**, *4*, e202400037.
[70] D. C. Poudyal, M. Samson, V. N. Dhamu, S. Mohammed, C. N. Tanchez, A. Puri, D. Baby, S. Muthukumar, S. Prasad, *Electrochem* **2024**, *5*, 341.
[71] S. Madhurantakam, J. B. Karnam, V. N. Dhamu, S. Seetaraman, M. A. Gates-Hollingsworth, D. P. AuCoin, D. V. Clark, K. L. Schully, S. Muthukumar, S. Prasad, *ACS Infect. Dis.* **2024**, *10*, 2118.
[72] C. Esseghaier, Y. Bergaoui, H. ben Fredj, A. Tlili, S. Helali, S. Ameur, A. Abdelghani, *Sens. Actuators B Chem.* **2008**, *134*, 112.
[73] Y. Wei, X.-P. Liu, C. Mao, H.-L. Niu, J.-M. Song, B.-K. Jin, *Biosens. Bioelectron.* **2018**, *103*, 99.
[74] Z. V. Leonenko, E. Finot, H. Ma, T. E. S. Dahms, D. T. Cramb, *Biophys. J.* **2004**, *86*, 3783.
[75] S. J. Attwood, Y. Choi, Z. Leonenko, *Int. J. Mol. Sci.* **2013**, *14*, 3514.
[76] S. Lenhert, P. Sun, Y. Wang, H. Fuchs, C. A. Mirkin, *Small* **2007**, *3*, 71.
[77] S. Lenhert, F. Brinkmann, T. Laue, S. Walheim, C. Vannahme, S. Klinkhammer, M. Xu, S. Sekula, T. Mappes, T. Schimmel, H. Fuchs, *Nat. Nanotechnol.* **2010**, *5*, 275.

[78] S. Biswas, M. Hirtz, H. Fuchs, *Small* **2011**, *7*, 2081.
[79] I. Gustafson, *Colloids Surf. B Biointerfaces* **2003**, *30*, 13.
[80] E. J. Lafarge, P. Muller, A. P. Schroder, E. Zaitseva, J. C. Behrends, C. M. Marques, *Proc. Natl. Acad. Sci.* **2023**, *120*, e2213112120.
[81] G.-P. Nikoleli, D. P. Nikolelis, C. G. Siontorou, S. Karapetis, M.-T. Nikolelis, *Biosensors* **2018**, *8*, 61.
[82] Y. Wang, Y. Zhao, A. Bollas, Y. Wang, K. F. Au, *Nat. Biotechnol.* **2021**, *39*, 1348.
[83] T. Ensslen, K. Sarthak, A. Aksimentiev, J. C. Behrends, *J. Am. Chem. Soc.* **2022**, *144*, 16060.
[84] N. Michael Green, in *Methods Enzymol.* (Eds: M. Wilchek, E.A. Bayer), Academic Press, **1990**, pp. 51–67.
[85] Y.-P. Wu, C. Y. Chew, T.-N. Li, T.-H. Chung, E.-H. Chang, C. H. Lam, K.-T. Tan, *Chem. Sci.* **2018**, *9*, 770.
[86] A. Goujon, K. Straková, N. Sakai, S. Matile, *Chem. Sci.* **2018**, *10*, 310.
[87] C. M. Dundas, D. Demonte, S. Park, *Appl. Microbiol. Biotechnol.* **2013**, *97*, 9343.
[88] V. I. Lyamichev, L. E. Goodrich, E. H. Sullivan, R. M. Bannen, J. Benz, T. J. Albert, J. J. Patel, *Sci. Rep.* **2017**, *7*, 12116.
[89] R. E. Stenkamp, I. L. Trong, L. Klumb, P. S. Stayton, S. Freitag, *Protein Sci.* **1997**, *6*, 1157.
[90] "Streptavidin/biotin: Tethering geometry defines unbinding mechanics | Science Advances," can be found under https://www.science.org/doi/10.1126/sciadv.aay5999,
[91] P. Muret, *FUNDAMENTALS OF ELECTRONICS 2 : Continuous-Time Signals and Sy Stems*, ISTE/Wiley, London, **2018**.
[92] I. Şerban, A. Enesca, *Front. Chem.* **2020**, *8*, DOI 10.3389/fchem.2020.00354.
[93] P. W. Sayyad, S.-J. Park, T.-J. Ha, *Biosens. Bioelectron.* **2024**, *259*, 116407.
[94] O. V. Soldatkina, O. O. Soldatkin, T. P. Velychko, V. O. Prilipko, M. A. Kuibida, S. V. Dzyadevych, *Bioelectrochemistry* **2018**, *124*, 40.
[95] A. Charnas, Z. Zhang, Z. Lin, D. Zheng, J. Zhang, M. Si, P. D. Ye, *Adv. Mater.* **2024**, *36*, 2304044.
[96] Y. Sun, J. A. Rogers, *Adv. Mater.* **2007**, *19*, 1897.
[97] M. Marezio, *Acta Crystallogr.* **1966**, *20*, 723.
[98] F. Utsuno, H. Inoue, I. Yasui, Y. Shimane, S. Tomai, S. Matsuzaki, K. Inoue, I. Hirosawa, M. Sato, T. Honma, *Thin Solid Films* **2006**, *496*, 95.
[99] D. B. Buchholz, Q. Ma, D. Alducin, A. Ponce, M. Jose-Yacaman, R. Khanal, J. E. Medvedeva, R. P. H. Chang, *Chem. Mater.* **2014**, *26*, 5401.

[100] T. Kim, C. H. Choi, J. S. Hur, D. Ha, B. J. Kuh, Y. Kim, M. H. Cho, S. Kim, J. K. Jeong, *Adv. Mater.* **2023**, *35*, 2204663.
[101] R. D. Piner, J. Zhu, F. Xu, S. Hong, C. A. Mirkin, *Science* **1999**, *283*, 661.
[102] D. S. Ginger, H. Zhang, C. A. Mirkin, *Angew. Chem. Int. Ed.* **2004**, *43*, 30.
[103] P. E. Sheehan, L. J. Whitman, *Phys. Rev. Lett.* **2002**, *88*, 156104.
[104] P. V. Schwartz, *Langmuir* **2002**, *18*, 4041.
[105] S. Lenhert, C. A. Mirkin, H. Fuchs, *Scanning* **2010**, *32*, 15.
[106] B. L. Weeks, A. Noy, A. E. Miller, J. J. De Yoreo, *Phys. Rev. Lett.* **2002**, *88*, 255505.
[107] M. Su, V. P. Dravid, *Appl. Phys. Lett.* **2002**, *80*, 4434.
[108] K. Salaita, Y. Wang, J. Fragala, R. A. Vega, C. Liu, C. A. Mirkin, *Angew. Chem. Int. Ed.* **2006**, *45*, 7220.
[109] J. Haaheim, R. Eby, M. Nelson, J. Fragala, B. Rosner, H. Zhang, G. Athas, *Ultramicroscopy* **2005**, *103*, 117.
[110] K. A. Brown, D. J. Eichelsdoerfer, X. Liao, S. He, C. A. Mirkin, *Front. Phys.* **2014**, *9*, 385.
[111] E. Berganza, M. P. Ebrahimkutty, S. K. Vasantham, C. Zhong, A. Wunsch, A. Navarrete, M. Galic, M. Hirtz, *Nanoscale* **2021**, *13*, 12642.
[112] S. K. Vasantham, E. Boltynjuk, S. H. Nandam, E. Berganza Eguiarte, H. Fuchs, H. Hahn, M. Hirtz, *Adv. Mater. Interfaces* **2024**, *11*, 2300721.
[113] M. Hirtz, R. Corso, S. Sekula-Neuner, H. Fuchs, *Langmuir* **2011**, *27*, 11605.
[114] F. Brinkmann, M. Hirtz, A. M. Greiner, M. Weschenfelder, B. Waterkotte, M. Bastmeyer, H. Fuchs, *Small* **2013**, *9*, 3266.
[115] G. Liu, S. H. Petrosko, Z. Zheng, C. A. Mirkin, *Chem. Rev.* **2020**, *120*, 6009.
[116] A. Urtizberea, M. Hirtz, *Nanoscale* **2015**, *7*, 15618.
[117] P. L. Ritger, N. A. Peppas, *J. Controlled Release* **1987**, *5*, 23.
[118] A. Urtizberea, M. Hirtz, *Nanoscale* **2015**, *7*, 15618.
[119] S. H. White, W. C. Wimley, A. S. Ladokhin, K. Hristova, in *Methods Enzymol.*, Academic Press, **1998**, pp. 62–87.
[120] R. Kaçar, R. B. Serin, E. Uçar, A. Ülkü, *Mater. Today Commun.* **2023**, *35*, 105534.
[121] W. Wu, *Nanoscale* **2017**, *9*, 7342.
[122] E. Sowade, K. Y. Mitra, E. Ramon, C. Martinez-Domingo, F. Villani, F. Loffredo, H. L. Gomes, R. R. Baumann, *Org. Electron.* **2016**, *30*, 237.
[123] H. Minemawari, T. Yamada, H. Matsui, J. Tsutsumi, S. Haas, R. Chiba, R. Kumai, T. Hasegawa, *Nature* **2011**, *475*, 364.

[124] A. Bogner, P.-H. Jouneau, G. Thollet, D. Basset, C. Gauthier, *Micron* **2007**, *38*, 390.

[125] K. D. Vernon-Parry, *III-Vs Rev.* **2000**, *13*, 40.

[126] W. Zhou, R. Apkarian, Z. L. Wang, D. Joy, in *Scanning Microsc. Nanotechnol. Tech. Appl.* (Eds: W. Zhou, Z.L. Wang), Springer, New York, NY, **2007**, pp. 1–40.

[127] I. Horcas, R. Fernández, J. M. Gómez-Rodríguez, J. Colchero, J. Gómez-Herrero, A. M. Baro, *Rev. Sci. Instrum.* **2007**, *78*, 013705.

[128] "Atomic Force Microscopy: Understanding Basic Modes and Advanced Applications - Haugstad, Greg: 9780470638828 - AbeBooks," can be found under https://www.abebooks.de/9780470638828/Atomic-Force-Microscopy-Understanding-Basic-0470638826/plp,

[129] G. Haugstad, Wiley, **2012**.

[130] "CO2 Laser Fabrication of a Passive continuous-flow T-shaped Polymethyl Methacrylate (PMMA) Micromixer | springerprofessional.de," can be found under https://link.springer.com/article/10.1007/s40516-023-00212-x,

[131] A. K. Dubey, V. Yadava, *Int. J. Mach. Tools Manuf.* **2008**, *48*, 609.

[132] H. Gleiter, *Beilstein J. Nanotechnol.* **2013**, *4*, 517.

[133] S. H. Nandam, Y. Ivanisenko, R. Schwaiger, Z. Śniadecki, X. Mu, D. Wang, R. Chellali, T. Boll, A. Kilmametov, T. Bergfeldt, H. Gleiter, H. Hahn, *Acta Mater.* **2017**, *136*, 181.

[134] S. H. Nandam, O. Adjaoud, R. Schwaiger, Y. Ivanisenko, M. R. Chellali, D. Wang, K. Albe, H. Hahn, *Acta Mater.* **2020**, *193*, 252.

[135] N. Chen, R. Frank, N. Asao, D. V. Louzguine-Luzgin, P. Sharma, J. Q. Wang, G. Q. Xie, Y. Ishikawa, N. Hatakeyama, Y. C. Lin, M. Esashi, Y. Yamamoto, A. Inoue, *Acta Mater.* **2011**, *59*, 6433.

[136] H. Voigt, A. Rigoni, E. Boltynjuk, M. R. Chellali, B. Tyler, H. Rösner, S. Divinski, H. Hahn, G. Wilde, *Adv. Funct. Mater.*., *n/a*, 2302386.

[137] Y. Ivanisenko, C. Kübel, S. H. Nandam, C. Wang, X. Mu, O. Adjaoud, K. Albe, H. Hahn, *Adv. Eng. Mater.* **2018**, *20*, 1800404.

[138] R. S. Averback, H. Hahn, H. J. Höfler, J. C. Logas, *Appl. Phys. Lett.* **1990**, *57*, 1745.

[139] P. Gong, X. Wang, Y. Shao, N. Chen, X. Liu, K. F. Yao, *Intermetallics* **2013**, *43*, 177.

[140] S. V. Ketov, X. Shi, G. Xie, R. Kumashiro, A. Y. Churyumov, A. I. Bazlov, N. Chen, Y. Ishikawa, N. Asao, H. Wu, D. V. Louzguine-Luzgin, *Sci. Rep.* **2015**, *5*, 7799.

[141] N. Chen, X. Shi, R. Witte, K. S. Nakayama, K. Ohmura, H. Wu, A. Takeuchi, H. Hahn, M. Esashi, H. Gleiter, A. Inoue, D. V. Louzguine, *J. Mater. Chem. B* **2013**, *1*, 2568.

[142] I. Casanellas, J. Samitier, A. Lagunas, *Front. Bioeng. Biotechnol.* **2022**, *10*, DOI 10.3389/fbioe.2022.1002967.

[143] K. Modaresifar, S. Azizian, M. Ganjian, L. E. Fratila-Apachitei, A. A. Zadpoor, *Acta Biomater.* **2019**, *83*, 29.

[144] S. Namgung, T. Kim, K. Y. Baik, M. Lee, J.-M. Nam, S. Hong, *Small* **2011**, *7*, 56.

[145] L. Richert, F. Vetrone, J.-H. Yi, S. F. Zalzal, J. D. Wuest, F. Rosei, A. Nanci, *Adv. Mater.* **2008**, *20*, 1488.

[146] X. Shi, S. Chen, J. Zhou, H. Yu, L. Li, H. Wu, *Adv. Funct. Mater.* **2012**, *22*, 3799.

[147] D. Marsh, *Biochim. Biophys. Acta BBA - Biomembr.* **2008**, *1778*, 1545.

[148] L. Xiao, Y. Sun, L. Liao, X. Su, *J. Mater. Chem. B* **2023**, *11*, 2550.

[149] T. W. Lowry, A. E. Kusi-Appiah, D. A. Fadool, S. Lenhert, *Membranes* **2023**, *13*, 151.

[150] G. Liu, M. Hirtz, H. Fuchs, Z. Zheng, *Small* **2019**, *15*, 1900564.

[151] S. Lenhert, P. Sun, Y. Wang, H. Fuchs, C. A. Mirkin, *Small* **2007**, *3*, 71.

[152] "3D Nanolithography by Means of Lipid Ink Spreading Inhibition - Berganza - 2023 - Small - Wiley Online Library," can be found under https://onlinelibrary.wiley.com/doi/full/10.1002/smll.202205590, **n.d.**

[153] A. E. Kusi-Appiah, N. Vafai, P. J. Cranfill, M. W. Davidson, S. Lenhert, *Biomaterials* **2012**, *33*, 4187.

[154] S. Sekula, J. Fuchs, S. Weg-Remers, P. Nagel, S. Schuppler, J. Fragala, N. Theilacker, M. Franzreb, C. Wingren, P. Ellmark, C. A. K. Borrebaeck, C. A. Mirkin, H. Fuchs, S. Lenhert, *Small* **2008**, *4*, 1785.

[155] H.-Y. Liu, R. Kumar, C. Zhong, S. Gorji, L. Paniushkina, R. Masood, U. A. Wittel, H. Fuchs, I. Nazarenko, M. Hirtz, *Adv. Mater.* **2021**, *33*, 2008493.

[156] A. Luchini, G. Vitiello, *Biomimetics* **2021**, *6*, 3.

[157] N. Willems, A. Urtizberea, A. F. Verre, M. Iliut, M. Lelimousin, M. Hirtz, A. Vijayaraghavan, M. S. P. Sansom, *ACS Nano* **2017**, *11*, 1613.

[158] B. Sanii, A. N. Parikh, *Soft Matter* **2007**, *3*, 974.

[159] M. Gavutis, V. Navikas, T. Rakickas, Š. Vaitekonis, R. Valiokas, *J. Micromechanics Microengineering* **2016**, *26*, 025016.

[160] I. Gözen, P. Dommersnes, A. Jesorka, I. Gözen, P. Dommersnes, A. Jesorka, in *Surf. Energy*, IntechOpen, **2015**.

[161] F. Blachon, F. Harb, B. Munteanu, A. Piednoir, R. Fulcrand, T. Charitat, G. Fragneto, O. Pierre-Louis, B. Tinland, J.-P. Rieu, *Langmuir* **2017**, *33*, 2444.

[162] K. Mori, S. Samata, N. Mitsugi, A. Teramoto, R. Kuroda, T. Suwa, K. Hashimoto, S. Sugawa, *Jpn. J. Appl. Phys.* **2020**, *59*, SMMB06.

[163] S. M. M. Dadfar, S. Sekula-Neuner, V. Trouillet, M. Hirtz, *Adv. Mater. Interfaces* **2021**, *8*, 2002117.

[164] N. Chada, K. P. Sigdel, R. R. S. Gari, T. R. Matin, L. L. Randall, G. M. King, *Sci. Rep.* **2015**, *5*, 12550.

[165] X. Chen, S. Lenhert, M. Hirtz, N. Lu, H. Fuchs, L. Chi, *Acc. Chem. Res.* **2007**, *40*, 393.

[166] M. Majewska, D. Mrdenovic, I. S. Pieta, R. Nowakowski, P. Pieta, *Biochim. Biophys. Acta BBA - Biomembr.* **2020**, *1862*, 183347.

[167] C. Leidy, T. Kaasgaard, J. H. Crowe, O. G. Mouritsen, K. Jørgensen, *Biophys. J.* **2002**, *83*, 2625.

[168] H. Takahashi, A. Miyagi, L. Redondo-Morata, S. Scheuring, *Small* **2016**, *12*, 6106.

[169] S. K. Arya, S. Bhansali, *Chem. Rev.* **2011**, *111*, 6783.

[170] M. Wang, Y. Yang, J. Min, Y. Song, J. Tu, D. Mukasa, C. Ye, C. Xu, N. Heflin, J. S. McCune, T. K. Hsiai, Z. Li, W. Gao, *Nat. Biomed. Eng.* **2022**, *6*, 1225.

[171] A. K. P, D. Sekar, *Hypertens. Res.* **2024**, *47*, 1752.

[172] J. Wu, H. Liu, W. Chen, B. Ma, H. Ju, *Nat. Rev. Bioeng.* **2023**, *1*, 346.

[173] C. Dincer, R. Bruch, E. Costa-Rama, M. T. Fernández-Abedul, A. Merkoçi, A. Manz, G. A. Urban, F. Güder, *Adv. Mater.* **2019**, *31*, 1806739.

[174] N. S. Oliver, C. Toumazou, A. E. G. Cass, D. G. Johnston, *Diabet. Med.* **2009**, *26*, 197.

[175] J. Leva-Bueno, S. A. Peyman, P. A. Millner, *Med. Microbiol. Immunol. (Berl.)* **2020**, *209*, 343.

[176] M. M. Khoo, K. L. Ng, Y. Alias, S. M. Khor, *J. Electroanal. Chem.* **2017**, *799*, 111.

[177] J. S. Cisneros, C. Y. Chain, M. A. Daza Millone, C. A. Labriola, K. Scollo, A. M. Ruiz, P. Estrela, M. E. Vela, *Biosens. Bioelectron. X* **2022**, *12*, 100261.

[178] H. Cho, S. Shim, W. W. Cho, S. Cho, H. Baek, S.-M. Lee, D.-S. Shin, *ACS Sens.* **2022**, *7*, 1676.

[179] S. Afsahi, M. B. Lerner, J. M. Goldstein, J. Lee, X. Tang, D. A. Bagarozzi, D. Pan, L. Locascio, A. Walker, F. Barron, B. R. Goldsmith, *Biosens. Bioelectron.* **2018**, *100*, 85.

[180] Y. Chen, R. Ren, H. Pu, X. Guo, J. Chang, G. Zhou, S. Mao, M. Kron, J. Chen, *Sci. Rep.* **2017**, *7*, 10974.

[181] J. Wang, T. Lu, M. Yang, D. Sun, Y. Xia, T. Wang, *Sci. Adv.* **2019**, *5*, eaau8769.

[182] F. N. Ishikawa, H.-K. Chang, M. Curreli, H.-I. Liao, C. A. Olson, P.-C. Chen, R. Zhang, R. W. Roberts, R. Sun, R. J. Cote, M. E. Thompson, C. Zhou, *ACS Nano* **2009**, *3*, 1219.

[183] P. Fathi-Hafshejani, N. Azam, L. Wang, M. A. Kuroda, M. C. Hamilton, S. Hasim, M. Mahjouri-Samani, *ACS Nano* **2021**, *15*, 11461.

[184] E. Bihar, S. Wustoni, A. M. Pappa, K. N. Salama, D. Baran, S. Inal, *Npj Flex. Electron.* **2018**, *2*, 1.

[185] R. Domingo-Roca, P. Lasserre, L. Riordan, A. R. Macdonald, A. Dobrea, K. R. Duncan, S. Hannah, M. Murphy, P. A. Hoskisson, D. K. Corrigan, *Biosens. Bioelectron. X* **2023**, *13*, 100308.

[186] G. Rosati, M. Urban, L. Zhao, Q. Yang, C. de Carvalho Castro e Silva, S. Bonaldo, C. Parolo, E. P. Nguyen, G. Ortega, P. Fornasiero, A. Paccagnella, A. Merkoçi, *Biosens. Bioelectron.* **2022**, *196*, 113737.

[187] B. Nagar, M. Balsells, A. de la Escosura-Muñiz, P. Gomez-Romero, A. Merkoçi, *Biosens. Bioelectron.* **2019**, *129*, 238.

[188] V. Druet, D. Ohayon, C. E. Petoukhoff, Y. Zhong, N. Alshehri, A. Koklu, P. D. Nayak, L. Salvigni, L. Almulla, J. Surgailis, S. Griggs, I. McCulloch, F. Laquai, S. Inal, *Nat. Commun.* **2023**, *14*, 5481.

[189] J. Rivnay, M. Ramuz, P. Leleux, A. Hama, M. Huerta, R. M. Owens, *Appl. Phys. Lett.* **2015**, *106*, 043301.

[190] H. Song, J. Spencer, A. Jander, J. Nielsen, J. Stasiak, V. Kasperchik, P. Dhagat, *J. Appl. Phys.* **2014**, *115*, 17E308.

[191] D. Dong, D. Zheng, F.-Q. Wang, X.-Q. Yang, N. Wang, Y.-G. Li, L.-H. Guo, J. Cheng, *Anal. Chem.* **2004**, *76*, 499.

[192] G. Cadilha Marques, L. Yang, Y. Liu, V. Wollersen, T. Scherer, B. Breitung, M. Wegener, J. Aghassi-Hagmann, *Adv. Mater. Technol.* **2023**, *8*, 2370121.

[193] B. Kim, *Adv. Electron. Mater.* **2020**, *6*, 1901068.

[194] U. Bog, F. Brinkmann, H. Kalt, C. Koos, T. Mappes, M. Hirtz, H. Fuchs, S. Köber, *Small* **2014**, *10*, 3863.

[195] A. Määttänen, U. Vanamo, P. Ihalainen, P. Pulkkinen, H. Tenhu, J. Bobacka, J. Peltonen, *Sens. Actuators B Chem.* **2013**, *177*, 153.

[196] E. B. Bahadır, M. K. Sezgintürk, *Artif. Cells Nanomedicine Biotechnol.* **2016**, *44*, 248.

[197] E. B. Aydın, M. K. Sezgintürk, *TrAC Trends Anal. Chem.* **2017**, *97*, 309.

[198] Yvonne Y. Duan, Graeme M. Clark, Robert S. C. Cowan, **2001**, pp. 498–508.

[199] A. K. Bavil, D. Sticker, M. Rothbauer, P. Ertl, J. Kim, *Analyst* **2021**, *146*, 3289.

[200] S. Abasi, J. R. Aggas, G. G. Garayar-Leyva, B. K. Walther, A. Guiseppi-Elie, *ACS Meas. Sci. Au* **2022**, *2*, 495.

[201] A. Santos, J. J. Davis, P. R. Bueno, *J. Anal. Bioanal. Tech.* **2014**, *0*, DOI 10.4172/2155-9872.S7-016.

[202] C.-H. Chuang, Y.-C. Du, T.-F. Wu, C.-H. Chen, D.-H. Lee, S.-M. Chen, T.-C. Huang, H.-P. Wu, M. Shaikh, *Biosens. Bioelectron.* **2015**, *84*, DOI 10.1016/j.bios.2015.12.103.

[203] M. Brodowski, M. Pierpaoli, M. Janik, M. Kowalski, M. Ficek, P. Slepski, B. Trzaskowski, G. Swain, J. Ryl, R. Bogdanowicz, *Sens. Actuators B Chem.* **2022**, *370*, 132427.

[204] M. Tanaka, E. Sackmann, *Phys. Status Solidi A* **2006**, *203*, 3452.

[205] K. Baler, O. A. Martin, M. A. Carignano, G. A. Ameer, J. A. Vila, I. Szleifer, *J. Phys. Chem. B* **2014**, *118*, 921.

[206] S. Popescu, C. Dale, N. Keegan, B. Ghosh, R. Kaner, J. Hedley, *Procedia Technol.* **2017**, *27*, 274.

[207] A. Schmidt, J. Spinke, T. Bayerl, E. Sackmann, W. Knoll, *Biophys. J.* **1992**, *63*, 1385.

[208] D. Dziubak, K. Pułka-Ziach, S. Sęk, *J. Phys. Chem. C* **2020**, *124*, 17916.

[209] J. H. T. Luong, S. K. Vashist, *ACS Omega* **2020**, *5*, 10.